Retinal Neurons: Establishing order through avoidance

A Dissertation
Presented in Partial Fulfillment of the Requirements for the
Degree of Doctorate of Philosophy
with a
Major in Microbiology, Molecular Biology and Biochemistry
in the
College of Graduate Studies
University of Idaho
by

Aaron B. Simmons

Major Professor: Peter Fuerst, Ph.D.
Committee Members: Deborah Stenkamp, Ph.D.; Elizabeth Fortunato, Ph.D.;
James Pru, Ph.D.
Department Administrator: James Nagler, Ph.D.

May 2017

Authorization to Submit Dissertation

This dissertation of Aaron Simmons, submitted for the degree of Doctorate of Philosophy with a Major in Microbiology, Molecular Biology and Biochemistry and titled “Retinal Neurons: Establishing order through avoidance,” has been reviewed in final form. Permission, as indicated by the signatures and dates below, is now granted to submit final copies to the College of Graduate Studies for approval.

Major Professor: _____ Date: _____

Peter Fuerst, Ph.D.

Committee Members: _____ Date: _____

Deborah Stenkamp, Ph.D.

_____ Date: _____

Elizabeth Fortunato, Ph.D.

_____ Date: _____

James Pru, Ph.D.

Department Administrator: _____ Date: _____

James Nagler, Ph.D.

Abstract

Vision is the primary sense used by humans to interact with their surrounding world. Our sense of vision originates within the retina, a highly specialized projection of the central nervous system, which gathers sensory information in the form of light and then converts it into useful visual information before conveying it to the brain. The retina is composed of neurons, glia, and cells of the vasculature, all of which are highly organized within the retina. The work in this dissertation explores cellular interactions that are responsible for directing formation of this highly organized tissue and identifies novel neuron-vessel and neuron-neuron interactions that pertain to developmental and disease processes.

The second chapter explores how the neurons of the retina drive organization of the retinal vasculature. We find that the placement of neurons is important for the distribution of neural derived factors mediating vessel patterning. Disruptions in neural patterning lead to the misrepresentation of neural-derived factors resulting in fragile vessels that leak blood. The third chapter is a technical book chapter that outlines methodology used to measure retinal vessels in mouse models, providing a useful tool for researchers studying retinal vessel patterning.

The fourth chapter explores regulatory mechanisms that inhibit plasticity in mature neurons, an important factor limiting cell replacement therapies for retinal degenerative blinding disorders. We identify an important negative regulator of neuron plasticity, Down syndrome cell adhesion molecule (Dscam), and find it necessary for cellular interactions between neurons, resulting in inhibition of dendrite and axon outgrow. Elimination of Dscam in mature neurons stimulates dendrite and axon outgrowth and the formation of novel connections. The fifth chapter characterizes a transgenic mouse that was used to manipulate Dscam in mature neurons.

The work in this dissertation identifies important factors that drive vascular pathology that can result in retinal degenerative blinding disorders. Furthermore, this work identifies a potential therapeutic target that can be targeted to stimulate synaptogenesis allowing newly implanted cell populations to wire into existing circuits to restore vision.

Acknowledgements

First and foremost, I want to acknowledge my major professor, Dr. Peter Fuerst, who has been instrumental to my success as a graduate student and researcher. Through your dedication and enthusiasm, you have taught me how to formulate ideas, design and execute thoughtful experiments, and critically think about experimental outcomes, all the while having fun doing it. Your understanding during times of hardship, both professionally and personally, has allowed me to balance the challenges of being a scientist and a father. I am forever grateful that you provided me with the opportunity and freedom to pursue my own interests. Thank you for everything.

I also want to acknowledge my Ph.D. committee members: Dr. Deborah Stenkamp, Dr. Elizabeth Fortunato, and Dr. James Pru. Your critical evaluations of my progress, along with your insightful suggestions, helped steer the focus and impact of my research. I appreciate all of you for the time you have taken to support me in my efforts and your willingness to provide guidance when needed. I am honored to have you as my mentors.

I also want to acknowledge all of the Fuerst Lab members that aided with the work presented in this dissertation, particularly: Shuai Li, Josh Sukeena, Sam Bloomsburg, Morgan Merrill, CJ Miller, Carlos Galicia and Justin Reed. Your contributions through intellectual discussions and the collection of data have helped tremendously with my research.

Last but not least, I want to acknowledge my parents, Jennifer and Patrick. Through experiences and by example, you have provided me with a foundation of morals and work ethic that have shaped who I am today. Thank you for all of the sacrifices you have made to help me achieve this goal.

Dedication

I dedicate this dissertation to my wife and best friend, Courtney, my most important source of strength. Thank you for believing in me, even when I did not believe in myself. Without your love and support, none of this is possible.

I also want to dedicate this dissertation to my children: Blaire, Nolan, Joel, and Mark, who add so much joy and purpose to my life. May you all realize your talents and relentlessly pursue them, even in the face of adversity.

Table of Contents

List of Figures

List of Tables

Author Contributions for Multiple-Authored Work

The work in the following document contains multiple-authored work that is shared by Aaron Simmons and Samuel Bloomsburg and is presented in chapters within Simmons' dissertation and Bloomsburg's thesis.

In the chapter "Non-selective OFF bipolar cell plasticity is inhibited by DSCAM mediated enforcement of dendritic and axonal outgrowth in the adult mouse retina," Simmons is the primary author and took lead on conceptualization of the project and oversight of all conducted experiments. Simmons developed the methodologies to visualize and measure bipolar cell morphometrics and discovered DSCAM as a negative regulator of plasticity in non-selective OFF bipolar cells during development through the enforcement of neuron tiling. Bloomsburg assisted with all of the experiments for the project and took lead on experiments associated with bipolar cell axons. Bloomsburg discovered that DSCAM is localized to bipolar cell axons and is required to organize their axon morphologies. Bloomsburg developed methodologies to measure population dynamics of bipolar cell innervation of cones. Together Simmons and Bloomsburg discovered the role of DSCAM in mature neurons is to continually inhibition dendrite and axon outgrowth and removing DSCAM inhibition is sufficient to stimulate synaptogenesis.

In the chapter "Pou4f2 knock-in Cre mouse: A multifaceted genetic tool for vision researchers," Simmons is the primary author and took lead on conceptualization of the project and oversight of all conducted experiments. Simmons mapped out the insertion point of *Pou4f2:Cre* and explored its mode of action, which depends upon the mouse breeding scheme. Bloomsburg assisted with all of the experiments for the project and took lead on experiments elucidating the developmental expression patterns of *Pou4f2:Cre* expression pattern within the retina and the brain.

Chapter 1: Introduction to retina structure, function, and disease

Vision is the dominant sense used by humans that allows us to interact and experience our surrounding world. Our sense of vision originates within the retina, the light-sensitive tissue of the central nervous system, which resides at the back of the eye. Neurons within the retina are organized into alternating cellular and synaptic layers consisting of three cellular layers: the outer nuclear layer (ONL), the inner nuclear layer (INL), and the retinal ganglion cell layer (RGL); and two synaptic layers: the outer and inner plexiform layers (OPL and IPL, respectively)[1]. Retinal neurons rely upon this organization to create neural circuits that encode basic sensory information, light, into fundamental aspects of vision that the brain integrates to form an image.

The visual encoding process begins at the very first synapse within the retina where photoreceptors, the light sensitive neurons of the visual system, connect to more than a dozen types of interneurons called bipolar cells[2]. Each type of bipolar cell differentially responds to photoreceptor input, based upon their biochemical makeup, generating a series of parallel mini-circuits that encode for specific types of visual stimuli, e.g. polarity, contrast, temporal profile and chromatic composition[2]. Bipolar cells then relay this information onto retinal ganglion cells, which relay this information off to the visual centers of the brain for further processing[1]. Superimposed upon this, the transmission of signal between photoreceptors, bipolar cells, and ganglion cells is laterally modulated by other types of interneurons, horizontal and amacrine cells, thereby further encoding visual information[1].

The neural retina requires the support of retinal vessels and glia in order to continue to carry out its function of encoding and transmission of visual information. Retinal neurons are nourished by two vascular systems: the retinal vessels, found within the retinal tissue, and the choroidal vessels, found above the photoreceptors[3]. There are three types of glial cells found within the retina: Müller cells, astrocytes, and microglia, which carry out homeostatic and protective roles to maintain retina physiology. Müller cells reside within the INL where they project out large radial processes spanning the thickness of the retina, providing structural support for the entire tissue[4]. Müller cells also send out smaller tangential processes into the retinal layers that interact with neurons to remove cellular waste and recycle neurotransmitters[4]. Tangential processes also wrap blood vessels to help form the blood-retina-barrier[4]. Astrocytes are found along the surface of the retina, where they wrap retinal blood vessels, to aid with formation of the blood-retina-barrier[5], and

neurons, to aid with synaptic maintenance[5] and also modulate neurotransmission[6]. Microglia are the macrophages of the retina and are found within the synaptic layers of the retina where they function in removal of cellular waste and debris and have also been shown to be important for maintaining synaptic structure[7]. During development and throughout adulthood there is a tremendous amount of crosstalk between retinal neurons, glia, and cells of the vasculature. This communication is essential for the retina development, and also to maintain the integrity of the mature retina.

Vascular retinopathies encompass a large group of retinal degenerative diseases where the disregulation of the vascular networks result in the pathological proliferation of new blood vessels, the over-activation of glia, and the degeneration of neurons. These diseases processes can be inherited like in retinitis pigmentosa[8, 9], initiated by other diseases like in diabetic retinopathy[10], caused by extremely premature birth like in retinopathy of prematurity[11], or simply be part of the natural aging process like in age-related macular degeneration[12]. As these diseases progress, their pathophysiologies become increasing more difficult to interpret as the retina attempts to respond to these insults through remodeling processes. A greater understanding of normal cellular interactions between the retina's neurons, glia, and cells of the vascular will shed light on how these interactions go awry during disease and potentially uncover interactions we can exploit to cure, or at least effectively manage, retinopathies causing blindness.

A major finding in this dissertation is the requirement of neuron placement on retinal vessel patterning (Chapter 2)[13]. This work uses a series of genetic mouse models with disrupted neuron organization of the retinal layers to study how neuron placement changes the dynamics of cellular interactions between neurons and blood vessels. We find that disorganization of the neural retina is reflected by the retina's glia and blood vessels. Furthermore, we find that the displacement of neurons is sufficient to mislocalize known angiogenic factors that mediate vessel patterning and that the mispatterned vessels are fragile and leak blood. This work also includes novel methodologies (Chapter 3) used to measure morphological characteristics of the retinal vasculature, providing a useful tool that can be used by those interested in studying factors influencing retinal vessel patterning.

One of the most attractive approaches to cure retinal degenerative diseases are cell replacement therapies, especially in diseases like age-related macular degeneration or retinitis pigmentosa, where photoreceptors degenerate but the down-stream retinal circuitry remains intact. Unfortunately, current attempts to achieve successful transplantation that restores retinal function fall short due to the inability of transplanted cells to integrate into

mature existing circuits. Developing neurons retain the ability to extend dendrites and axons to make new connections, but as neurons mature, their ability to continue to make new connections is diminished[14-16]. This inability of mature neurons to make new connections likely explain the shortcomings of current cell replacement approaches, as neurons within the existing circuitry are unable to make new connections with transplanted cells. Identification of the factors and mechanisms that inhibit a neuron's ability to make new connections will provide potential signaling pathways and molecules that can be targeted to stimulate synaptogenesis and enhance cell replacement therapies.

Another major finding in this dissertation identifies Down syndrome cell adhesion molecule (Dscam) as an intrinsic negative regulator of neural plasticity (Chapter 4). By studying a population of bipolar cells expressing Dscam, we find that Dscam mediates cellular interactions between neighboring bipolar cells of the same subtype and that these interactions prevent the growth of dendritic and axonal arbors from invading each other's territories. We find that elimination of Dscam in mature neurons is sufficient to stimulate axon and dendrite outgrowth and the formation of new connections. This work also includes the characterization of a multifaceted cre-expressing transgenic mouse line that will be a useful tool for vision researchers (Chapter 5)[17].

The research within this dissertation is relevant towards human health. This work identifies neural placement as an important factor, that when disrupted, can drive vascular pathology – the underlying cause of many retinal degenerative blinding disorders. This work goes on to identify a potential therapeutic target that can be targeted to stimulate synaptogenesis allowing newly implanted cell populations to wire into existing circuits to restore vision for patients that have lost their vision due to retinal disease processes.

REFERENCES

1. Masland RH. The neuronal organization of the retina. *Neuron* 2012;76:266-280.
2. Euler T, Haverkamp S, Schubert T, Baden T. Retinal bipolar cells: elementary building blocks of vision. *Nature reviews Neuroscience* 2014;15:507-519.
3. Kolb H. Simple Anatomy of the Retina. In: Kolb H, Fernandez E, Nelson R (eds), *Webvision: The Organization of the Retina and Visual System.* Salt Lake City (UT); 1995.
4. Kolb H. Glial Cells of the Retina. In: Kolb H, Fernandez E, Nelson R (eds), *Webvision: The Organization of the Retina and Visual System.* Salt Lake City (UT); 1995.

5. Vecino E, Rodriguez FD, Ruzafa N, Pereiro X, Sharma SC. Glia-neuron interactions in the mammalian retina. *Progress in retinal and eye research* 2015.
6. Allen NJ, Barres BA. Signaling between glia and neurons: focus on synaptic plasticity. *Current opinion in neurobiology* 2005;15:542-548.
7. Stephan AH, Barres BA, Stevens B. The complement system: an unexpected role in synaptic pruning during development and disease. *Annual review of neuroscience* 2012;35:369-389.
8. Jones BW, Kondo M, Terasaki H, Lin Y, McCall M, Marc RE. Retinal remodeling. *Japanese journal of ophthalmology* 2012;56:289-306.
9. Jones BW, Pfeiffer RL, Ferrell WD, Watt CB, Marmor M, Marc RE. Retinal remodeling in human retinitis pigmentosa. *Experimental eye research* 2016;150:149-165.
10. Lutty GA. Effects of diabetes on the eye. *Investigative ophthalmology & visual science* 2013;54:ORSF81-87.
11. Hartnett ME. Advances in understanding and management of retinopathy of prematurity. *Survey of ophthalmology* 2016.
12. Hageman GS, Gehrs K, Johnson LV, Anderson D. Age-Related Macular Degeneration (AMD). In: Kolb H, Fernandez E, Nelson R (eds), *Webvision: The Organization of the Retina and Visual System.* Salt Lake City (UT); 1995.
13. Simmons AB, Merrill MM, Reed JC, Deans MR, Edwards MM, Fuerst PG. Defective Angiogenesis and Intraretinal Bleeding in Mouse Models With Disrupted Inner Retinal Lamination. *Investigative ophthalmology & visual science* 2016;57:1563-1577.
14. Bavelier D, Levi DM, Li RW, Dan Y, Hensch TK. Removing brakes on adult brain plasticity: from molecular to behavioral interventions. *The Journal of neuroscience : the official journal of the Society for Neuroscience* 2010;30:14964-14971.
15. Hubel DH, Wiesel TN. The period of susceptibility to the physiological effects of unilateral eye closure in kittens. *The Journal of physiology* 1970;206:419-436.
16. Ramoa AS, Campbell G, Shatz CJ. Dendritic growth and remodeling of cat retinal ganglion cells during fetal and postnatal development. *The Journal of neuroscience : the official journal of the Society for Neuroscience* 1988;8:4239-4261.
17. Simmons AB, Bloomsburg SJ, Billingslea SA, et al. Pou4f2 knock-in Cre mouse: A multifaceted genetic tool for vision researchers. *Molecular vision* 2016;22:705-717.

Chapter 2: Defective angiogenesis and intraretinal bleeding in mouse models with disrupted inner retinal lamination

Aaron B. Simmons, Morgan M. Merrill, Justin C. Reed, Michael R. Deans, Malia M. Edwards, and Peter G. Fuerst

Current Status: Published in *Investigative Ophthalmology & Visual Science*
Citation: Simmons, A.B., Merrill, M.M., Reed J.C., Deans M.R., Edwards M.M., and Fuerst, P.G. Defective angiogenesis and intraretinal bleeding in mouse models with disrupted inner retinal lamination. Investigative Ophthalmology & Visual Science. 2016 Apr 1;57(4):1563-77. PMID: 27046121

ABSTRACT

Purpose: Abnormal retinal angiogenesis leads to visual impairment and blindness. Understanding how retinal vessels develop normally has dramatically improved treatments for people with retinal vasculopathies, but additional information about development is required. Abnormal neuron patterning in the outer retina has been shown to result in abnormal vessel development and blindness, for example, in people and mouse models with *Crumbs homologue 1* (*CRB1*) mutations. In this study, we report and characterize a mouse model of inner retinal lamination disruption and bleeding, the Down syndrome cell adhesion molecule (*Dscam*) mutant, and test how neuron-neurite placement within the inner retina guides development of intraretinal vessels.

Methods: *Bax* mutant mice (increased neuron cell number), *Dscam* mutant mice (increased neuron cell number, disorganized lamination), *Fat3* mutant mice (disorganized neuron lamination) and *Dscam* gain-of-function mice ($Dscam^{GOF}$) (decreased neuron cell number) were used to manipulate neuron placement and number. Immunohistochemistry was used to assay organization of blood vessels, glia, and neurons. *In-situ* hybridization was used map the expression of angiogenic factors.

Results: Significant changes in the organization of vessels within mutant retinas were found. Displaced neurons and microglia were associated with the attraction of vessels. Using *Fat3* mutants and $Dscam^{GOF}$ retinas, we provide experimental evidence that vessel branching is induced at the neuron-neurite interface, but that other factors are required for

full plexus layer formation. We further demonstrate that the displacement of neurons results in the mislocalization of angiogenic factors.

Conclusion: Inner retina neuron lamination is required for development of intraretinal vessels.

INTRODUCTION

Retinal neurons in humans are nourished by three vasculature networks, or plexi, and the choroidal vessels, an organization that is shared between human and mouse[1]. Many blinding diseases including macular degeneration, vasculopathy of prematurity and diabetic retinopathy are caused by aberrant growth and maintenance of these vessels, resulting in retinal neuron death and subsequent vision loss[2-4]. Understanding the normal development of these vessels will help us better understand what happens to them during these disease processes.

The mouse retina serves as an excellent model for understanding basic principles guiding vessel development because its development and structure is similar to the human retina[1]. The immature retina is nourished by a fetal or hyaloid vascular system, which resides within the vitreous and is eventually replaced by retinal vessels during development[1]. Hyaloid vessels begin to regress at birth in the mouse, as the retinal vessels enter the retina through the optic nerve head (ONH). Retinal vessels proliferate out radially across the surface of the retina to form the superficial plexus (SP), complete by postnatal day 7 (P7). The retinal vessels then dive to the outer plexiform layer (OPL) to form the deep plexus (DP), complete by P14, and ascend back to the inner plexiform layer (IPL) to form the intermediate plexus (IP), complete by P21[1].

The retinal vasculature develops in response to a complex series of molecular and cellular interactions between the retina's neurons, glia and vascular cells. Retinal neurons have been shown to direct vessel growth through the release and/or regulation of pro-angiogenic factors such as vascular endothelial growth factor (VEGF)[5-8], anti-angiogenic factors such as semaphorins[9, 10] and through interactions with glia[11]. The retina contains three populations of glia that are important for development and maintenance of the retinal vasculature; Müller cells (MCs), astrocytes and microglia. MCs are derived from retinal progenitors and are the last population of cells to be born within the retina[12]. During

development, MCs release VEGF in response to neural induced hypoxia[13] and are thought to provide scaffolding along which endothelial cells migrate during development[1]. Mature MCs project radial processes spanning the retina forming the outer and inner limiting membranes. Tangential MC processes wrap blood vessels to help make up the blood-retina-barrier (BRB), and also play a role at neural synapses[14]. Astrocytes and microglia migrate into the retina through the ONH during development[15, 16]. Upon entry, astrocytes proliferate and migrate centrifugally across the laminin rich surface of the retina and provide a template directing the migration of endothelial cells in mice[17, 18]. After development, astrocytes serve to stabilize vessels through the release of VEGF[19] and wrap superficial vessels to help make up the BRB[11]. Microglia promote branching of superficial vessels during development and are thought to play a role in directing vessel growth into the retina[16]. The initial invasion and subsequent formation of the superficial vessels has been well studied; however, much less is known about mechanisms responsible for attracting and organizing the intraretinal vessels forming the deep and intermediate plexi.

In this study, we test the role of neuron placement on intraretinal vascular development using mouse models in which neuron placement within the inner retina is disrupted. Retinal neurons are organized in three cellular layers: the outer nuclear layer (ONL), inner nuclear layer (INL) and retinal ganglion cell layer (RGL); and two synaptic layers: the OPL and IPL, all of which are notable for their stereotypic organization into alternating laminae[20, 21]. Disorganization of ONL lamination and vascular defects has been documented in humans and mice carrying *Crumbs1* mutations[22]. Similarly, we report abnormal angiogenesis and intraretinal bleeding associated with laminar disruption within the inner retina.

In this study, we find significant differences in the organization of blood vessels in retinas with ectopic neurons within the IPL (*Bax* mutants) and in those with highly disrupted neuron patterning within the inner retina (*Dscam* mutants). The latter also exhibits frequent intraretinal bleeding. Using *Fat3* mutant mice, which contain an additional plexiform lamina, and using *Dscam* gain-of-function (*Dscam*^{GOF}) mice, in which vessel branching occurs at the INL/IPL interface yet lack an IP, we provide experimental evidence that vessel branching occurs at the neuron-neurite interface. Next, we tested the relative contribution of glial organization and neuron misplacement to vessel organization defects. Glial organization was largely maintained in retinas with misplaced neurons. The displacement of neurons in the *Dscam* mutant retina results in the ectopic expression and localization of

angiogenic factors suggesting a mechanism by which displaced neurons could deflect growing vessels, resulting in fragile growing vessels and intraretinal bleeding.

MATERIALS AND METHODS

Mouse Strains and Handling: Mice were handled in accordance with protocols approved by the Animal Care and Use Committees at the University of Idaho and the University of Utah and with the ARVO Statement for the Use of Animals in Ophthalmic and Vision Research. *Dscam*$^{-/-}$ mice: The *Dscam*^{2J} (The Jackson Laboratory, Bar Harbor, ME; stock number: 006038)[23] and *Dscam* FD[24] loss of function alleles were used in this study. *Dscam*^{GOF} mice were previously generated[25] and are available through the Jackson Laboratory (stock number: 025543). *Bax* mutant mice were obtained from The Jackson Laboratory (stock number: 002994) and *Fat3* mutant retinas were provided by Dr. Michael Deans (University of Utah)[26].

Immunohistochemistry: Tissues were prepared as previously described[25].

Antibodies and Stains: *Primary antibodies:* mouse anti-Glutamine Synthetase (GS) (Millipore, Darmstadt, Germany; MAB302; 1:1000), mouse anti-Glial Fibrillary Acidic Protein (GFAP) (Cell Signaling Technology, Danvers, MA; 3670; 1:200), rabbit anti-GFAP (Dako, Carpinteria, CA; Z0334; 1:500), rabbit anti-IBA-1 (Wako, Richmond, VA; 019-19741; 1:500), rabbit anti-VEGF (Santa Cruz Biotechology, Santa Cruz, CA; A20; 1:200), mouse anti-PAX6 (developed by Kawakami, Developmental Studies Hybridoma Bank; 1:500) and rabbit anti-Vimentin (abcam, Cambridge, MA; ab45939; 1:300). *Secondary antibodies:* Secondary antibodies were used at 1:500 RT or 1:1000 4º C overnight (Jackson ImmunoResearch, West Grove, PA). *Stains:* Isolectin GS-B4 Alexa 568 (Invitrogen, Grand Island, NY; I21412; 1:200), DAPI (Cell Signaling Technology; 4083; 1:50,000 from 1mg/ml stock), DRAQ5 (Thermo Scientific, Waltham, MA; 62251; 1:2000).

Microscopy: Micrographs were captured from a Nikon or Olympus spinning disk confocal microscope, an Olympus Flouview scanning laser confocal microscope, a Leica Stereoscope, or Leica DMR microscope. Adobe Photoshop and FIJI were used to process

images. Any modifications to the brightness or contrast of images were performed uniformly across the image, in accordance with journal policies.

Cell Counts: *Neurons*: Thickness of the cellular layers was quantified as previously described[25]. *Müller cells*: Density was quantified in sections stained with DAPI and GS. Numbers were normalized per unit length of retina. *Microglia:* Density was quantified in whole retinas stained with IBA-1. Images were captured through the entire retina at 1 µm increments along the z-axis and were then split into microglia found in the IPL or OPL based upon physical separation of cell bodies. These counts were normalized per unit volume in the IPL and per unit area in the OPL. In all counts, the peripheral and central retina were sampled equally and were quantified at P28.

Vessel Density: Vessel density was quantified in P28 whole retinas stained with GS isolectin. Images were captured through the entire retinal vessels at 1 µm increments along the z-axis. Twelve images were captured from each retina (4 central, 4 mid, and 4 peripheral). Image stacks were imported into FIJI and were traced with the plugin, Simple Neurite Tracer[27]. For each image stack, the total length of vessels was normalized per unit volume.

Plexus and Astrocyte Coverage: P28 whole retinas stained with GS isolectin or GFAP were imaged and sampled at 1 µm along the z-axis. Eight images were captured from each retina (4 central and 4 peripheral). Images stacks were then imported into FIJI and z-projections were generated. Vessels found within the IPL of *Bax*$^{-/-}$ and the INL of *Fat3*$^{-/-}$ retinas were not included in the analysis. The intermediate plexus data for *Dscam*$^{-/-}$ and *Dscam*^{GOF} retinas includes everything between the SP and DP. The percent coverage was then measured in FIJI from the z-projection images.

Blood vessel and Müller cell radial process orientation: P28 retina sections stained with DAPI and GS isolectin or GS were imaged and imported into FIJI, where the orientation within the IPL was measured with respect to the nerve fiber layer (NFL). Each recorded orientation was classified as one observation and the data was converted to the percentage of observations at a particular angle in 10° increments.

Blood vessel branch points (BPs): P28 retina sections stained with DAPI and GS isolectin were imaged and imported into FIJI. All BPs within a section were identified and recorded based upon location within the different laminae of the retina. The IPL was further divided into S1-S5, according to convention established by Ramon y Cajal[28]. BPs found within S1 were considered to be found within the IP. BPs found in S2-S5 were considered to be found within the IPL. The data were then converted to the percentage of BPs found within the different laminae for a given retina section.

Nuclei to nearest vessel measurement: P14 *Dscam*$^{-/-}$ whole retinas stained with DRAQ5, GS isolectin and IBA-1 were imaged on a confocal microscope and imported into Bitplane's Imaris. Images were sampled equally from the peripheral and central retina to capture two developmental time-points. Within Imaris, the images were digitally reconstructed as surfaces and spots for the vessels and nuclei, respectively. Spots within the IPL were then isolated and classified. Endothelial nuclei were identified by their elongated shape and their location within GS isolectin, microglia by IBA-1, and the remainder were classified as neurons. The distance transformation function was then used to measure the closest surface (blood vessel) to each of the spots (nuclei) within the IPL. As a randomized control, blood vessels were flipped along the horizontal axis to randomize the location of nuclei and the measurements were repeated. Spots encapsulated by vessels in the flipped control were excluded from the analysis.

Protein Extraction and Western Blot: Protein was extracted from P14 retinas from *Dscam* mutants and wild type littermate controls using mem-PER Eukaryotic Protein Extraction Reagent Kit (Thermo Scientific, Rockford, IL). 20 µg of total protein was loaded into each lane and were separated using a 10% acrylamide gel. Blots were transferred to PVDF membranes (Bio-Rad Laboratories, Hercules, CA; 162-0174) and blocked in TBST (0.05% Tween) and 3% non-fat dry milk. Blots were probed with rabbit anti-VEGF antibody (Santa Cruz Biotechology; 1:1000) for 75 min room temperature (RT) followed by four 5 min washes in TBST at RT. Anti-VEGF was detected using goat anti-rabbit HRP linked antibody (Cell Signaling Technology; 7074; 1:25,000), diluted in 3% milk. Blots were then washed four times for 5 min in TBST at RT. Immoblin Western Chemiluminescent HRP Substrate Kit (Millipore) was used to detect antibodies. Blots were then striped and re-probed with rabbit anti-GAPDH antibody (Synaptic Systems, Goettingen, Germany; 247002; 1:1000) and detected with anti-rabbit HRP linked antibody (Cell Signaling Technology). Steps for

anti-GAPDH were performed identical to anti-VEGF. Densitometry was performed using FIJI to calculate the relative densities between anti-VEGF and anti-GAPDH.

***In-situ* hybridization:** Probes were generated as previously described[29] with the following modifications. Primers to make to make probe templates: *Vegfa* forward (TGTCTACCAGCGAAGCTACT), *Vegfa* reverse (TCGTTTAACTCAAGCTGCCT), *Vegfr2* forward (ATTCAGAGCGATGTGTGGTC), *Vegfr2* reverse (GTCTGTCTGGCTGTCATCTG), *Sema3C* forward (ATCGGCAGTGTGTGTGTATC), *Sema3C* reverse (GAACCTAGAGCAAGAGTGGC), *Sema3E* forward (GGCAAGTATGGAACCACCAA), *Sema3E* reverse (CTGGAGCAGGATATGCCATC). *In-vitro* transcription mixture was composed of 1 µg cDNA, 4 µl 10x T7 or SP6 buffer (Roche), 4 µl T7 or SP6 RNA polymerase (Roche), 1 µl RNase inhibitor (Roche), 4 µl digoxyigenin or fluorescein dNTPs (Roche) and RNase free water to 40 µl. Samples were incubated at 37 ºC overnight and 4 µl LiCl, 4 µl ETDA and 150 µl EtOH was added to the samples. RNA was chilled at -80 ºC and re-suspended in 20 µl of RNase free water.

Tissues for hybridization were prepared by fixing P14 from *Dscam* mutant and wildtype littermate enucleated and hemisected eyes (cornea and lens removed) in 4% paraformaldehyde with 5% sucrose at RT for 30 min. Retinas were then dissected out of the eye cup and washed three times 10 min in phosphate buffer with 5% sucrose. Tissues were cryopreserved by equilibrating them in 30% sucrose and then embedded and frozen down in a 2:1 mixture of OCT:30% sucrose. Tissues were sectioned at 6 µm using a cryostat and were placed onto charged slides. Slides were then dried overnight in a desiccator at RT. Hybridization was prepared as previously described[30, 31].

RESULTS

Blood leakage in developing Dscam mutant retinas

A varying degree of intraretinal bleeding was observed within 52% of developing retinas in mice lacking *Dscam* (*Dscam*$^{-/-}$) between P16 and P20, (Figure 2.1 A-B), a time point when intraretinal vessels are forming[1]. Histological staining of *Dscam*$^{-/-}$ retinas revealed that this bleeding occurred within the inner retina (Figure 2.1 C-D). Up-regulation of GFAP was observed within MCs within the bloody patches (Figure 2.1 E-E'), as well as, an infiltration of IBA-1 positive microglia (Figure 2.1 F). Intraretinal bleeding was observed

in mice in which the *Dscam* gene was conditionally targeted in the retina with *Pax6α-Cre*, indicating that this phenotype was not secondary to hydrocephalus that occurs in *Dscam* mutants[32] (Supplemental Figure 2.1). Intraretinal bleeding was not observed in adult *Dscam* mutants (age >P35), indicating that the integrity of the vascular network was eventually established in these mice. Consistent with this, a significant increase in blood vessel growth cones was detected at P28 in *Dscam*$^{-/-}$ mice, a time point when angiogenesis is largely complete in the wild type (*WT*) retina (Figure 2.1 G-I).

*D*scam is not expressed by cells of the vasculature or glia[33], but rather is required for neuron patterning and developmental cell death within retinal neurons[29]. Because the neural retina begins to develop before vessels invade the inner retina, we hypothesized that cues from the neural retina or glia act to provide guideposts that are utilized by developing blood vessels and that abnormalities in retinal lamination could potentially drive the observed vascular pathology.

Genetic approach to vary neuron placement

Mouse mutants in which neuron number and lamination are disrupted were assembled to test the hypothesis that neurons facilitate blood vessel organization. The *Bax* mutant retina (*Bax*$^{-/-}$) has an increase in cell number and misplacement of neurons in the IPL as a result of a defect in developmental cell death (Figure 2.2 B). Neuron cell number in the *Bax*$^{-/-}$ mutant retina is similar to that observed in *Dscam*$^{-/-}$ retina (Figure 2.2 C), the latter which also features uneven INL lamination[25, 34]. Cell number is similar to the *WT* in the *Fat3* mutant retina (*Fat3*$^{-/-}$); however, ectopic plexiform laminae form within the INL and just below the RGL in *Fat3*$^{-/-}$ retinas, termed the outer and inner misplaced plexiform layer (OMPL and IMPL), respectively (Figure 2.2 D)[26]. Some neurons normally found within the INL are mislocalized to the RGL[26]. Quantification of cell numbers was consistent with previous publications (Figure 2.2 E)[25, 26, 34].

Vessel disorganization correlates with laminar (dis)organization

The adult retinal vasculature consists of three capillary networks, or plexi: the SP, IP and DP. We measured if the formation of these plexi was normal across these mutant

strains at an age when their development is complete, P28 (Figure 2.3). The DP develops normally in the *Bax*$^{-/-}$ and *Fat3*$^{-/-}$ retinas. *Dscam*$^{-/-}$ retinas have significantly reduced DP coverage compared to *Bax*$^{-/-}$ and *Fat3*$^{-/-}$ retinas (Figure 2.3 A-E and P-S). Formation of the IP was normal within *Bax*$^{-/-}$ and *Fat3*$^{-/-}$ retinas, compared to *WT* (Figure 2.3 F-G, I-J, P-Q and S). *Dscam*$^{-/-}$ retinas lacked a defined IP (Figure 2.3 H, J and R). While the SP was normal within all of the models, vessel coverage was significantly increased in the *Bax*$^{-/-}$ retina compared to all strains (Figure 2.3 K-O and P-S). Additionally, ectopic vessels were observed running parallel to the plexi within *Bax*$^{-/-}$ and *Fat3*$^{-/-}$ retinas in areas correlated to the IPL and OMPL respectively (Figure 2.3 Q and S, arrows).

We next asked whether the total density of vessels reflected the neural densities within the different strains. Calculation of vessel densities revealed a significant increase in vessel density in *Bax*$^{-/-}$ retinas compared to all other strains (Figure 2.3 T).

The interplexus vessels connecting the three plexi were then analyzed (Figure 2.3 P-S and Figure 2.4 A-F). Measuring the trajectory these vessels took when traveling through the retina demonstrated that the majority of vessels projected perpendicular within *WT* and *Fat3*$^{-/-}$ retinas (Figure 2.4 A and D-F). Vessels in *Bax*$^{-/-}$ retinas followed a similar trend except that statistically more vessels within the IPL were found running parallel to the retinal laminae, when compared to *WT* and *Fat3*$^{-/-}$ retinas (Figure 2.4 B and E-F). Vessels within *Dscam*$^{-/-}$ retinas followed a more tortuous trajectory with statistically less perpendicular vessels and statistically more running between 0-60º and 120-180º, when compared to *WT* and *Fat3*$^{-/-}$ retinas (Figure 2.4 C and E-F). No statistical differences were detected between *Bax*$^{-/-}$ and *Dscam*$^{-/-}$ retinas. This is probably due to how the data was lumped together in increments of 60º for statistical analysis. Interplexus branching was also examined (Figure 2.4 G). The majority of vessel branch points (BPs) within *WT* retinas occurred at locations spatially correlated to the three vascular plexi (Figure 2.4 G). A significant increase in BPs was detected within the IPL of *Bax*$^{-/-}$ retinas (Figure 2.4 G). BPs within *Dscam*$^{-/-}$ retinas were distributed uniformly throughout the retinal laminae (Figure 2.4 G). A significant increase in BPs was detected within the INL of *Fat3*$^{-/-}$ retinas, 93% of these falling within the OMPL (Figure 2.4 G).

After observing defects in the formation of IP in *Dscam*$^{-/-}$ retinas we decided to analyze the retinal vasculature within mice that overexpress *Dscam* (*Dscam*^{GOF}) at P28 (Figure 2.5). In *Dscam*^{GOF} retinas, the ectopic and overexpression of *Dscam* results in a

significantly thinner retina compared to all other strains (Figure 2.5 A and I)[25]. *Dscam*^{GOF} retinas maintained formation of the DP and SP (Figure 2.5 B-C and G), although the coverage of the DP was significantly reduced compared to all strains and coverage of the SP was significantly reduced compared to *Bax*$^{-/-}$ (Figure 2.5 D and H). Interestingly, *Dscam*^{GOF} retinas lacked an IP (Figure 2.5 B and E), even though vessels continued to branch at the neuron-neurite interface between the INL and IPL (Figure 2.5 B and E, arrows). The orientation of interplexus connections ran perpendicular to the plexi and continued to branch at areas spatially correlated to where the three plexi should form (Figure 2.5 J and K).

Taken together, these data provide evidence that displacement of neurons in the IPL of the *Dscam*$^{-/-}$ and *Bax*$^{-/-}$ retina result in misprojection of vessels through the IPL. Moreover, the presence of an ectopic plexus lamina in the *Fat3*$^{-/-}$ retina and branching of vessels in the *Dscam*^{GOF} at the INL/IPL junction, implicate the neuron-neurite interface as a point of vessel branching.

Having characterized the organization of the retinal vessels in *Bax*, *Dscam* and *Fat3* mutant retinas, we next set out to determine if disorganization of cell types associated with vascular development could explain these results.

Astrocytes

Whole retinas were stained with GFAP to visualize the morphology and density of astrocytes at P28 (Figure 2.6)[35]. Astrocytes were morphologically normal within *Bax*$^{-/-}$ and *Dscam*$^{-/-}$ retinas (Figure 2.6 A-C), while astrocytes within *Fat3*$^{-/-}$ retinas contained globe shaped projections at some of their tips (Figure 2.6 D) that filled in areas where the inner limiting membrane was discontinuous (Figure 2.6 D'-D''). Astrocytes continued to wrap vessels in all genotypes. The coverage of astrocytes was determined through confocal microscope images of GFAP staining within the NFL and RGL. A correlation between neural densities within the RGL of our genetic models (Figure 2.2 E) and their corresponding astrocyte coverage (Figure 2.6 E) was found, consistent with previous studies[36-38].

Müller Cells

The density and morphology of MCs was assayed by staining sections of retina with GS and vimentin at P28 (Figure 2.7)[39, 40]. No significant differences in the density of MCs or the trajectory at which MC radial processes project was detected when comparing all models (Figure 2.7 Q-R). When assaying the morphology of the tangential processes, we discovered that these processes were confined to neurite containing laminae in all genotypes (Figure 2.7 M-P). This is most apparent in the IPL of *Dscam*$^{-/-}$ retinas, where MC processes were observed abutting but not invading the INL or RGL (Figure 2.7 G and O), and was further corroborated in the *Fat3*$^{-/-}$ retina where tangential processes were found within the OMPL (Figure 2.7 H and P). GFAP was detected in MCs of *Bax*$^{-/-}$, *Dscam*$^{-/-}$, *Fat3*$^{-/-}$ retinas and confirmed with vimentin staining (Figure 2.7 M-O and not shown).

Microglia

To assay microglia organization, P28 retinas were stained with IBA-1 (Figure 2.8)[41]. Microglia are located within neurite containing laminae of the retina: the OPL, IPL and the OMPL of *Fat3*$^{-/-}$ retinas (Figure 2.8 A-D). Significant increases in microglia density compared to *WT* were found in all strains, except within the IPL when comparing *WT* to *Fat3*$^{-/-}$ (Figure 2.8 I and N).

Neurons

Next, we tested whether the displaced neurons within the IPL of *Dscam*$^{-/-}$ retinas correlated with misdirection of vessels and if this interaction was attractive or repulsive. To test this, whole *Dscam*$^{-/-}$ retinas were stained with GS isolectin, DRAQ5 and IBA-1 and then imaged with a confocal microscope at P14, a time-point when intermediate vessels are forming[1] and slightly before intraretinal bleeding was observed in *Dscam* mutants (Figure 2.9 A and C). We then mapped vessels spanning the IPL and the location of displaced neurons and microglia (Figure 2.9 B, D-F). The distance between vessels and the nearest displaced neuron or microglia was measured and plotted compared to a control in which the vessels were flipped along the horizontal axis (Figure 2.9 G-H) (See Materials and Methods). Both neurons and microglia were statistically closer to vessels than the flipped

controls suggesting that neural somata and/or microglia are attracting vessel growth (Figure 2.9 H). Microglia were statistically closer to vessels than neural somas in both the peripheral and central retina (Figure 2.9 H).

Neuron placement affects the expression patterns of angiogenic factors.

We next wanted to test whether the displacement of neurons within the inner retinas of *Dscam*$^{-/-}$ mice could alter the expression patterns of angiogenic factors, which could in turn explain vascular defects within the inner retina. *In-situ* hybridization was performed on *Dscam*$^{-/-}$ retinas and littermate controls at P14 to visualize expression patterns of four angiogenic factors that are critical during retinal angiogenesis: *Vegfa*[1, 5, 6, 13, 19, 42], *Vegfr2* (KDR/Flk-1)[8], *Sema3C*[43] and *Sema3E*[9, 44] (Figure 2.10).

In *WT* and *Dscam*$^{-/-}$ retinas, *Vegfa* was highly expressed by cells within the middle of the INL, likely MCs, consistent with a previous study[13]. Expression of *Vegfa* was also observed to a lesser extent within most neurons of the INL and RGL (Figure 2.10 A-B), and in displaced neurons of *Dscam*$^{-/-}$ retinas (Figure 2.10 B, arrowheads). Expression of *Vegfr2* was also observed at high levels within cells central to the INL in the *WT* retina. This pattern was less distinct in *Dscam*$^{-/-}$ retinas. Expression of *Vegfr2* was found in most neurons of the INL and RGL in *WT* and *Dscam*$^{-/-}$ retinas (Figure 2.10 C-D), and again within displaced neurons of *Dscam*$^{-/-}$ retinas (Figure 2.10 D, arrowheads). Ectopic expression of *Vegfr2* was also detected within the INL of *Dscam*$^{-/-}$ retinas. Expression of *Sema3C* was observed throughout the retina (Figure 2.10 E-F), including displaced neurons in the *Dscam*$^{-/-}$ retina (Figure 2.10 F, arrowheads). Expression of *Sema3E* was observed in neurons in the RGL and to a lesser extent in the INL of both *WT* and *Dscam*$^{-/-}$ retinas (Figure 2.10 G-H), and within displaced neurons of *Dscam*$^{-/-}$ retinas (Figure 2.10 H, arrowheads). No staining was observed when probing retinas with mRNA sense probes (Supplemental Figure 2.2).

VEGF concentration gradients are influenced by neuron placement

The observations of altered expression patterns of *Vegfa* and *Vegfr2,* along with a recent study uncovering that VEGFR2 functions to titrate VEGF and prevent angiogenesis during early development[8] brought us to ask the question, are VEGF concentration

gradients altered in *Dscam* mutants? To test this, immunohistochemistry was performed to visualize the distribution of VEGF protein throughout *Dscam*$^{-/-}$ retinas and littermate controls at P14 (Figure 2.11). In *WT* and *Dscam*$^{-/-}$ retinas, diffuse VEGF staining was observed throughout the entire retina excluding the ONL (Figure 2.11 A-B'). More intense VEGF immunoreactivity was observed on the surface of cell bodies, including displaced cell bodies in *Dscam*$^{-/-}$ retinas, compared to the IPL neurites.

To identify which type of cells within the IPL were accumulating more VEGF relative to the neurites, P14 retina sections were stained with DRAQ5, VEGF and PAX6, a marker for neurons[45]. Nuclei within the IPL of *WT* and *Dscam*$^{-/-}$ retinas were then quantified and sorted by makers for which they were positive (Figure 2.11 E). Our results indicate that all cell bodies accumulating VEGF on their surface were PAX6 positive, but not all PAX6 positive cells accumulated VEGF, suggesting that a subset of neurons regulate VEGF localization during IP formation. Western blot was performed to quantify the amount of VEGF protein within *Dscam*$^{-/-}$ retinas compared to *WT* littermates at P14. No significant differences in the amount of relative VEGF protein was detected (Figure 2.11 F).

DISCUSSION

Retinal neovascularization and vascular patterning defects result in blinding retinal diseases. Changes in the neural retina in these diseases can initiate the growth of new vessels through the process of angiogenesis[46]. A better understanding of the basic principles regulating angiogenesis during development will help elucidate what is occurring during vascular proliferative diseases causing blindness.

In this study, we set out to address the origin of retinal bleeding in *Dscam* mutant mice. We find that 1) abnormalities in neuron lamination in the inner retina can promote pathological angiogenesis, 2) disrupting neural lamination leads to significant patterning changes in blood vessels, 3) the neuron-neurite interface is a point of vessel branching, 4) the displacement of neurons and microglia correlates with an attractive misdirection of growing vessels and 5) the displacement of neurons is sufficient to alter the expression and localization of angiogenic factors.

Neuron Disorganization and Retinal Angiogenesis

Developmental retinal lamination defects and vascular abnormalities are observed in heritable retinal dystrophies, such as retinitis pigmentosa (RP) and Leber congenital amaurosis (LCA) and are caused by mutations in the *Crumbs homologue 1* (*CRB1*) gene[22]. *CRB1* is required for retinal lamination structuring within both human and mouse outer retinas[22]. In humans, the loss of *CRB1* is associated with retinal lamination defects within LCA patients[47], and vascular abnormalities leading to edema and retinal detachment within RP patients[48]. In *CRB1* mutant mouse models, structural alterations in the OLM result in the restructuring of the outer retina in the formation of pseudorosettes and retinal folding[49, 50]. Similarly, we identify that developmental alterations in neural lamination within inner portions of *Dscam*$^{-/-}$ retinas cause abnormalities in the patterning and integrity of vessels as they develop. Taken together, these observations suggest that developmental, disease and age related changes in neural lamination could promote abnormal vascular growth and retinal bleeding.

Neuron Disorganization Mislocalizes Angiogenic Factors

In the mouse, retinal vessels form via a process of angiogenesis and their growth is guided by secreted molecules that act to attract or repel growing blood vessels[51]. A growing body of literature has begun to uncover that angiogenesis is regulated by similar molecules and mechanisms to that of the nervous system and that the vascular and nervous systems often engage in cross-talk during development and disease[51]. Therefore, regulating the balance and expression of these shared factors is important for proper development and maintenance of these systems. Moreover, the highly organized retina serves as an ideal model for understanding these principles.

VEGF is a key regulator of angiogenesis[52]. Within the retina, VEGF is required for the initiation of angiogenic sprouts, arteriole vs. venous fate determination, and vessel stabilization[1, 13, 19, 42]. During the initial development of the superficial vessels, neurons have been shown to regulate VEGF activity through VEGFR2 induced engulfment of VEGF preventing immature vessel sprouting into the retina[8]. As development proceeds, neural derived VEGF has been shown to regulate the formation of the intraretinal vessels[5, 6].

These studies begin to illustrate the importance of neural regulation on VEGF bioavailability and how this regulation changes overtime, presumably to aid with vessel patterning.

Our results implicate an additional requirement to this regulation, that is, the placement of neurons. During development of the IP in *WT* retinas, we observed accumulation of VEGF on the surface of neural somas abutting the INL. In other model systems, a capture and presentation mechanism has been well documented such as: Netrins for axon guidance in *Drosophila*[53, 54], UNC-6 for axon guidance and dendrite repulsion in *C. elegans*[55, 56] and F-spondin for axon guidance in chick[57]; where, a diffusible guidance molecule is captured and presented to growth cones allowing multicellular organisms to tightly regulate the growth of axons and dendrites. Perhaps formation of the IP in the retina utilizes a similar mechanism, where neurons abutting the IPL accumulate MC and neural derived VEGF and present it to vessel growth cones promoting vessel branching and ramification at the neuron-neurite interface. In *Dscam* mutants, we find the displacement of neurons is sufficient to mislocalize the distribution of VEGF and that the cell surface accumulation of VEGF is largely absent in the INL and abundant in displaced neurons throughout the IPL.

Semaphorins are a class of repelling guidance molecules originally found to be important for nervous system development and have recently been shown to be important for angiogenesis[51]. During blood vessel growth, secreted semaphorins modulate delta-like 4 (Dll4)-notch signaling disrupting tip/stalk cell determination and causing cytoskeletal destabilization, preventing the growth of vessels in a particular direction or all together[58]. In our study, we analyzed the expression patterns of two secreted semaphorins known to be important for angiogenesis in the retina, *Sema3C*[43] and *Sema3E*[9, 44]. We find that both of these are highly expressed normally in the retina and that these are almost always expressed by displaced cells in *Dscam* mutants.

A possible model to explain the disorganization of intraretinal vessels in *Dscam* mutants is that the displacement of neurons leads to lack of a distinct VEGF cue that normally promotes vessel branching and ramification and is exacerbated by the misexpression of repulsive semaphorin cues leading to vascular defects and retinal bleeding. Future studies targeting VEGF, VEGF receptors, and semaphorins will be performed to test this hypothesis.

Glia and the Retinal Vasculature

The retina contains three types of glia that are intimately linked to the retinal vasculature: astrocytes, MCs and microglia. Interactions between these cells, along with neurons and cells of the vasculature, are required to form the neurovascular unit. Associated changes in neurons and glia have been reported in pathological conditions of the retina; however, a cause and effect relationship is yet to be resolved[59]. In this study, we observe changes in the organization of these populations in mutant strains with abnormal neural organization within the inner retina, suggesting a role for neurons in initiating and maintaining these cellular interactions.

Astrocytes were the least affected glia population in our mutant strains. We found a correlation between neural densities within the RGL and astrocyte densities, consistent with previous reports demonstrating that PDGF released by neurons promotes astrocyte growth[36, 37] and that depletion of retinal ganglion cells results in decreased astrocyte populations[38]. Astrocyte gross morphology appeared to be unaffected by neuron organization because astrocytes were found within the NFL of all our mutant stains and their processes wrapped superficial vessels. It can be reasoned that the globe shaped projections at the tips of *Fat3*$^{-/-}$ astrocytes follow misprojected neurites from neurons forming the IMPL. However, these changes were not reflected by the retinal vessels.

During development, hypoxia drives the expression and release of VEGF from MCs and it is thought the MCs provide structural support for the migration of endothelial cells during vessel formation[1, 13]. Mature MC tangential processes wrap retinal vessels to help form the BRB[11]. Selective ablation of MCs in the adult retina leads to severe changes in the organization of retinal vessels, breakdown of the BRB and eventually intraretinal neovascularization[60]. We found that the radial processes of MCs were unaffected by neural lamination, while the tangential processes were redirected toward ectopic neurites. However, no considerable changes were observed in MCs that could describe vascular defects.

We also identified changes to microglia organization in our mutant stains. We found that microglia limit themselves to the neurite containing laminae within the retina and frequently find them at the neuron-neurite interface. Microglia are known to regulate the branching of developing superficial vessels[16]. A potential model to explain the branching pattern observed at the neuron-neurite interface in this study is that microglia position

themselves at the neuron-neurite interface and promote branching of vessels at this interface. Microglia depletion studies aimed at differentiating these possibilities will be performed in future studies to address this question.

Conclusion

This study demonstrates the importance of neuronal placement during intraretinal vessel development. Our current working model is that lamination defects cause mispresentation of neural derived factors organizing vascular growth leading to the disorganization of retinal vessels (Figure 2.12). Whether the changes in neural lamination are directly causing changes in vessel development, are secondary to neural driven glial changes, or both remain to be elucidated and is the focus of future experiments.

ACKNOWLEDGEMENTS

The authors would like to thank Ann Norton, the director of the optical imaging core at the University of Idaho, for her support and training with imaging and Bitplane's Imaris. The authors would also like to thank Joshua Sukeena and Carlos Galicia for their help with *in-situ* hybridization. This research was supported by the National Eye Institute Grant EY020857 (PGF) and EY021146 (MRD). Imaging support was provided by NIH Grant Nos. P20 RR016454 (PGF), P30 GM103324-01 (PGF) and P20 GM103408 (PGF).

REFERENCES

1. Fruttiger M. Development of the retinal vasculature. *Angiogenesis* 2007;10:77-88.
2. Mehta S. Age-Related Macular Degeneration. *Primary care* 2015;42:377-391.
3. Hellstrom A, Smith LE, Dammann O. Retinopathy of prematurity. *Lancet* 2013;382:1445-1457.
4. Lutty GA. Effects of diabetes on the eye. *Investigative ophthalmology & visual science* 2013;54:ORSF81-87.

5. Kurihara T, Westenskow PD, Bravo S, Aguilar E, Friedlander M. Targeted deletion of Vegfa in adult mice induces vision loss. *The Journal of clinical investigation* 2012;122:4213-4217.
6. Usui Y, Westenskow PD, Kurihara T, et al. Neurovascular crosstalk between interneurons and capillaries is required for vision. *The Journal of clinical investigation* 2015;125:2335-2346.
7. Luo L, Uehara H, Zhang X, et al. Photoreceptor avascular privilege is shielded by soluble VEGF receptor-1. *eLife* 2013;2:e00324.
8. Okabe K, Kobayashi S, Yamada T, et al. Neurons limit angiogenesis by titrating VEGF in retina. *Cell* 2014;159:584-596.
9. Kim J, Oh WJ, Gaiano N, Yoshida Y, Gu C. Semaphorin 3E-Plexin-D1 signaling regulates VEGF function in developmental angiogenesis via a feedback mechanism. *Genes & development* 2011;25:1399-1411.
10. Buehler A, Sitaras N, Favret S, et al. Semaphorin 3F forms an anti-angiogenic barrier in outer retina. *FEBS letters* 2013;587:1650-1655.
11. Vecino E, Rodriguez FD, Ruzafa N, Pereiro X, Sharma SC. Glia-neuron interactions in the mammalian retina. *Progress in retinal and eye research* 2015.
12. Agathocleous M, Harris WA. From progenitors to differentiated cells in the vertebrate retina. *Annual review of cell and developmental biology* 2009;25:45-69.
13. Stone J, Itin A, Alon T, et al. Development of retinal vasculature is mediated by hypoxia-induced vascular endothelial growth factor (VEGF) expression by neuroglia. *The Journal of neuroscience : the official journal of the Society for Neuroscience* 1995;15:4738-4747.
14. Kolb H. Glial Cells of the Retina. In: Kolb H, Fernandez E, Nelson R (eds), *Webvision: The Organization of the Retina and Visual System.* Salt Lake City (UT); 1995.
15. Watanabe T, Raff MC. Retinal astrocytes are immigrants from the optic nerve. *Nature* 1988;332:834-837.
16. Arnold T, Betsholtz C. Correction: The importance of microglia in the development of the vasculature in the central nervous system. *Vascular cell* 2013;5:12.
17. Dorrell MI, Aguilar E, Friedlander M. Retinal vascular development is mediated by endothelial filopodia, a preexisting astrocytic template and specific R-cadherin adhesion. *Investigative ophthalmology & visual science* 2002;43:3500-3510.

18. Gnanaguru G, Bachay G, Biswas S, Pinzon-Duarte G, Hunter DD, Brunken WJ. Laminins containing the beta2 and gamma3 chains regulate astrocyte migration and angiogenesis in the retina. *Development* 2013;140:2050-2060.
19. Scott A, Powner MB, Gandhi P, et al. Astrocyte-derived vascular endothelial growth factor stabilizes vessels in the developing retinal vasculature. *PloS one* 2010;5:e11863.
20. Sanes JR, Zipursky SL. Design principles of insect and vertebrate visual systems. *Neuron* 2010;66:15-36.
21. Masland RH. The neuronal organization of the retina. *Neuron* 2012;76:266-280.
22. Richard M, Roepman R, Aartsen WM, et al. Towards understanding CRUMBS function in retinal dystrophies. *Human molecular genetics* 2006;15 Spec No 2:R235-243.
23. Fuerst PG, Harris BS, Johnson KR, Burgess RW. A novel null allele of mouse DSCAM survives to adulthood on an inbred C3H background with reduced phenotypic variability. *Genesis* 2010;48:578-584.
24. Fuerst PG, Bruce F, Rounds RP, Erskine L, Burgess RW. Cell autonomy of DSCAM function in retinal development. *Developmental biology* 2012;361:326-337.
25. Li S, Sukeena JM, Simmons AB, et al. DSCAM promotes refinement in the mouse retina through cell death and restriction of exploring dendrites. *The Journal of neuroscience : the official journal of the Society for Neuroscience* 2015;35:5640-5654.
26. Deans MR, Krol A, Abraira VE, Copley CO, Tucker AF, Goodrich LV. Control of neuronal morphology by the atypical cadherin Fat3. *Neuron* 2011;71:820-832.
27. Longair MH, Baker DA, Armstrong JD. Simple Neurite Tracer: open source software for reconstruction, visualization and analysis of neuronal processes. *Bioinformatics* 2011;27:2453-2454.
28. Kolb H. Inner Plexiform Layer. In: Kolb H, Fernandez E, Nelson R (eds), *Webvision: The Organization of the Retina and Visual System.* Salt Lake City (UT); 1995.
29. Fuerst PG, Koizumi A, Masland RH, Burgess RW. Neurite arborization and mosaic spacing in the mouse retina require DSCAM. *Nature* 2008;451:470-474.
30. Nelson SM, Frey RA, Wardwell SL, Stenkamp DL. The developmental sequence of gene expression within the rod photoreceptor lineage in embryonic zebrafish. *Developmental dynamics : an official publication of the American Association of Anatomists* 2008;237:2903-2917.
31. Stevens CB, Cameron DA, Stenkamp DL. Plasticity of photoreceptor-generating retinal progenitors revealed by prolonged retinoic acid exposure. *BMC developmental biology* 2011;11:51.

32. Xu Y, Ye H, Shen Y, et al. Dscam mutation leads to hydrocephalus and decreased motor function. *Protein & cell* 2011;2:647-655.
33. de Andrade GB, Long SS, Fleming H, Li W, Fuerst PG. DSCAM localization and function at the mouse cone synapse. *The Journal of comparative neurology* 2014;522:2609-2633.
34. Harder JM, Libby RT. BBC3 (PUMA) regulates developmental apoptosis but not axonal injury induced death in the retina. *Molecular neurodegeneration* 2011;6:50.
35. Bignami A, Eng LF, Dahl D, Uyeda CT. Localization of the glial fibrillary acidic protein in astrocytes by immunofluorescence. *Brain research* 1972;43:429-435.
36. Fruttiger M, Calver AR, Kruger WH, et al. PDGF mediates a neuron-astrocyte interaction in the developing retina. *Neuron* 1996;17:1117-1131.
37. Fruttiger M, Calver AR, Richardson WD. Platelet-derived growth factor is constitutively secreted from neuronal cell bodies but not from axons. *Current biology : CB* 2000;10:1283-1286.
38. Edwards MM, McLeod DS, Li R, et al. The deletion of Math5 disrupts retinal blood vessel and glial development in mice. *Experimental eye research* 2012;96:147-156.
39. Pixley SK, Kobayashi Y, de Vellis J. A monoclonal antibody against vimentin: characterization. *Brain research* 1984;317:185-199.
40. Haverkamp S, Wassle H. Immunocytochemical analysis of the mouse retina. *The Journal of comparative neurology* 2000;424:1-23.
41. Ito D, Imai Y, Ohsawa K, Nakajima K, Fukuuchi Y, Kohsaka S. Microglia-specific localisation of a novel calcium binding protein, Iba1. *Brain research Molecular brain research* 1998;57:1-9.
42. Stalmans I, Ng YS, Rohan R, et al. Arteriolar and venular patterning in retinas of mice selectively expressing VEGF isoforms. *The Journal of clinical investigation* 2002;109:327-336.
43. Yang WJ, Hu J, Uemura A, Tetzlaff F, Augustin HG, Fischer A. Semaphorin-3C signals through Neuropilin-1 and PlexinD1 receptors to inhibit pathological angiogenesis. *EMBO molecular medicine* 2015;7:1267-1284.
44. Fukushima Y, Okada M, Kataoka H, et al. Sema3E-PlexinD1 signaling selectively suppresses disoriented angiogenesis in ischemic retinopathy in mice. *The Journal of clinical investigation* 2011;121:1974-1985.

45. Sebastian-Serrano A, Sandonis A, Cardozo M, Rodriguez-Tornos FM, Bovolenta P, Nieto M. Palphax6 expression in postmitotic neurons mediates the growth of axons in response to SFRP1. *PloS one* 2012;7:e31590.
46. Lieth E, Gardner TW, Barber AJ, Antonetti DA, Penn State Retina Research G. Retinal neurodegeneration: early pathology in diabetes. *Clinical & experimental ophthalmology* 2000;28:3-8.
47. Jacobson SG, Cideciyan AV, Aleman TS, et al. Crumbs homolog 1 (CRB1) mutations result in a thick human retina with abnormal lamination. *Human molecular genetics* 2003;12:1073-1078.
48. den Hollander AI, Heckenlively JR, van den Born LI, et al. Leber congenital amaurosis and retinitis pigmentosa with Coats-like exudative vasculopathy are associated with mutations in the crumbs homologue 1 (CRB1) gene. *American journal of human genetics* 2001;69:198-203.
49. Mehalow AK, Kameya S, Smith RS, et al. CRB1 is essential for external limiting membrane integrity and photoreceptor morphogenesis in the mammalian retina. *Human molecular genetics* 2003;12:2179-2189.
50. van de Pavert SA, Kantardzhieva A, Malysheva A, et al. Crumbs homologue 1 is required for maintenance of photoreceptor cell polarization and adhesion during light exposure. *Journal of cell science* 2004;117:4169-4177.
51. Carmeliet P. Blood vessels and nerves: common signals, pathways and diseases. *Nature reviews Genetics* 2003;4:710-720.
52. Carmeliet P, Ferreira V, Breier G, et al. Abnormal blood vessel development and lethality in embryos lacking a single VEGF allele. *Nature* 1996;380:435-439.
53. Timofeev K, Joly W, Hadjieconomou D, Salecker I. Localized netrins act as positional cues to control layer-specific targeting of photoreceptor axons in Drosophila. *Neuron* 2012;75:80-93.
54. Hiramoto M, Hiromi Y, Giniger E, Hotta Y. The Drosophila Netrin receptor Frazzled guides axons by controlling Netrin distribution. *Nature* 2000;406:886-889.
55. Asakura T, Waga N, Ogura K, Goshima Y. Genes required for cellular UNC-6/netrin localization in Caenorhabditis elegans. *Genetics* 2010;185:573-585.
56. Smith CJ, Watson JD, VanHoven MK, Colon-Ramos DA, Miller DM, 3rd. Netrin (UNC-6) mediates dendritic self-avoidance. *Nature neuroscience* 2012;15:731-737.

57. Zisman S, Marom K, Avraham O, et al. Proteolysis and membrane capture of F-spondin generates combinatorial guidance cues from a single molecule. *The Journal of cell biology* 2007;178:1237-1249.
58. Gu C, Giraudo E. The role of semaphorins and their receptors in vascular development and cancer. *Experimental cell research* 2013;319:1306-1316.
59. Coorey NJ, Shen W, Chung SH, Zhu L, Gillies MC. The role of glia in retinal vascular disease. *Clinical & experimental optometry* 2012;95:266-281.
60. Shen W, Fruttiger M, Zhu L, et al. Conditional Mullercell ablation causes independent neuronal and vascular pathologies in a novel transgenic model. *The Journal of neuroscience : the official journal of the Society for Neuroscience* 2012;32:15715-15727.

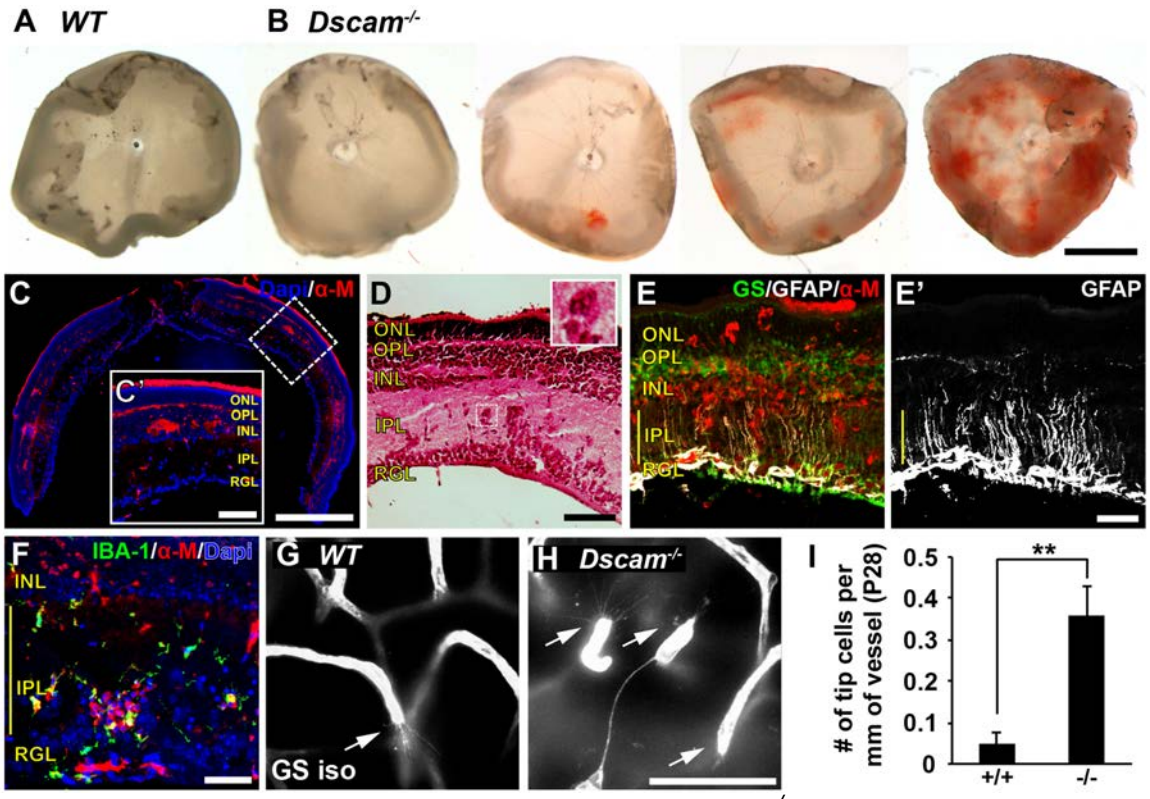

Figure 2.1. Retinal bleeding and glial activation in *Dscam*$^{-/-}$ mice. Retinal bleeding was observed in 52% of *Dscam*$^{-/-}$ retinas between P16 and P20 (n=23). **A)** *WT* retina, no retinal bleeding. **B)** *Dscam*$^{-/-}$ retina, varying amounts of retinal bleeding from none to severe. **C)** Cross section of bloody *Dscam*$^{-/-}$ retina stained with DAPI and α-mouse to visualize locations of bleeding. Retinal bleeding is found within the inner retina. **C')** zoomed in insert of cross section. **D)** Cross section of bloody *Dscam*$^{-/-}$ retina stained with hematoxylin and eosin. Red blood cells can be seen within the retina outside of blood vessels. Inset shows higher magnification of a clump of red blood cells found within the IPL. **E)** Cross section of bloody retina stained with GS, GFAP and α-mouse. **E')** GFAP split out for better visualization. GFAP can be seen throughout MC processes within bloody spots. **F)** Cross section of retina stained with DAPI, IBA-1 and α-mouse. Microglia can be seen in locations where retina is bloody. **G-H)** Images of endothelial tip cells in *WT* and *Dscam*$^{-/-}$ retinas at P28. **I)** Graph illustrating density of tip cells at P28. Very few tip cells were observed in *WT* retinas. Significantly more tip cells were found within *Dscam*$^{-/-}$ retinas. Error bars = SD. Student's *t*-test was used to analyze data. **p<0.002. Abbreviations: α-M: anti-mouse, GFAP: glial fibrillary acidic protein, GS: glutamine synthetase, GS iso: GS isolectin, INL: inner nuclear layer, IPL: inner plexiform layer, ONL: outer nuclear layer, OPL: outer plexiform layer, RGL: retinal ganglion cell layer. Scale bar in B = 1 mm; C = 500 μm; C' = 100 μm; D = 100 μm E' = 50 μm; H = 50 μm. Inset in D = 40x40 μm.

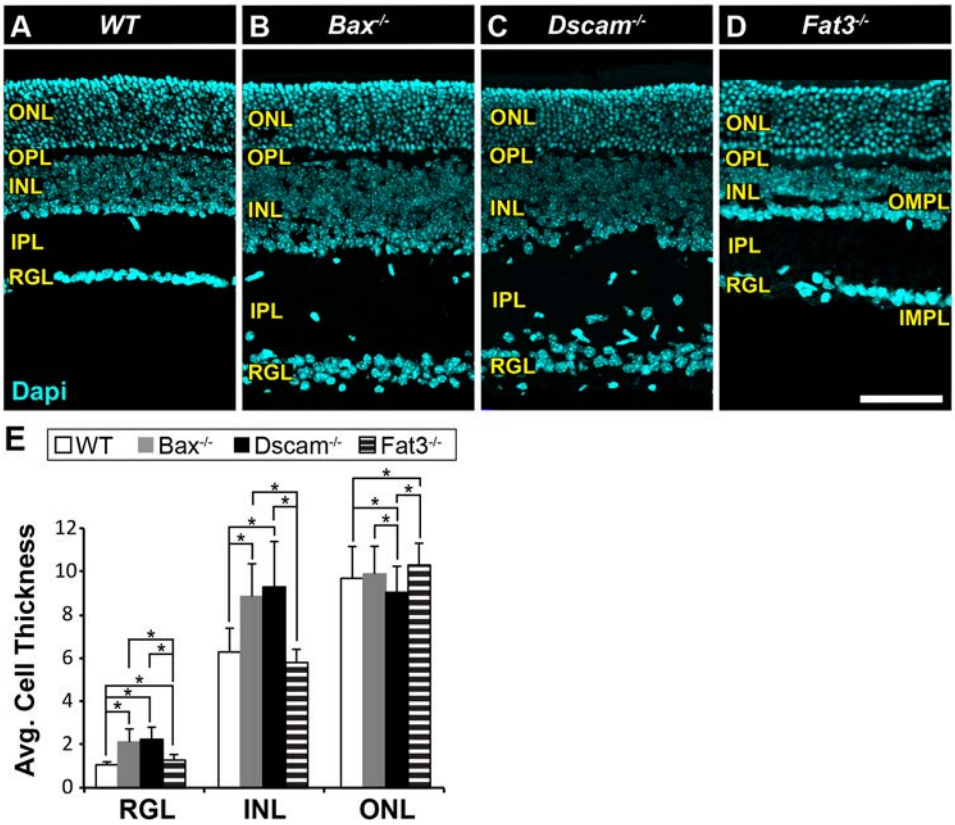

Figure 2.2. Mutant mouse strains used in this study. A-D) P28 retina sections stained with DAPI. **A)** *WT* retina. The stereotypic organization of the retina consists of 3 cellular laminae: ONL, INL and RGL, separated by 2 plexiform layers: OPL and IPL. **B)** *Bax*$^{-/-}$ retina. Increase thickness in the INL, IPL and RGL due to a defect in developmental cell death. Lamination of the neural retina is maintained, except ectopic neural somas located in IPL. **C)** *Dscam*$^{-/-}$ retina. Increase thickness in the INL, IPL and RGL due to a defect in developmental cell death. Lamination of the outer retina is maintained while the inner retina (INL, IPL and RGL) is highly disrupted. **D)** *Fat3*$^{-/-}$ retina. Cellularity is maintained. Abnormal migration of neurons results in more cells found within the RGL and less in the INL. Two ectopic plexiform layers form. One in the INL and the other below the RGL, termed the outer and inner misplaced plexiform layer (OMPL and IMPL), respectively. **E)** Cell thickness of each nuclear layer quantified. n≥3 mice was used for each strain. Error bars = SD. A one-way ANOVA was used to statistically analyze data for each cellular layer separately (RGL: $p \leq 6.61 \times 10^{-52}$; INL: $p \leq 1.45 \times 10^{-44}$; ONL: $p \leq 7.31 \times 10^{-5}$). Tukey's pairwise comparison was used to compare each group. *denotes statistical differences between groups. Abbreviations: INL: inner nuclear layer, IMPL: inner misplaced plexiform layer, IPL: inner plexiform layer, ONL: outer nuclear layer, OMPL: outer misplaced plexiform layer, OPL: outer plexiform layer, RGL: retinal ganglion cell layer. Scale bar in D = 100 µm.

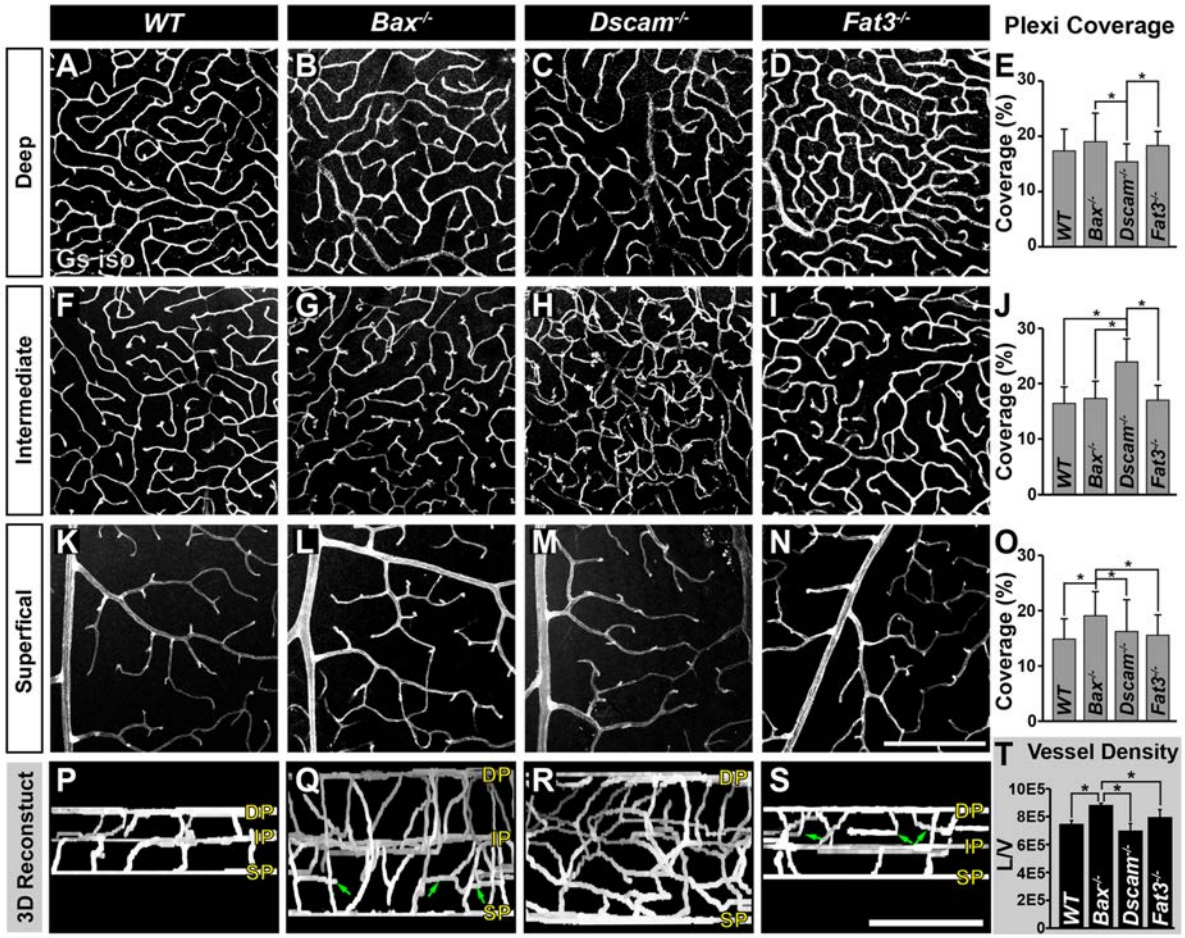

Figure 2.3. Analysis of neural organization and density on formation of vascular plexi. P28 whole retinas stained with GS isolectin. **A-E)** Analysis of the DP. A significant decrease in vascular coverage was detected in *Dscam*$^{-/-}$ retinas, compared to *Bax*$^{-/-}$ and *Fat3*$^{-/-}$. **F-J)** Analysis of the IP. *Dscam*$^{-/-}$ retinas lack a defined IP, data is representative of all vessels between the SP and DP. **K-O)** Analysis of the SP. A significant increase in vascular coverage was detected in *Bax*$^{-/-}$ retinas. **P-S)** Digital reconstruction of vessel image in whole mount flipped to view the x/z-axis. Ectopic vessels are found throughout the IPL of *Bax*$^{-/-}$ and the INL of *Fat3*$^{-/-}$ retinas (green arrows). **T)** Graph representing total vessel density. n≥3 mice was used for each strain per quantification. Error bars = SD. A one-way ANOVA was used to statistically analyze all data separately (DP coverage: $p \leq 6.94 \times 10^{-18}$; IP coverage: p=0.00; SP coverage: $p \leq 2.80 \times 10^{-5}$; vessel density: $p \leq 1.95 \times 10^{-3}$). Tukey's pairwise comparison was used to compare each group. *denotes statistical differences between groups. Abbreviations: DP: deep plexus, GS iso: GS isolectin, IP: intermediate plexus, SP: superficial plexus. Scale bar in N = 200 μm; S = 100 μm.

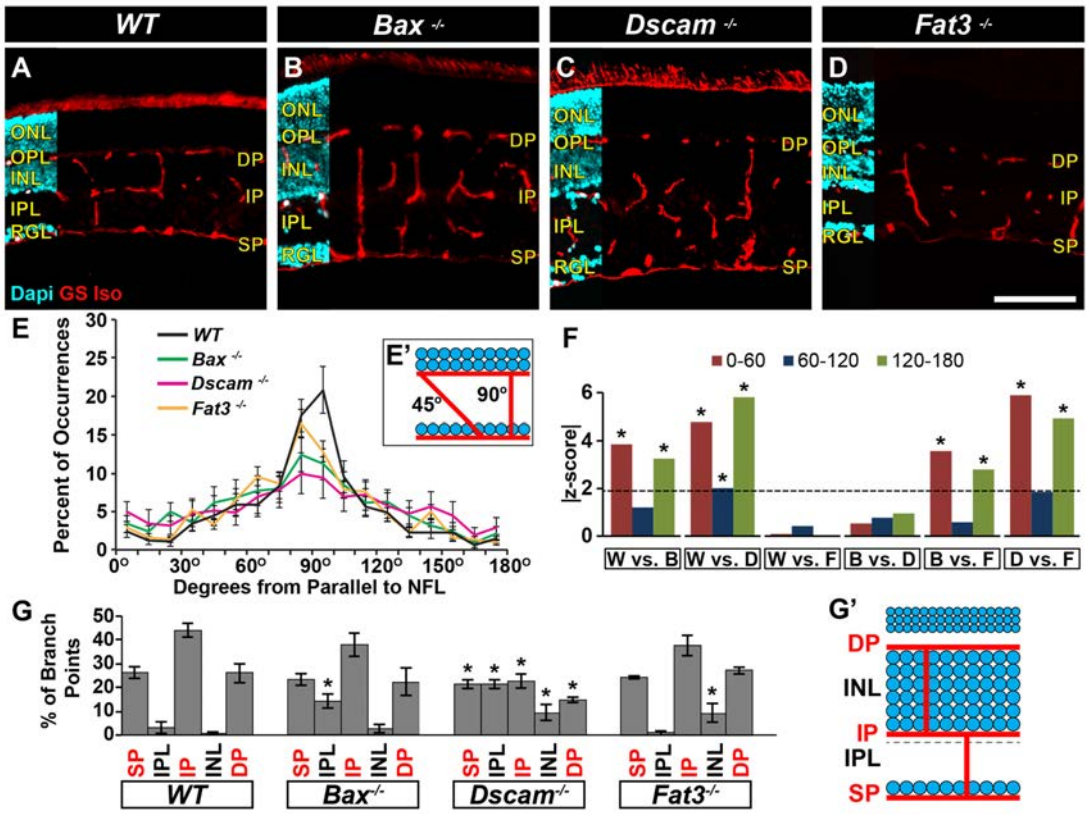

Figure 2.4. Analysis of neural organization and density on interplexus connections. **A-D)** P28 retina sections stained with GS isolectin and DAPI. **E)** The trajectory of vessels was quantified throughout the IPL. The majority of vessels in *WT* and *Fat3*$^{-/-}$ ran perpendicular to the NFL. *Bax*$^{-/-}$ vessels mainly ran perpendicular to the NFL with some ectopic vessels running parallel. *Dscam*$^{-/-}$ vessels were much more tortuous. Error bars = SD. **F)** Mann-Whitney U tests were used to statistically analyze orientation data. The data were grouped in increments of 30º. Graph represents the absolute z-score value generated by test. Dotted line represents the threshold a value must pass to be considered statistically different. *denotes that threshold was met. **G)** Branching locations were analyzed for interplexus vessels. Vessels within the *WT* branch at areas corresponding to vascular plexi. A significant increase in branch points (BPs) was observed in the IPL of *Bax*$^{-/-}$ and the INL of *Fat3*$^{-/-}$. BPs were uniformly distributed across *Dscam*$^{-/-}$ retinas. Error bars = SD. Student's *t*-test was used to statistically analyze *WT* vs other genotypes. Percent data was converted to arcsine for analysis. *p≤0.05. n≥3 mice was used for each strain per quantification. Abbreviations: B: *Bax*$^{-/-}$, D: *Dscam*$^{-/-}$, DP: deep plexus, F: *Fat3*$^{-/-}$, GS iso: GS isolectin, INL: inner nuclear layer, IP: intermediate plexus, IPL: inner plexiform layer, NFL: nerve fiber layer, ONL: outer nuclear layer, OPL: outer plexiform layer, RGL: retinal ganglion cell layer, SP: superficial plexus, W: *WT.* Scale bar in D = 100 µm.

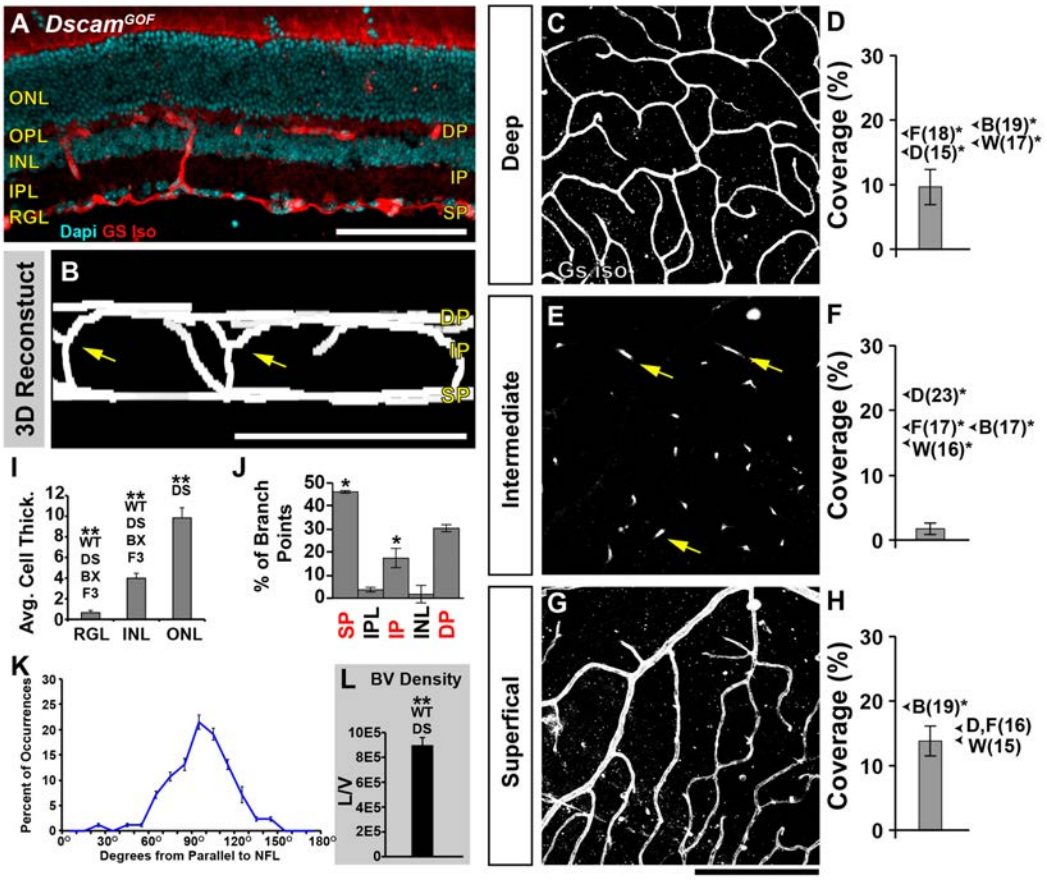

Figure 2.5. Analysis of retinal vasculature in the *Dscam*^{GOF} retina. Retinal vasculature was analyzed in retinas over expressing *Dscam*, *Dscam* gain-of-function (*Dscam*^{GOF}), retinas at P28. These retinas have significantly reduced number of neurons within the inner retina due to an increase in developmental cell death, while maintaining lamination within the inner retina. **A)** Cross section of retina stained with GS isolectin and DAPI. **B)** Digital reconstruction of vessel image in whole mount flipped to view the x/z-axis. Note the lacking IP (yellow arrows). **C-D)** Analysis of the DP. A significant decrease in coverage was detected compared to all other genotypes. Arrows show the average coverage of other genotypes for comparison and the average value is denoted within parentheses. *denotes statistical differences. **E-F)** Analysis of the IP. *Dscam*^{GOF} retinas lack an IP. Vessel branching was observed at the boundary of the INL and IPL (yellow arrows), yet these vessels never ramified to create an IP. **G-H)** Analysis of SP. A significant decrease in coverage was detected compared to the *Bax*$^{-/-}$ retina. **I)** Cellular thickness of each cellular layer. There were statistically fewer cells within the RGL and INL compared to all strains. There were statistically more cells within the ONL compared to *Dscam*$^{-/-}$. **J)** Analysis of

interplexus vessel branching. A statistical increase in the frequency of BPs within the RGL and a statistical decrease at the IP was observed when comparing to *WT*. **L)** Density of *Dscam*^{GOF} vessels. A significant increase in vessels was detected when compared to *WT* and *Dscam*$^{-/-}$ retinas. Error bars = SD. One-way ANOVAs were used to statistically compare *Dscam*^{GOF} to all other strains for cell thickness, plexi coverage, and vessel density (p-values are included in other figures). Tukey's pairwise comparison was used to compare each group. Student's *t*-test was used to statically compare BPs to *WT*. *p≤0.05. Mann Whitney U test was used to statistically compare *Dscam*^{GOF} vs all other strains. Abbreviations: B: *Bax*$^{-/-}$, BX: *Bax*$^{-/-}$, DP: Deep Plexus, DS: *Dscam*$^{-/-}$, *Dscam*^{GOF}: *Dscam gain-of-function*, F: *Fat3*$^{-/-}$, F3: *Fat3*$^{-/-}$, GS iso: GS isolectin, INL: inner nuclear layer, IP: Intermediate Plexus, IPL: inner plexiform layer, NFL: nerve fiber layer, ONL: outer nuclear layer, OPL: outer plexiform layer, RGL: retinal ganglion cell layer, SP: Superficial plexus, W: *WT*, WT: *WT*. Scale bar in A and B = 100 μm; in G = 200 μm.

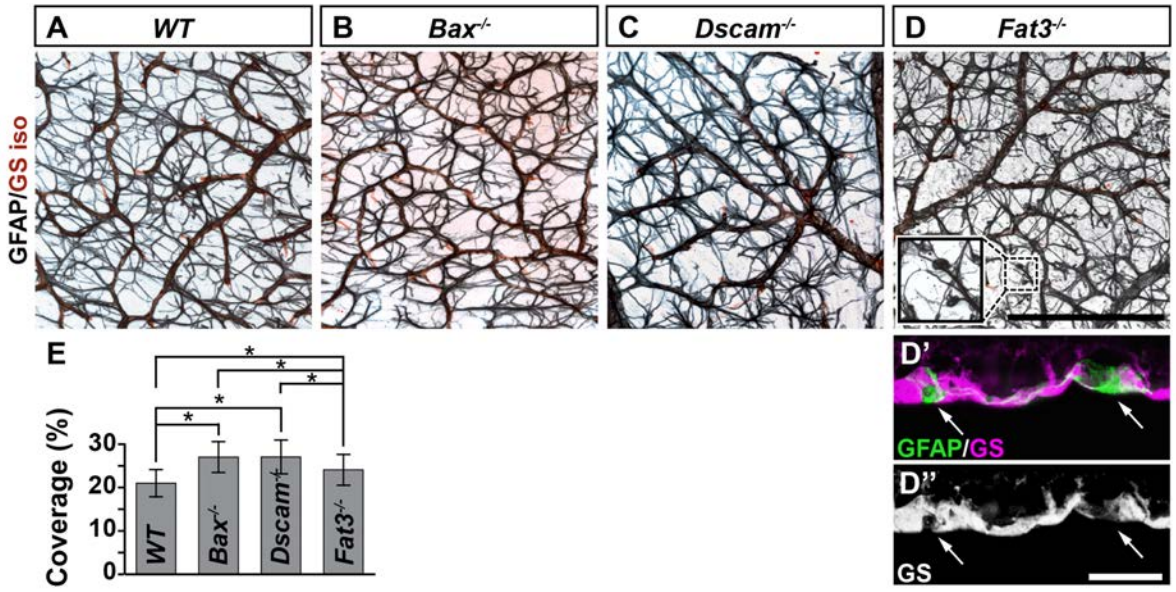

Figure 2.6. Astrocytes in mutant strains. A-D) P28 whole retinas stained with GFAP and GS isolectin. The characteristic star-shaped morphology of astrocytes was present in all of the models and their processes wrapped blood vessels. Within *Fat3*$^{-/-}$ retinas, globe shaped processes were found at some tips of astrocytes and filled areas of the inner limiting membrane that were discontinuous (arrows in D' and D''). **E)** Graph illustrating the coverage of GFAP within whole retinas. A significant increase in coverage was detected when comparing all of the strains to *WT*. A significant decrease in coverage was detected when comparing *Fat3*$^{-/-}$ to *Bax*$^{-/-}$ or *Dscam*$^{-/-}$ mice. n≥3 mice was used for each strain. Error bars = SD. A one-way ANOVA was used to statistically analyze the data ($p \leq 2.69 \times 10^{-13}$). Tukey's pairwise comparison was used to compare between groups. *denotes statistical differences. Abbreviations: GFAP: glial fibrillary acidic protein, GS: glutamine synthetase, GS iso: GS isolectin. Scale bar in D = 200 µm; D'' = 20 µm. Inset in D = 44x44 µm.

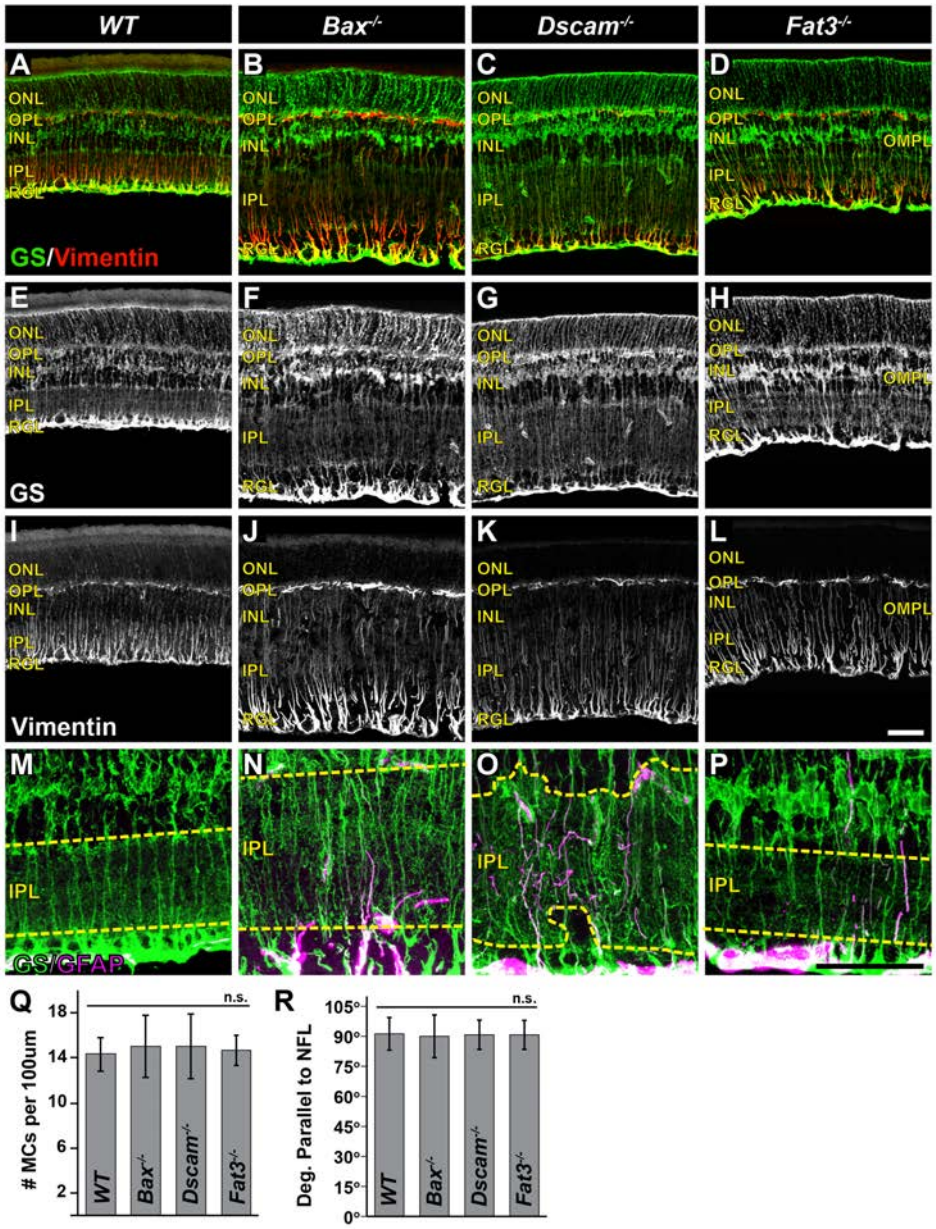

Figure 2.7. Müller cells in mutant strains. A-L) P28 retina sections stained with GS and vimentin. **M-P)** High magnification images of GS and GFAP staining within the IPL. Yellow dashed line outlines the boundary of the IPL. **Q)** Graph illustrating MC density. No significant difference in cell number was detected. **R)** Graph illustrating measurement of MC radial process projections. n≥3 mice was used for each strain per quantification. Error bars = SD. A one-way ANOVA was used to statistically analyze the data separately (MC density: p=0.88; MC radial process: p=0.27). Abbreviations: GFAP: glial fibrillary acidic protein, GS: glutamine synthetase, INL: inner nuclear layer, IPL: inner plexiform layer, MC: Müller cell, NFL: nerve fiber layer, ONL: outer nuclear layer, OMPL: outer misplaced plexiform layer, OPL: outer plexiform layer, RGL: retinal ganglion cell layer. Scale bar in L and P = 50 µm.

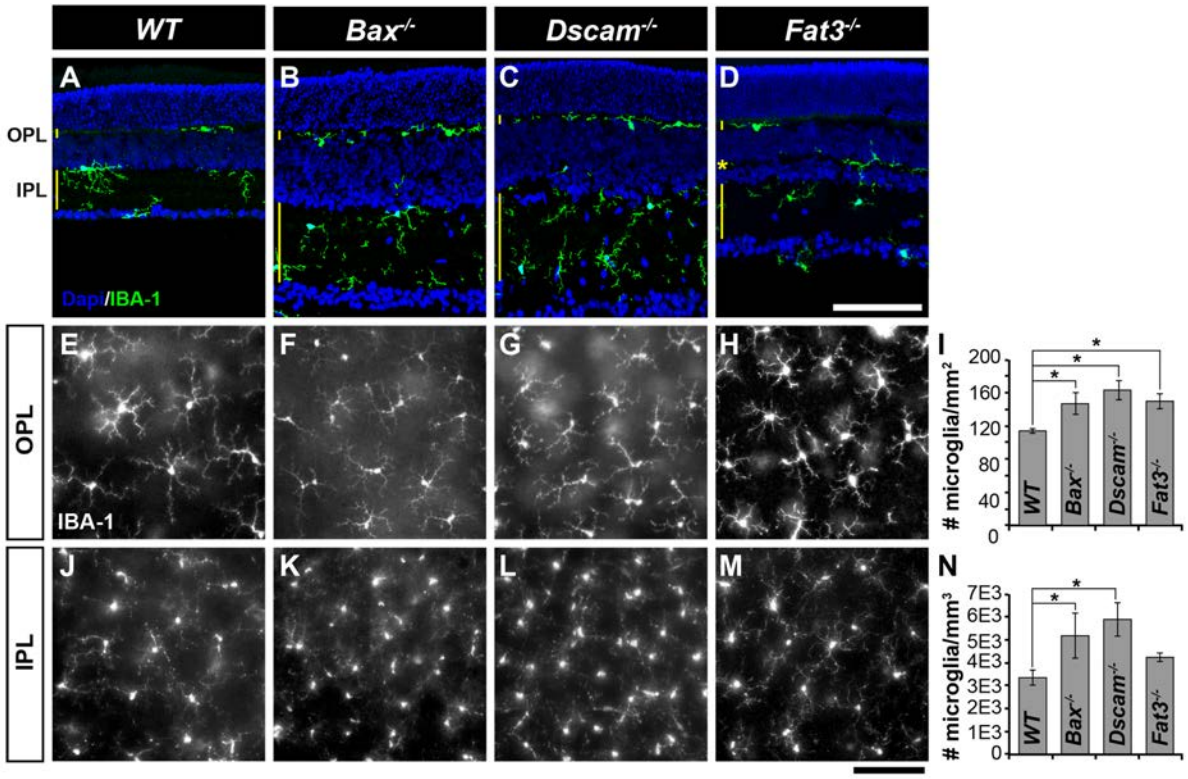

Figure 2.8. Microglia in mutant strains. A-D) P28 retina sections stained with IBA-1 and DAPI. Microglia can were found within neurite containing laminae of retina: the OPL, IPL and the OMPL of *Fat3*$^{-/-}$ mice. **E-H)** Microglia within the OPL in whole retinas. **I)** Graph illustrating density of microglia within the OPL. **J-M)** Microglia within the IPL in whole retinas. **N)** Graph illustrating density of microglia within the IPL. Within the OPL, a significant increase in microglia was observed in all models, when compared to *WT*. Within the IPL, a significant increase in microglia was observed in *Bax*$^{-/-}$ and *Dscam*$^{-/-}$ when compared to *WT*. n≥3 mice was used for each strain per quantification. Error bars = SD. A one-way ANOVA was used to statistically analyze the data (OPL: $p \leq 1.80 \times 10^{-3}$; IPL $p \leq 6.02 \times 10^{-3}$). Tukey's pairwise comparison was used to compare between groups. *denotes statistical differences. Abbreviations: IPL: inner plexiform layer, OPL: outer plexiform layer. Scale bar in D and M = 100 µm.

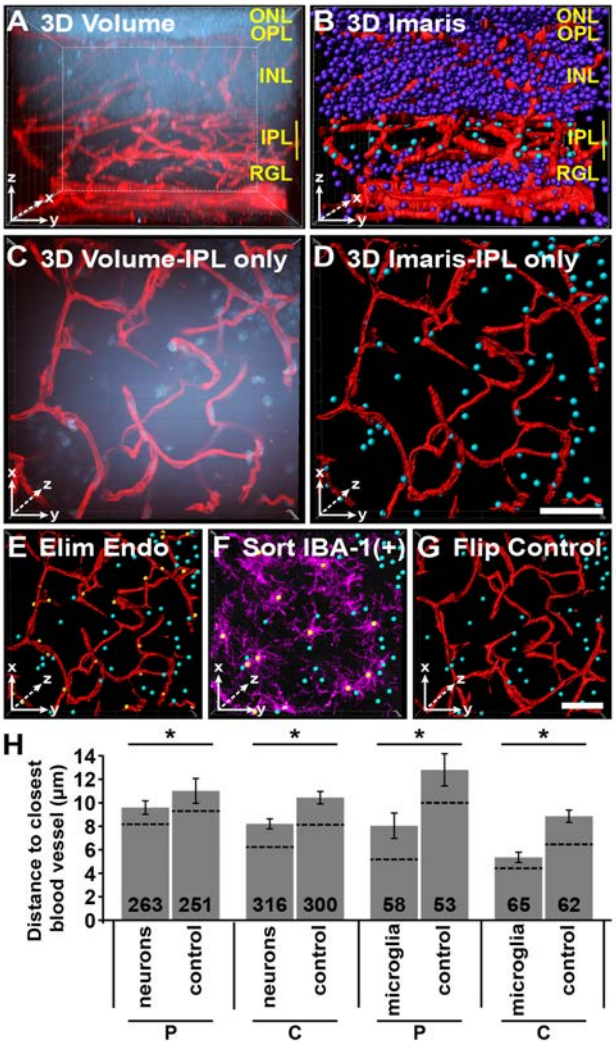

Figure 2.9. Nuclei to nearest vessel 3D assay. Using Bitplane's Imaris, we developed a 3D assay to measure the neural soma and microglia to the nearest vessel. This was performed on *Dscam*$^{-/-}$ retinas at P14 due to the large number of displace neurons within the IPL **A)** 3D rendering of image of whole retina stained with DRAQ5 and GS isolectin. **B)** Blood vessels were made into surfaces (red) while nuclei were made into spots (purple and cyan). Spots within the IPL are selected and colored cyan, while all other nuclei are purple. **C)** Cropped view of IPL 3D rendering. Flipped to view the x/y-axis. **D)** Cropped view of IPL of Imaris objects. Note that some nuclei in C are not present in D. This is because they are part of the INL not the IPL and were excluded from analysis. **E)** Endothelial nuclei were sorted by vessel reconstruction and GS isolectin staining and eliminated from analysis. **F)** Microglia were sorted by IBA-1 staining (purple). **G)** Vessels were flipped along the horizontal axis and served as an internal control. This control randomized the distribution of

nuclei allowing for the comparison between the relative placement of cells to blood vessels to that of random distribution **H)** Graph illustrating the average distance between neurons and vessels or microglia and vessels. Number in bar is the total number of spots quantified. Dotted line represents the median. Images were captured from 6 different retinas. Error bars = SE. Student's *t*-test was used to analyze data. *p≤0.05. Abbreviations: INL: inner nuclear layer, IPL: inner plexiform layer, ONL: outer nuclear layer, OPL: outer plexiform layer, RGL: retinal ganglion cell layer. Scale bars in D and G = 25 μm.

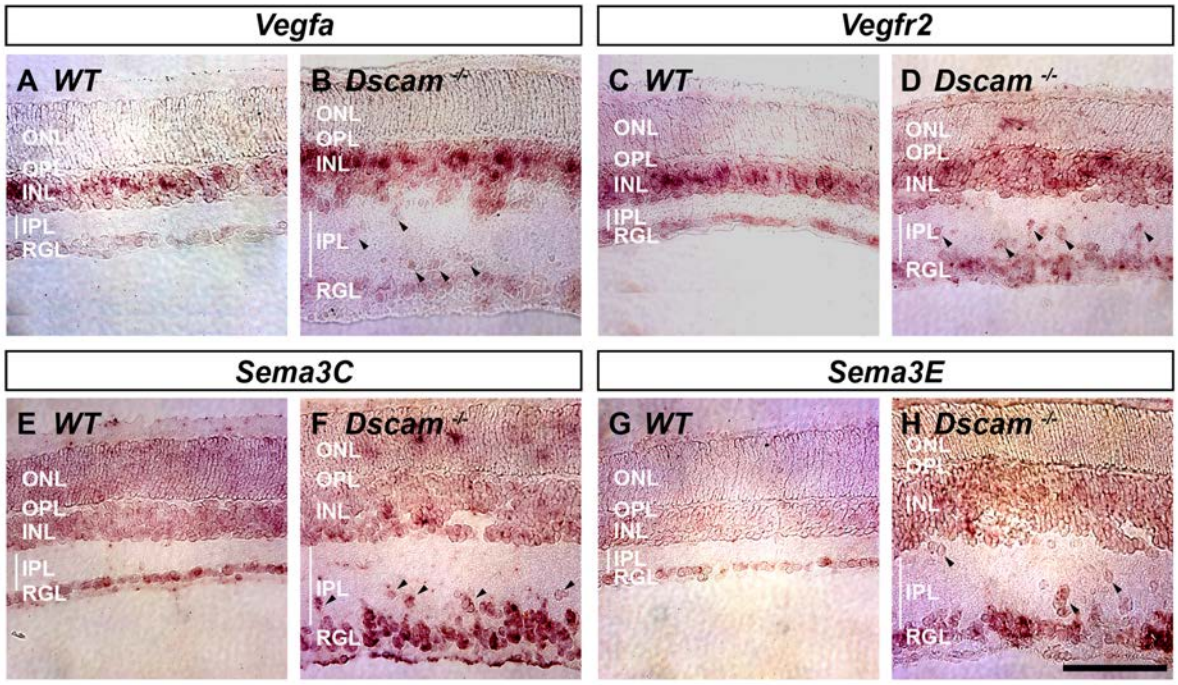

Figure 2.10. Neuron placement affects the expression patterns of angiogenic factors. Retinas were prepared for *in-situ* hybridization at P14 comparing *Dscam*$^{-/-}$ to littermate controls. **A-B)** *Vegfa* expression was detected strongly within the central INL of *WT* and *Dscam*$^{-/-}$ retinas and to a lesser extent within most cells of the INL and RGL. *Vegfa* was also detected within displaced neurons in *Dscam*$^{-/-}$ retinas (arrowheads). **C-D)** *Vegfr2* expression was detected strongly within the central INL of *WT* retinas and to a lesser extent in cells throughout the INL and RGL. *Vegfr2* expression was detected within the INL and RGL of *Dscam*$^{-/-}$ retinas although the central expression in the INL was less distinct. *Vegfr2* expression was also detected in patches in the ONL and within displaced neurons of *Dscam*$^{-/-}$ retinas (arrowheads) **E-F)** *Sema3C* expression was detected throughout all cellular layers in *WT* and *Dscam*$^{-/-}$ retinas, including displaced neurons in *Dscam*$^{-/-}$ retinas (arrowheads) **G-H)** *Sema3E* expression was detected within the RGL and to a lesser extent in the INL of *WT* and *Dscam*$^{-/-}$ retinas, and within displaced neurons of *Dscam*$^{-/-}$ retinas (arrowheads). n=4 retinas from two mice were analyzed. Abbreviations: INL: inner nuclear layer, IPL: inner plexiform layer, ONL: outer nuclear layer, OPL: outer plexiform layer, RGL: retinal ganglion cell layer. Scale bar in H = 100 μm.

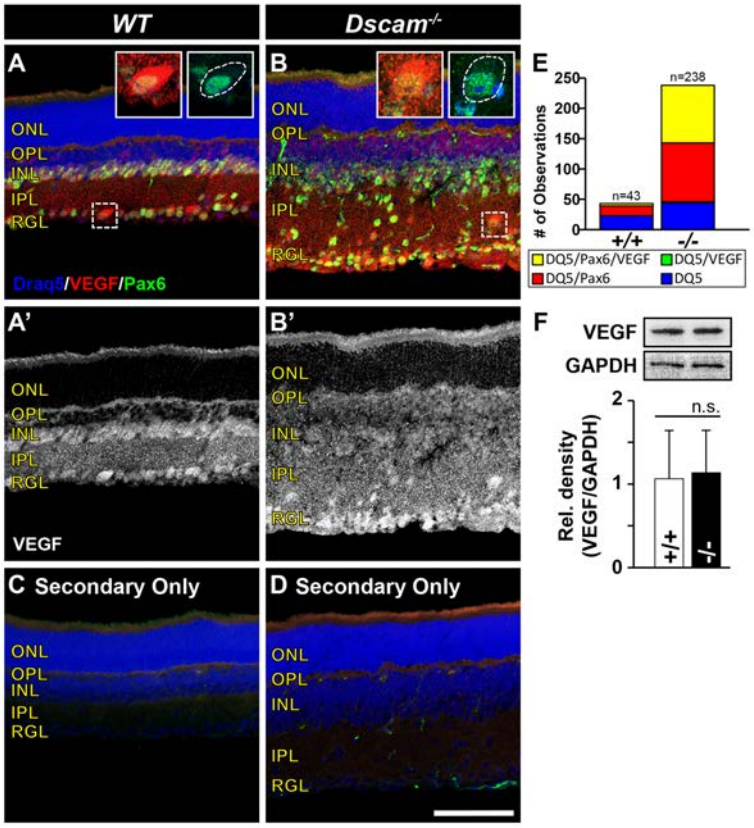

Figure 2.11. VEGF localization is influenced by neural placement. Retinas were prepared for immunohistochemistry at P14 comparing *Dscam*$^{-/-}$ to littermate controls. **A-B)** Retina sections stained with DRAQ5, VEGF and PAX6. Insets illustrate the accumulation of VEGF on the surface of neurons. White dotted line in the second inset shows the outline of neuron soma. **A'-B')** VEGF channel split out for better visualization. **C-D)** Control retinas stained with secondary antibodies only. Staining of VEGF and PAX6 is absent. α-Mouse staining can be seen in blood vessels. **E)** Graph illustrating the raw cell counts of nuclei within the IPL of *WT* and *Dscam*$^{-/-}$ retinas. Nuclei were sorted into 4 bins (Yellow = DRAQ5/PAX6/VEGF; Green = DRAQ5/VEGF; Red = DRAQ5/PAX6; Blue = DRAQ5). All cells VEGF+ were PAX6+, but not all PAX6+ cells were VEGF+. **F)** Western blot was performed to quantify the total amount of VEGF protein in *Dscam*$^{-/-}$ retinas compared to littermate controls. No significant difference was detected when comparing the relative density (VEGF/GAPDH) of VEGF protein in *Dscam*$^{-/-}$ and *WT* littermate controls. Error bars = SD. Student's *t*-test was used to analyze data (p=0.83). n≥3 mice was used for each strain per quantification. Abbreviations: DQ5: DRAQ5, GAPDH: Glyceraldehyde-3-Phosphate Dehydrogenase, INL: inner nuclear layer, IPL: inner plexiform layer, ONL: outer nuclear layer, OPL: outer plexiform layer, RGL: retinal ganglion cell layer, VEGF: vascular endothelial growth factor. Scale bar in D = 100 μm. Insets in A and B = 31x31 μm.

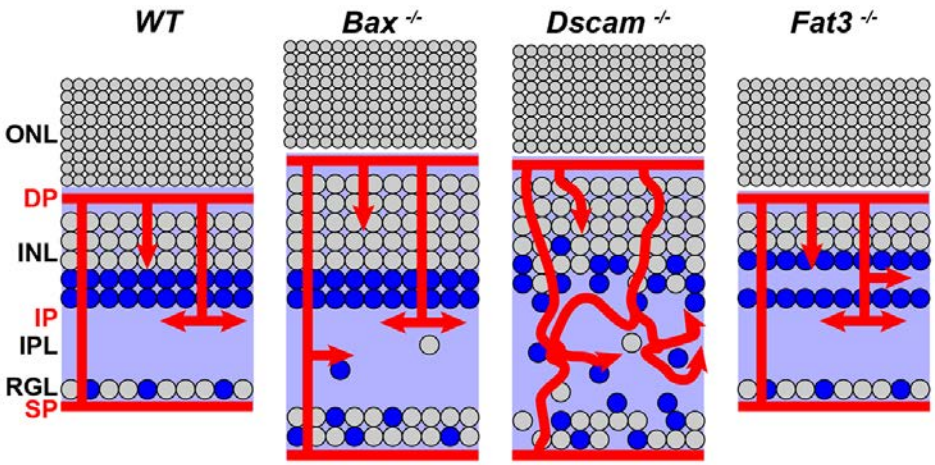

Figure 2.12. Working Model. Disrupting the organization of the neurons in the inner retina in turn change how neural derived factors are presented altering the organization of non-neural components. Illustrated here is VEGF distribution to serve as an example. There are likely many neural derived angiogenic factors influenced by neuron placement. Abbreviations: DP: deep plexus, INL: inner nuclear layer, IP: intermediate plexus, IPL: inner plexiform layer, ONL: outer nuclear layer, OPL: outer plexiform layer, RGL: retinal ganglion cell layer, SP: superficial plexus.

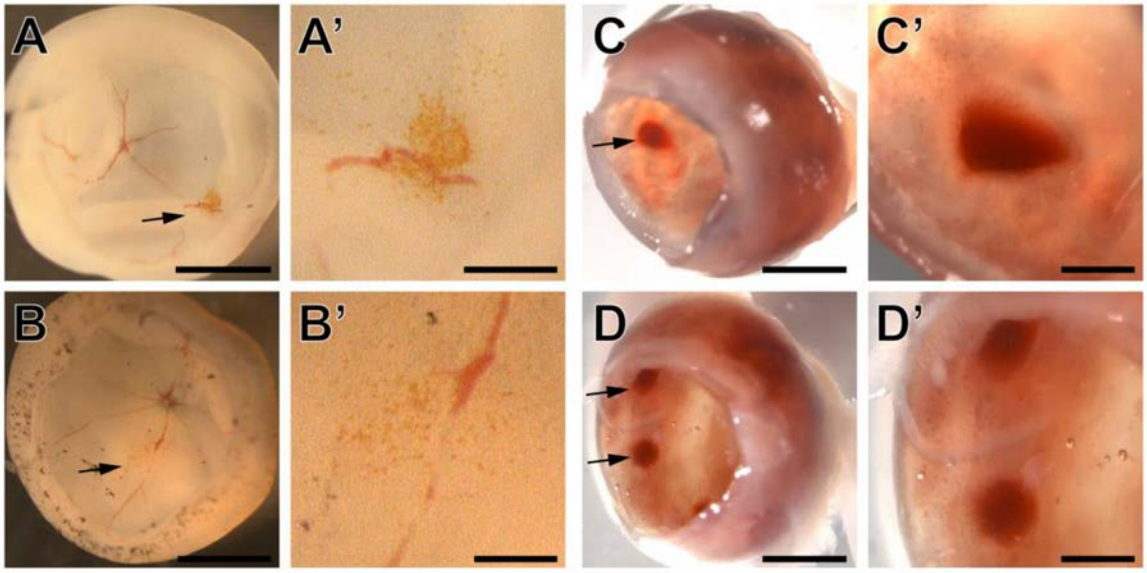

Supplemental Figure 2.1. Retinal bleeding when Dscam is conditionally targeted within retinal neurons. Retinal bleeding was observed in retinas where Dscam was conditionally deleted from retinal neurons using Pax6α-Cre. This bleeding was from none (not shown), to little (A-B) to severe (C-D). Arrows point to locations of bleeding within the retinas. Scale bars in A, B, C and D = 1mm; in A', B', C' and D' = 200 μm.

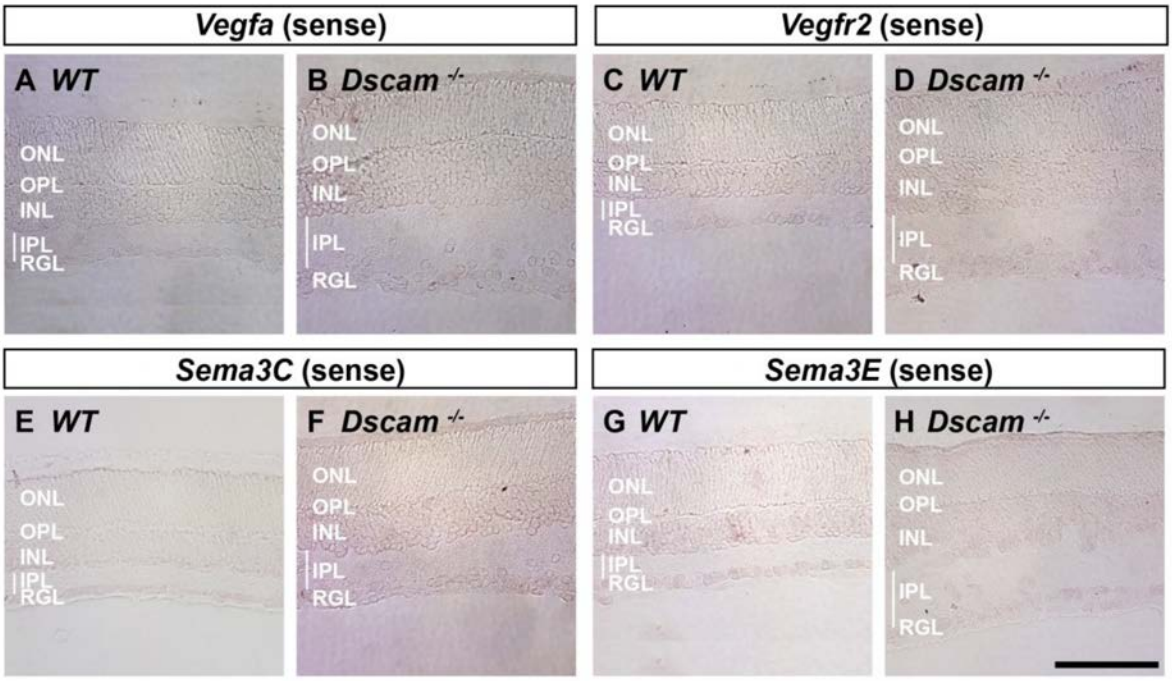

Supplemental Figure 2.2. Sense controls for in-situ hybridization. Sense probes were made for each of the antisense probes, as controls. No color reaction was detected in any of the controls. A-B) Vegfa (sense). C-D) Vegfr2 (sense). E-F) Sema3C (sense). G-H) Sema3E (sense). n=4 retinas from 2 mice were analyzed. Abbreviations: INL: inner nuclear layer, IPL: inner plexiform layer, ONL: outer nuclear layer, OPL: outer plexiform layer, RGL: retinal ganglion cell layer. Scale bar in H = 100 μm.

Chapter 3: Analysis of retinal vascular plexi and interplexus connections in mouse models

Aaron B. Simmons and Peter G. Fuerst
Current Status: Submitted to *Methods in Molecular Biology*

ABSTRACT

The retina is a highly organized neural tissue consisting of three neural layers and two synaptic layers. Blood vessels that nourish the mouse and human neural retina mirror this organization consisting of three plexus layers, or plexi, that run parallel within the retina, connected by interplexus vessels to create a closed vascular network. Here, we describe a methodology to describe this organization that can be used to interrogate factors mediating retinal vessel patterning including: coverage of the vascular plexi, branching and orientation of the inter-plexus connections, and digital reconstruction of the retinal vasculature to measure vessel length and density. The methodology focuses on the mouse retina, but can easily be adapted to study retinal vessels of other species.

1 INTRODUCTION

The retina is a highly ordered neural tissue responsible for detection and processing of visual stimuli, followed by the propagation of this information to visual centers of the brain***(1)***. The retina is organized into alternating cellular and synaptic layers that permit its function: the retinal ganglion cell layer (RGL), inner plexiform layer (IPL), inner nuclear layer (INL), outer plexiform layer (OPL), and the outer nuclear layer (ONL) (Figure 3.1). The human retina is nourished by the retinal vasculature, which mirrors the organization of the neural retina and consists of three vascular plexi that run parallel within the retina, the superficial plexus (SP) found on the surface of the retina, the intermediate plexus (IP) found in the IPL adjacent to the INL, and the deep plexus (DP) found within the OPL (Figure 3.1)***(2)***.

The mouse retina serves as an excellent model system for understanding factors mediating vessel patterning in the human retina because of their similar organization, which is not conserved in all mammals***(2)***. Development of the retinal vasculature occurs in

response to numerous cellular and molecular interactions between the vasculature and neurons***(3-8)***, Müller cells***(8-10)*** astrocytes***(11-13)*** and microglia***(14)***. These cues orchestrate the development of vessels in an overlapping stepwise process beginning with the radial proliferation and expansion of the SP on the surface of the retina, followed by vascular sprouting into the retina to form the DP, and finally vascular sprouting back towards the surface of the retina to form the IP***(2)***.

Abnormal vessel patterning can result in degeneration of the neural retina and eventually the loss of vision***(15-17)***. Designing and interpreting experiments aimed to identify factors necessary for vessel patterning in the retina therefore require a methodology for measuring morphological characteristics of the retinal vasculature. Here, we describe means to quantify vessel patterning of the three vascular plexi and the vessels connecting them, the interplexus vessels. These quantifications can then be used to compare experimental groups testing candidate factors mediating retinal vessel patterning.

2 MATERIALS

This section is intended to provide the reader with a list of materials, reagents, and solutions needed to complete the protocols described, however, each protocol section only require certain reagents. Common laboratory materials such as pipettors are not included in this list. All materials are listed, and then each methods section begins with a "*Required Materials"* list that includes everything needed to perform the specific protocol.

2.1 Reagents, Materials, and Software

Cryo-molds: 10x10x5mm (4565, Tissue-Tek); 15x15 mm (4566 Tissue-Tek).

DAPI (4',6-diamidino-2-phenylindole): 4083, Cell Signaling Technology.

DRAQ5: 62251, Thermo Scientific.

Hydrophobic pen: Z377821, SIGMA

Isolectin GS-B4 (GS-B4): Alexa Fluor 488 Conjugate (I21411, Invitrogen), Alexa Fluor 568 Conjugate (I21412, Invitrogen), Alexa Fluor 594 Conjugate (I21413, Invitrogen), Alexa Fluor 647 Conjugate (I32450, Invitrogen).

FIJI: software can be downloaded here: https://imagej.net/Fiji/Downloads. FIJI runs on both Mac and PC computers. In order to carry out the protocols outlined here, you need to have the following plugins: 1) Bio-Formats***(18)***, a plugin designed to read most common microscope software image formats and 2) Simple Neurite Tracer***(19)***, which is used for reconstructing vessels and measuring their length.

Glycerol (FW 92.09): G33-500, Fisher Scientific.

Optimal cutting temperature (OCT) compound: 4583, Tissue-Tek.

Paraformaldehyde (16% solution): 15710, Electron Microscopy Sciences.

Sucrose (FW 342.30): 8550, EMD Millipore.

2.2 Stock solutions

10% Triton Solution: For 40 ml, add the following to a 50 ml conical tube: 4 ml Triton X-100 (T9284, Sigma-Aldrich), and fill to 40 ml with dH_2O. Wrap stored in aluminum foil to protect from light.

Phosphate-buffered Saline Stock Solution (10X PBS): Note: Do not use this stock solution for the methods sections, use to make the 1X working solutions. For 1 L 10X PBS, add the following to 750 ml dH_2O. 80 g NaCl (FW 58.440), 2.0 g KCl (FW 74.55), 26.8 g $Na_2HPO_4 \cdot 7H_2O$ (FW 268.07), 2.4 g KH_2PO_4 (FW 136.09). Adjust pH to 7.4. Adjust volume to 1 L with dH_2O.

Sodium Azide Stock Solution (100X Sodium Azide): For 10 ml, dissolve 2 g NaN_3 (FW 65.01) in dH_2O into a total volume of 10 ml.

2.3 Working solutions

0.1% Triton Buffer (TB): For 40 ml, add the following to a 50 ml conical tube: 4 ml 10X PBS, 400 µl 10% Triton solution, 400 µl of 2% 100x Sodium Azide, and fill to 40 ml with dH_2O.

0.4% Triton Buffer (TB): For 40 ml, add the following to a 50 ml centrifuge tube: 4 ml 10X PBS, 1.6 ml 10% Triton solution, 400 µl of 2% 100x Sodium Azide, and fill to 40 ml with dH_2O.

4% Paraformaldehyde (PFA): For 40 ml, add the following to a 50 ml centrifuge tube: 10 ml 16% PFA, 4 ml 10X PBS, and fill to 40 ml with dH_2O.

30% Sucrose solution: For 40 ml, first dissolve 12g of sucrose in 30 ml 1X PBS. Once dissolved, adjust the final volume to 40 ml with 1X PBS.

Cutting media: Mix OCT Compound and 30% Sucrose Solution at a 2:1 ratio (OCT Compound:30% Sucrose Solution).

Mounting media: For 40 ml, add the following to a 50 ml centrifuge tube: 32 ml glycerol, 7.6 ml 1X PBS, and 400 µl 100X Sodium Azide.

Phosphate-buffered Saline Working Solution (1X PBS): Use this solution for the methods section. For 1 L, dilute 100 ml of 10X PBS with 900 ml of dH_2O.

3 METHODS

3.1 Retina Extraction and Fixation

Required Materials: mice, euthanizing agent (approved by animal protocols at your institution), PBS, petri dish, forceps, dissecting scope, 26-gauge needle, microdissection scissors, 1.5 ml microcentrifuge tubes, 4% PFA

1. Euthanize mouse with protocols approved by your Animal Care and Use Committee (ACUC) at your institution.
2. Enucleating (Figure 3.2 A): Start by applying pressure to the skull dorsally and ventrally from the eye, until the eye begins to bulge out slightly. Using forceps, grasp

the optic nerve at the back of the eye by wedging them between the eyeball and eye socket and remove gently the eye.

3. Hemisecting (Figure 3.2 B): The following steps should be performed under a dissecting scope in a petri dish filled with PBS. Begin by stabilizing the eye by grasping the optic nerve or ocular muscles with forceps. Next, create a pilot hole with a 26-gauge needle at the cornea/sclera boundary and cut along the cornea/sclera boundary with microdissection scissors to remove the cornea and iris (*see* **Note 1**). Finally, remove the lens using forceps.
4. Fixing: Place the hemisected eyes into a 1.5 ml microcentrifuge tube filled 4% PFA solution. Incubate for 30 minutes (min) at room temperature (RT).
5. Fine dissecting: Immediately following fixation, place hemisected eyes in a petri dish filled with PBS and isolate the retina by removing the optic nerve and sclera. To remove the optic nerve, cut the optic nerve at the base near the sclera. To remove the sclera, use forceps to tease apart the sclera from the retina and peel it off. This is difficult to accomplish at some ages (approximately postnatal day 8-12) in mouse because the retina is firmly attached to the retina pigment epithelium.
6. Washing: Perform 2 x 20 min washes in 1.5 ml microcentrifuge tubes filled with PBS at RT.

3.2 Cryo-sectioning

Cryo-sectioning the tissue is only necessary for analysis of the interplexus vessels. To prepare tissue for as a whole-mount, for analysis of the vascular plexi, skip this section and proceed to staining and mounting (3.3.1).

Required Materials: retinas from section 3.1, 30% sucrose solution, 1.5 ml microcentrifuge tubes, cutting media, cryo-mold, liquid nitrogen, cryo-stat, positively charged glass microscope slides, slide box

1. Cryo-preserving the retina: Equilibrate the retina with the 30% sucrose solution by incubating the fine dissected retinas in a 1.5 ml microcentrifuge tube filled with the 30% sucrose solution. The retina will initially float at the surface of the solution, once equilibrated; the retina will sink to the bottom, usually within an hour at RT. This can be carried out overnight at 4 ºC.

2. Incubating the cryo-preserved retina in cutting media: Place retinas in a 1.5 ml microcentrifuge tube filled with cutting media and gently mix periodically to ensure the cutting media encompasses the retina without interference from the 30% sucrose.
3. Preparing the cryo-block: Place the retina in a cryo-mold filled with the cutting media and orient the retina so that the cutting plane is aligned with the posterior-anterior axis. Remove any bubbles within this media as it will cause problems when sectioning.
4. Freezing the cryo-block: Rapidly freeze by holding the cryo-mold just in the liquid phase of liquid nitrogen until the block is frozen solid. Suboptimal freezing will result in artifact or difficult cutting. This most often occurs because the tissue is frozen too slowly (held just above the liquid nitrogen) or frozen too rapidly (immersed too deeply into the liquid nitrogen). This usually takes about one minute. Blocks can be wrapped in foil and a sealed bag and stored at -20 to -80 ºC.
5. Sectioning the retina: Using a cryo-stat, section the cryo-block at a thickness between 10-16 µm. Tissue cuts best at approximately -20 ºC, but this temperature can be cryostat specific. Begin collecting the tissue around the optic nerve to ensure that the sections are perpendicular to the retina (*see* **Note 2**). Place the sections onto positively charged glass microscope slides and store in a slide box in the freezer. Slides are stable for greater than 1 year after collected onto slides.

3.3 Staining and Mounting

This section is divided into protocols specific for staining whole-mounted retinas and cryo-sections. Note that the procedures follow the same basic steps, however, incubations times and solutions used throughout the protocol are specific for each retina preparation. These protocols are compatible with anti-body staining (*see* **Note 3**).

3.3.1 Whole-mounted retina (Staining and Mounting)

Perform all incubation steps in 1.5 ml microcentrifuge tubes on a rocker table filled with 500 µl of each solution. All dilutions are made in 0.4% TB.

Required Materials: retinas from section 3.1, 1.5 ml microcentrifuge tubes, 0.4% TB, PBS, GS-B4, DAPI (optional), uncharged glass microscope slides, electrical tape, dissecting scope, microdissection scissors or scalpel, forceps, small paint brushes, Kim wipes, mounting media, coverslips.

1. Permeabilizing the retina: Incubate the retinas in 0.4% TB for 2-4 hours (hrs) RT or at 4°C for 12-18 hrs.
2. Staining retinal vasculature: Incubate the retinas in 1:200 dilution of GS-B4. Incubations can be performed at RT for 6-8 hours (hrs) or at 4°C for 12-36 hrs. DAPI can be added to the solution at a concentration of 1:5000 if desired (*see* **Note 4**) to stain nuclei.
3. Washing the retina: At RT, perform 2 x 20 min washes in PBS.
4. Preparing slide for mounting (Figure 3.3): Using uncharged glass microscope slides, cut a piece of electrical tape that covers a large portion of the microscope slide and cute a hole in the middle of the tape before applying it to the microscope slide (*see* **Note 5**). This helps to avoid compression of the retina, which can cause the orientation of vessels to distort.
5. Preparing the retina for mounting: Under a dissecting scope, place the retina cup side up (RGL facing up, ONL facing down) into the hole in the electrical tape. Make four equal slits into the retina to allow it to lay flat onto the slide. Gently remove excess PBS using a Kim wipe, but do not let the retina dry completely. Using paintbrushes, lay the retina down and gently brush off any remaining vitreous, hyaloid vasculature, and other material on the surface of the retina.
6. Mounting: Add a small amount of mounting media onto the tape, just outside the well. Apply a coverslip using forceps to first apply an edge to the mounting media and gently set the coverslip down over the retina. Use light pressure to adhere the coverslip, avoid using pressure directly on the retina. Place the prepared slide in a slide box lined with a paper towel to wick away excess mounting media. Retinas can be stored at 4°C for several weeks.

3.3.2 Cryo-sections (Staining and Mounting)

Perform all wash steps in a Coplin Jar and all incubation steps in a humidifier chamber to prevent the slides from drying out (*see* **Note 6**). All dilutions are made in 0.1% TB, to a

volume between 150-250 µl. Drawing a well around the retina sections with a hydrophobic pen will decrease the surface area needed to incubate the slides and decrease the reagent needed to cover the retinas.

Required Materials: prepared microscope slides with sections of retina from section 3.2, Coplin jar, humidifier chamber, PBS, 0.1% TB, GS-B4, DAPI, forceps, Kim wipes, mounting media, coverslips.

1. Washing the cutting media off slide: Wash slides in PBS for ≥5 min RT.
2. Permeabilizing the retina sections: Incubate slides in 0.1% TB for ≥30 min RT.
3. Staining retinal vasculature. Incubate slides in a 1:200 dilution of GS-B4. Incubations can be performed at RT for 1-3 hrs or at 4°C for 8-20 hrs.
4. Washing the retina sections: At RT, perform 3 x 10 min washes in PBS. Add DAPI to the 2nd wash a dilution of 1:50,000.
7. Mounting the retina sections with cover glass: Remove excess PBS from the slide by gently tapping the slide against a paper towel and wipe around the tissue with a Kim wipe. Add a small amount of mounting media to the slide and apply the coverslip with forceps. Place the prepared slide in a slide box lined with a paper towel to wick away excess mounting media and store in the fridge. Retina sections can be stored at 4°C for several weeks.

3.4 Image acquisition

Required Materials: prepared slides from section 3.3.1 or 3.3.2, microscope

The following is meant to serve as a guide, but should be tailored towards your experiments and imaging equipment. When imaging, the most important aspects are sampling (the location from which images are collected) and remaining consistent in this selection. In both preparations, the entirety of the retinal vasculature should be sampled and the z-steps should be uniform between compared groups. Recommended z-step sampling increment range is 0.5-1 µm. ***Whole-mounted retinas:*** retina should be sampled equally from all wings of the retina (dorsal, ventral, temporal, and nasal). Each wing of the retina should be sampled multiple regions (i.e. central, middle, periphery) (*see* **Note 7**). A good way to keep track of this is to reference distance from the optic nerve head for central images, distance from the edge of the retina for peripheral images, and shoot in the middle

for middle images. ***Cryo-sections:*** only retina sections sectioned perpendicular to the retina should be analyzed, as oblique cuts will skew the data (*see* **Note 2**). Image the entire retina section and generate a z-projection montage image to be analyzed.

3.5 Analysis of Vascular Plexi Coverage

Required Materials: images from section 3.4 *Whole-mounted retinas*, computer with FIJI software

1. Import image stacks into FIJI: This can be accomplished by simply dragging the file into the main FIJI window below the toolbar.
2. Preparing the image: To eliminate background, use the subtract background function (Process > Subtract Background...) and then adjust the brightness contrast (Image > Adjust > Brightness/Contrast…).
3. Creating z-projections (Figure 3.4 A-C): Scroll through the image stack and identify which image ranges contain each plexi (superficial, intermediate, and deep). Open the z-projection menu (Image > Stacks > Z Project...) and create z-projection images for each plexus by entering the appropriate image ranges and use “Max Intensity” projection type.
4. Creating binary image (Figure 3.4 D-F): Convert each z-projection into a binary image (Process > Binary > Make Binary). Make sure that the vessels are black, if not, simply repeat the “Make Binary” command and it will invert the image.
5. Measure plexi coverage: Open the Analyze Particles function (Analyze > Analyze Particles...). Check the “Summarize” box and click “OK”. A Summary Window of the measurements will appear summarizing the total area and the % area, among other measurements. Record the desired measurements. Values in the top right hand corner in Figure 3.4 D-F are % area for each image.

3.7 Analysis of Vascular Density

The following measurements are performed from images of whole-mounted retina using the FIJI plugin, Simple Neurite Tracer. Detailed directions and tips about using the software can be found here: https://imagej.net/Simple_Neurite_Tracer. This software can be used to

trace vessels in both 2D and 3D. Before beginning the protocols below, ensure that your scale of your images is set properly (*see* **Note 8**).

3.7.1 Vessel Density per Plexi

Required Materials: images from section 3.4 *Whole-mounted retinas*, computer with FIJI software

1. Open z-projection image of a plexus layer (Figure 3.5 A), generated in step 3 of "Analysis of Vascular Plexi Coverage".
2. Covert the image to an 8-bit (Image > Type > 8-bit).
3. Open Simple Neurite Tracer (Plugins > Segmentation > Simple Neurite Tracer).
4. Tracing the vasculature: Using Simple Neurite Tracer, trace the vessels. Figure 3.5 B shows a line-stack generated from tracing vessels in Figure 3.5 A. The fine capillaries in this image are not traced, but could be if that is desired. Again, remain consistent with whatever you choose.
5. Saving Data: After the vessels have been traced, save the traces file (File > Save traces file...). This is a file that you can use to reopen the trace you just created. Next, you can save the CSV file (File > Export as CSV). This is a file that provides a map of all the lines created. This file also contains the length of each line segment.
6. Calculating vascular density: In the CSV file, sum all of the lengths for each line segment. The number in the top left corner in Figure 3.5 B is the total length of vessels in micrometers. This number can now be normalized per unit area for which it was collected.

3.8.1 Total Vascular Density

Required Materials: images from section 3.4 *Whole-mounted retinas*, computer with FIJI software

1. Import image stacks into FIJI: This can be accomplished by simply dragging the file into the main FIJI window below the toolbar.

2. Preparing the image: To eliminate background, use the subtract background function (Process > Subtract Background...) and then adjust the brightness contrast (Image > Adjust > Brightness/Contrast...).
3. Covert the image to an 8-bit (Image > Type > 8-bit).
4. Open Simple Neurite Tracer (Plugins > Segmentation > Simple Neurite Tracer).
5. Tracing the vasculature: Using Simple Neurite Tracer, trace the vessels. The fine capillaries in this image are not traced, but could be if that is desired. Again, remain consistent with whatever you choose.
6. Saving Data: After the vessels have been traced, save the traces file (File > Save traces file...). This is a file that you can use to reopen the trace you just created. Next, you can save the CSV file (File > Export as CSV). This is a file that provides a map of all the lines created. This file also contains the length of each line segment.
7. Calculating vascular density: In the CSV file, sum all of the lengths for each line segment. The number in the top left corner in Figure 3.5 C is the total length of vessels in micrometers. This number can now be normalized per unit volume for which it was collected.
8. Generating a 3D projection (Figure 3.5 C): 3D images can be generated for the raw image and trace using the 3D viewer (Plugins > 3D Viewer). For the raw image, open the image stack and open the 3D viewer. For the line stack, first generate a line stack in Simple Neurite Tracer (Analysis > Make Line Stack). To add volume to the line stack prior to 3D projection, *see* **Note 9**. Next, import the line stack into 3D viewer. In 3D viewer, objects can be rotated to any angle and snapshots can be taken, videos can also be generated.

3.6 Analysis of Inter-plexus Connections

Required Materials: images from section 3.4 *Cryo-sections*, computer with FIJI software

1. Import montage images into FIJI: This can be accomplished by simply dragging the file into the FIJI window below the toolbar.
2. Preparing the image: To reduce background, use the subtract background function (Process > Subtract Background) and then adjust the brightness contrast (Image > Adjust > Brightness/Contrast).

3.6.1 Inter-plexus Vessel Orientation

1. In FIJI, open the montage images of retina sections created above.
2. Measuring inter-plexus vessel orientation (Figure 3.6 A): Using the “Angle tool”, found on the main FIJI window, begin measuring the orientation of inter-plexus vessels using tangential lines at each spot on the retina. Shown in Figure 3.6 A is an analysis of inter-plexus vessels connecting the SP and IP. This analysis can be performed for inter-plexus vessels connecting the IP to the DP.
3. Repeat step 2 for every inter-plexus vessel in the retina section. In order to remove bias, only measure stretches of vessels longer than a certain length, 10 μm is recommended.
4. Data Handling: Bin the observations in 10° increments (i.e. 0°-10°) and convert the data to the percentage of observations within a particular bin within a retina section.

3.6.2 Inter-plexus Vessel Branching

1. In FIJI, open the montage images of retina sections created above.
2. Measuring vessel branching (Figure 3.6 B): Identify inter-plexus vessel branching and record the observation based upon which retinal layer the branching occurred (SP, RGL, IPL, IP, INL, DP).
3. Repeat step 2 for the entire retina section.
4. Data Handling: Convert the data to the percentage of branch points found within the different retinal layers for a given retina section.

4 NOTES

1. Cutting just above the cornea/sclera boundary (in the cornea), ensures that you will not cut off part of the retina.
2. Since the retina is a hemi-spherical object, sections only near the optic nerve head are perpendicular to the vertical axis of the retinal layers, while sections near the on the extreme ends will be oblique. Only analyzing perpendicular sections is very important, otherwise, vessels will appear to travel in orientations that are not accurate. Additionally, this allows for proper sampling for all of the regions of the retina (central, middle, peripheral).

3. These staining protocols are compatible with antibody staining as previously described***(3)*** Normal donkey serum, or another antibody blocking agent such as bovine serum albumin, needs to be added to the triton buffer solutions (3 ml in 40 ml of total solution). Add GS-B4 to the secondary antibody incubation step.
4. The addition of DAPI will allow for resolution of the nuclear layers and can be helpful when looking at organization of the vessels in whole-mounted retinas. DRAQ5 can be used in place of DAPI at a dilution of 1:1000, if far-red flour is desired.
5. Electrical tape has the ideal thickness for most retinas. If a shallower or deeper well is needed to mount the retina, use a different type of tape or add multiple layers. When cutting a whole out of the tape, a regular office single hole punch works well for most retinas.
6. A humidifier chamber can be made with any container that will create an airtight seal. To keep the chamber moist, lay a paper towel down in the bottom of the container and saturate it with water. Elevate the slides above the paper towel using two closely places wooden dowels (or pencils) or anything else you can think of to accomplish this. Just make sure not to place the slides directly on the paper towel because your solution on the slide will become diluted or wash off completely.
7. The innermost part of the retina, area closest to the optic nerve head, is considered the central retina. The outermost part of the retina, area closest to the iris, is considered the peripheral retina. The area mid-way between the central and peripheral retina is considered the middle retina.
8. Most microscope software has an option to export the data with the metadata. In FIJI, you can verify the size of the field by looking in the top left had corner of the window of the image. If you need to set the scale manually, open the Set Scale function (Analyze > Set Scale...). There you will enter the distance in pixels, known distance, pixel aspect ratio, and the unit of length. Note this will only set your scale in the x,y plane. In order to get the distance correct between serial z-images, open the 3D project function (Image > Stacks > 3D Project...). There you need to make a projection image, but first make sure you insert the proper distance in the “Splice Spacing” box and select “Interpolate”. If the scale is set properly, the projection with have depth, if not, it will remain flat.
9. If you want to add volume to your line stack as shown in Figure 3.5 C, use the fill tool in Simple Neurite Tracer in the “All Paths” window by selecting all of the paths and clicking “Fill Out”. Once filled, select the “Create Image Stack from Fill” in the

"All Fills" window. This can now be saved as an image stack and used to generate a 3D image in the 3D viewer.

REFERENCES

1. Masland RH (2012) The neuronal organization of the retina. Neuron 76 (2):266-280. doi:10.1016/j.neuron.2012.10.002
2. Fruttiger M (2007) Development of the retinal vasculature. Angiogenesis 10 (2):77-88. doi:10.1007/s10456-007-9065-1
3. Simmons AB, Merrill MM, Reed JC, Deans MR, Edwards MM, Fuerst PG (2016) Defective Angiogenesis and Intraretinal Bleeding in Mouse Models With Disrupted Inner Retinal Lamination. Investigative ophthalmology & visual science 57 (4):1563-1577. doi:10.1167/iovs.15-18395
4. Edwards MM, McLeod DS, Li R, Grebe R, Bhutto I, Mu X, Lutty GA (2012) The deletion of Math5 disrupts retinal blood vessel and glial development in mice. Experimental eye research 96 (1):147-156. doi:10.1016/j.exer.2011.12.005
5. Usui Y, Westenskow PD, Kurihara T, Aguilar E, Sakimoto S, Paris LP, Wittgrove C, Feitelberg D, Friedlander MS, Moreno SK, Dorrell MI, Friedlander M (2015) Neurovascular crosstalk between interneurons and capillaries is required for vision. The Journal of clinical investigation 125 (6):2335-2346. doi:10.1172/JCI80297
6. Okabe K, Kobayashi S, Yamada T, Kurihara T, Tai-Nagara I, Miyamoto T, Mukouyama YS, Sato TN, Suda T, Ema M, Kubota Y (2014) Neurons limit angiogenesis by titrating VEGF in retina. Cell 159 (3):584-596. doi:10.1016/j.cell.2014.09.025
7. Kim J, Oh WJ, Gaiano N, Yoshida Y, Gu C (2011) Semaphorin 3E-Plexin-D1 signaling regulates VEGF function in developmental angiogenesis via a feedback mechanism. Genes & development 25 (13):1399-1411. doi:10.1101/gad.2042011
8. Vecino E, Rodriguez FD, Ruzafa N, Pereiro X, Sharma SC (2015) Glia-neuron interactions in the mammalian retina. Progress in retinal and eye research. doi:10.1016/j.preteyeres.2015.06.003
9. Stone J, Itin A, Alon T, Pe'er J, Gnessin H, Chan-Ling T, Keshet E (1995) Development of retinal vasculature is mediated by hypoxia-induced vascular endothelial growth factor (VEGF) expression by neuroglia. The Journal of neuroscience : the official journal of the Society for Neuroscience 15 (7 Pt 1):4738-4747

10. Shen W, Fruttiger M, Zhu L, Chung SH, Barnett NL, Kirk JK, Lee S, Coorey NJ, Killingsworth M, Sherman LS, Gillies MC (2012) Conditional Mullercell ablation causes independent neuronal and vascular pathologies in a novel transgenic model. The Journal of neuroscience : the official journal of the Society for Neuroscience 32 (45):15715-15727. doi:10.1523/JNEUROSCI.2841-12.2012
11. Dorrell MI, Aguilar E, Friedlander M (2002) Retinal vascular development is mediated by endothelial filopodia, a preexisting astrocytic template and specific R-cadherin adhesion. Investigative ophthalmology & visual science 43 (11):3500-3510
12. Gnanaguru G, Bachay G, Biswas S, Pinzon-Duarte G, Hunter DD, Brunken WJ (2013) Laminins containing the beta2 and gamma3 chains regulate astrocyte migration and angiogenesis in the retina. Development 140 (9):2050-2060. doi:10.1242/dev.087817
13. Scott A, Powner MB, Gandhi P, Clarkin C, Gutmann DH, Johnson RS, Ferrara N, Fruttiger M (2010) Astrocyte-derived vascular endothelial growth factor stabilizes vessels in the developing retinal vasculature. PloS one 5 (7):e11863. doi:10.1371/journal.pone.0011863
14. Arnold T, Betsholtz C (2013) Correction: The importance of microglia in the development of the vasculature in the central nervous system. Vascular cell 5 (1):12. doi:10.1186/2045-824X-5-12
15. Hartnett ME (2016) Advances in understanding and management of retinopathy of prematurity. Survey of ophthalmology. doi:10.1016/j.survophthal.2016.12.004
16. Lutty GA (2013) Effects of diabetes on the eye. Investigative ophthalmology & visual science 54 (14):ORSF81-87. doi:10.1167/iovs.13-12979
17. Mehta S (2015) Age-Related Macular Degeneration. Primary care 42 (3):377-391. doi:10.1016/j.pop.2015.05.009
18. Linkert M, Rueden CT, Allan C, Burel JM, Moore W, Patterson A, Loranger B, Moore J, Neves C, Macdonald D, Tarkowska A, Sticco C, Hill E, Rossner M, Eliceiri KW, Swedlow JR (2010) Metadata matters: access to image data in the real world. The Journal of cell biology 189 (5):777-782. doi:10.1083/jcb.201004104
19. Longair MH, Baker DA, Armstrong JD (2011) Simple Neurite Tracer: open source software for reconstruction, visualization and analysis of neuronal processes. Bioinformatics 27 (17):2453-2454. doi:10.1093/bioinformatics/btr390

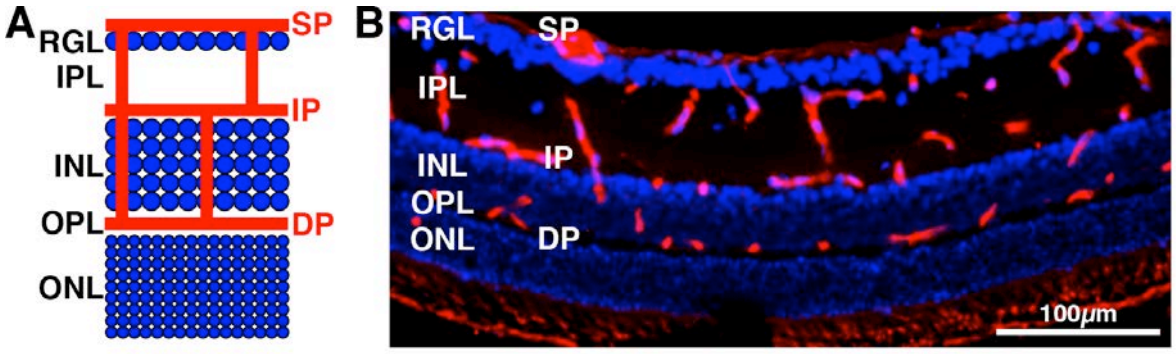

Figure 3.1. Organization of the mouse retina. (A) Cartoon illustration of the retina, showing its organization. (B) Cross-section of a mouse retina stained with DAPI and GS-B4 to label nuclei and the vasculature, respectively.

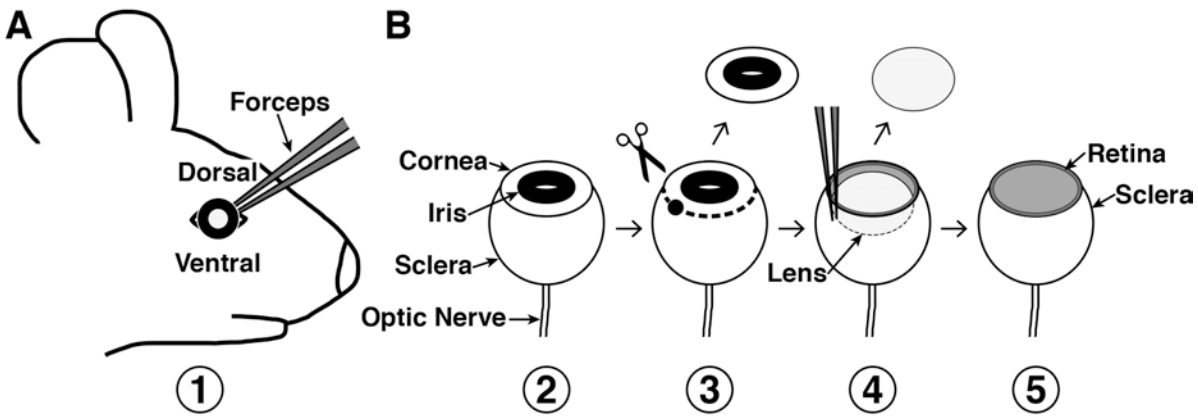

Figure 3.2. Diagram showing the enucleating and hemisecting processes. This diagram shows the processes of removing and dissecting the eye in preparation for the fixing process. (A) Enucleation (Steps 1-2). Apply pressure above (dorsally) and below (ventrally) the eye socket until the eye bulges out slightly and grasp the optic nerve with forceps and gently remove eye. Place eye in dissecting dish filled with PBS. (B) Hemisection (Steps 3-5). Poke a pilot hole at the cornea/sclera boundary with a needle and use microdissection scissors to cut and remove the cornea and iris (Step 3). Next, remove the lens with forceps (Step 4). Now the hemisected eye – sclera, retina, and optic nerve – can be placed in fixative (Step 5).

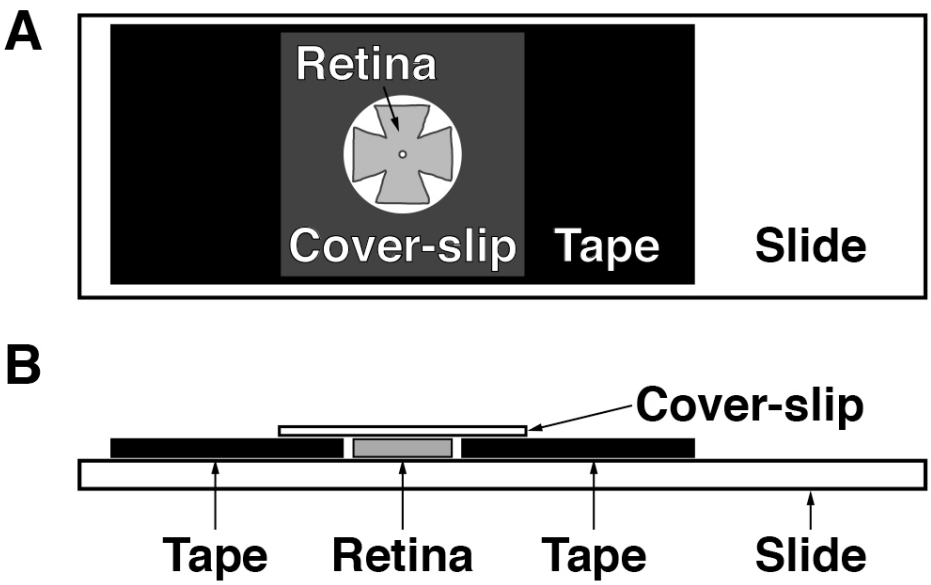

Figure 3.3. Diagram of whole-mounted retina preparation. This preparation minimizes the squishing of the retina, which will distort the vasculature, by using a spacer made from electrical tape. (A) View looking down at the slide preparation. (B) View looking at the side of the preparation to visualize the orientation of the different layers.

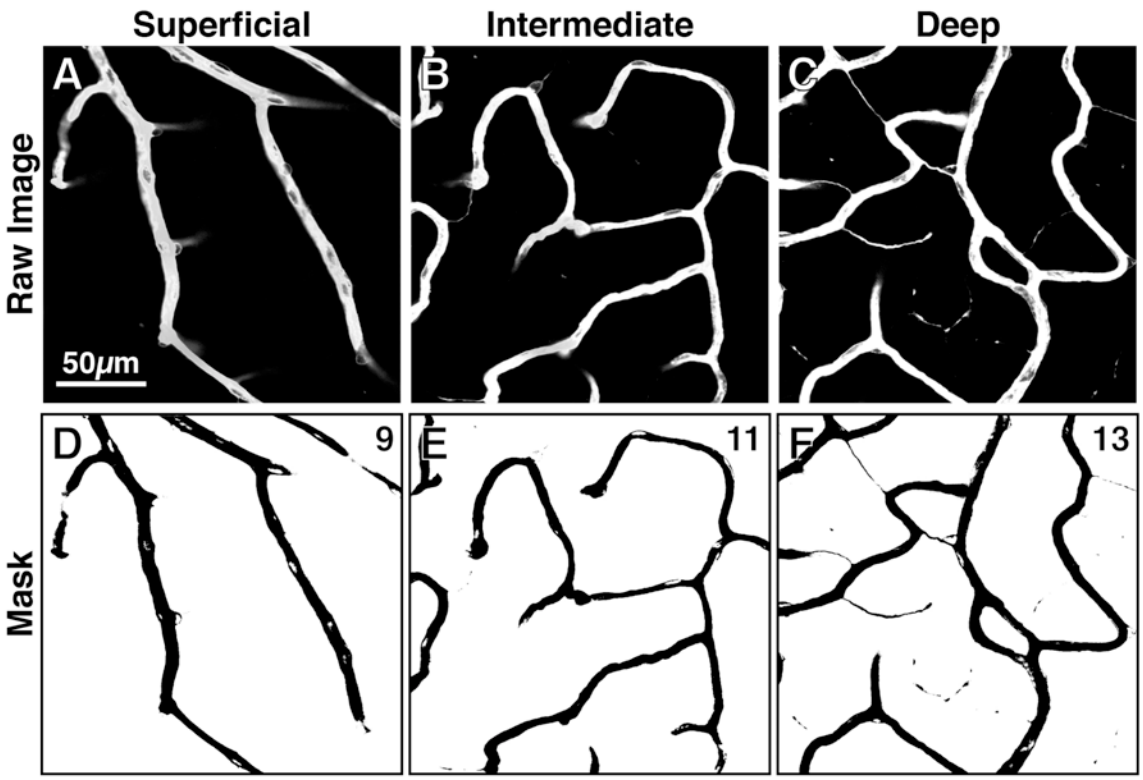

Figure 3.4. Analyzing vascular coverage of each plexi. (A-C) Z-projection images for each of the vascular plexi generated from a single image series taken through a single point in a whole-mounted retina. Background has been eliminated in FIJI. (D-F) Mask of the z-projection images generated by the Make Binary function in FIJI. Number in the top right corner is the % coverage measured by the Analyze Particles function in FIJI.

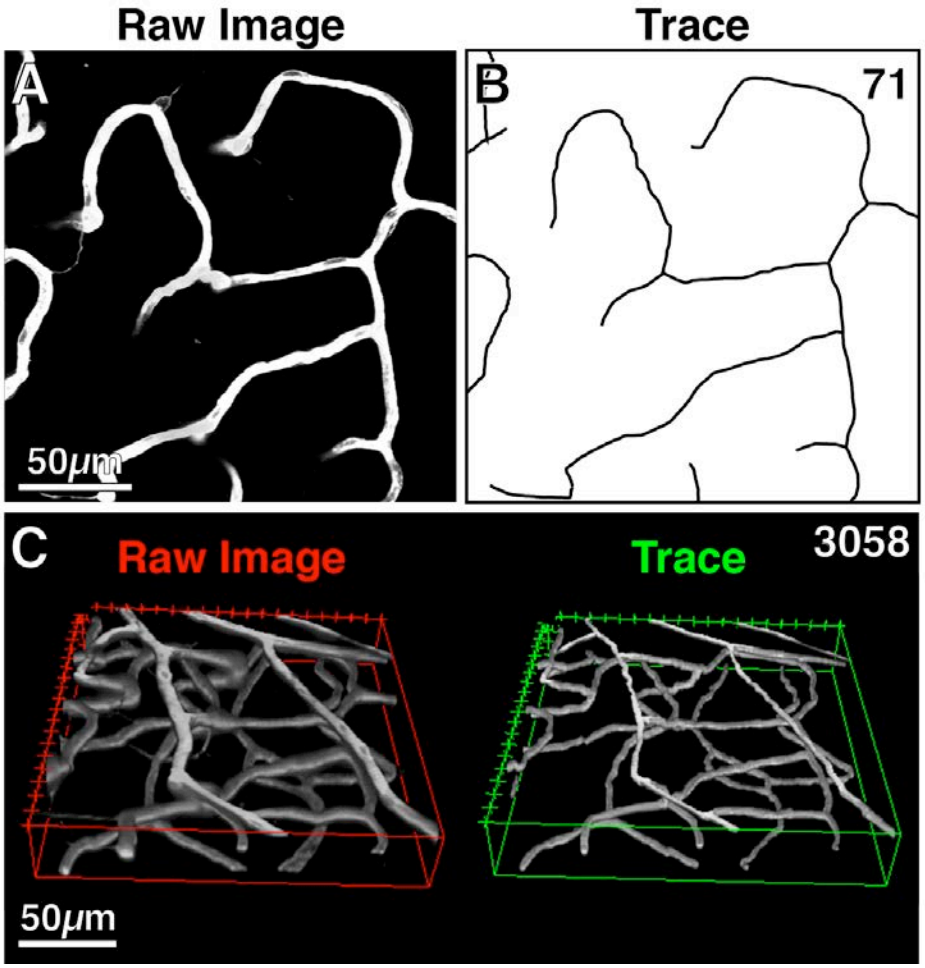

Figure 3.5. Tracing and measuring vessels. (A) Z-projection image of the IP from Figure 3.3. (B) Trace generated from the line-stack exported from Simple Neurite Tracer. (C) 3D viewer snap shots of the same image series used in Figure 3.3 and a trace of the very same stack exported from Simple Neurite Tracer, after partially filling the trace. The numbers in the top right corners of B and C are the total length of vessels measured in micrometers.

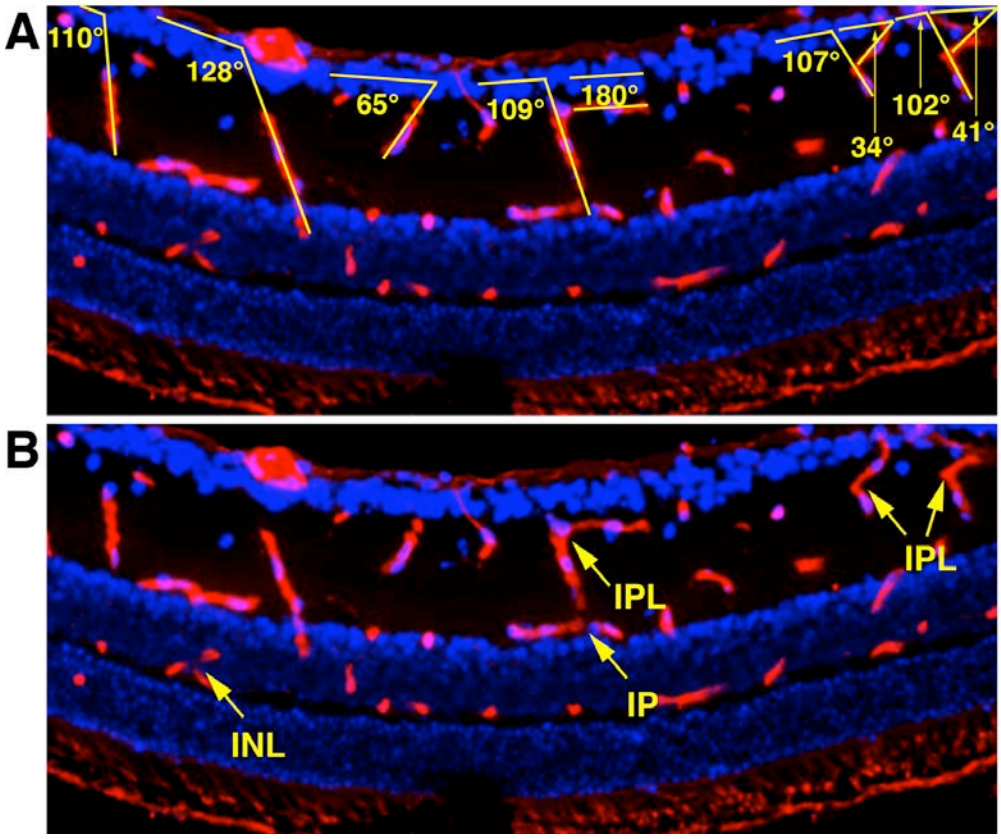

Figure 3.6. Measuring inter-plexus orientation and branching. The sections used here are the same as the image in Figure 3.1. (A) The orientations of the inter-plexus vessels within the IPL are measured with respect to tangential lines along the retina. This analysis can also be performed for inter-plexus vessels in the INL. (B) Branching of the inter-plexus vessels marked with arrows. The text refers to which retinal layer the branch point is found.

Chapter 4: Non-selective OFF bipolar cell plasticity is inhibited by DSCAM mediated enforcement of dendritic and axonal outgrowth in the adult mouse retina

Aaron B. Simmons, Samuel J. Bloomsburg, Joshua M. Sukeena, Calvin J. Miller, Yohaniz Ortega-Burgos, Bart G. Borghuis, and Peter G. Fuerst

Current Status: Submitted to *Neuron*

ABSTRACT

Mature neurons in the central nervous system are limited in their ability to extend neurites and make novel connections, a process termed plasticity, but the mechanisms inhibiting plasticity in mature neurons remain largely unknown. In this study, we explore the limits to which mature retinal bipolar cells (BCs) are able to make novel connections in the adult mouse retina. Remarkably, we discover that OFF BCs retain the ability to make new connections within the constraints of their tiled dendritic fields well beyond when the retina is considered mature. We find that Down syndrome cell adhesion molecule (*Dscam*) limits BC plasticity by preventing neurite outgrowth through homotypic recognition and enforcement of dendrite and axonal tiling. Conditional deletion of *Dscam* during development results in the expansion of dendrite and axon arbors and the loss of tiled territories. We then go on to confirm that these enlarged arbors make connections that are physiologically active. Finally, we find that deletion of *Dscam* in the mature retina is sufficient to trigger neurite outgrowth and the birth of novel connections.

INTRODUCTION

Developing neurons readily extend axons and dendrites and make novel synaptic connections. However, the ability of mature neurons to make novel contacts in response to triggers such as damage and degeneration, a process termed plasticity, widely varies among different types of neurons. Within the peripheral nervous system, mature neurons are readily able to make novel connections, while mature neurons in the central nervous system (CNS), are much more limited in their ability to make generate novel circuitry.

Factors that limit plasticity include the post-mitotic state of most CNS neurons (Thakurela et al., 2015), establishment of the extracellular matrix (De Luca and Papa, 2016, Fawcett, 2015), elements of the immune system (Levin and Godukhin, 2017, Tay et al., 2017), and intrinsic factors limiting neuron axon and dendrite outgrowth (Sun et al., 2011, Steketee et al., 2014). A better understanding of the intrinsic and extrinsic factors that limit neural plasticity has long been recognized as a barrier to enhancing the clinical treatment of neurological disorders (Fernandez-Hernandez and Rhiner, 2015, Rodriguez and Verkhratsky, 2011, Schmidt and Minnerup, 2016).

In this study, we identify the Down syndrome cell adhesion molecule (Dscam) as an intrinsic factor that limits plasticity in the retina's OFF bipolar cells (BCs) by inhibiting outgrowth of both dendritic and axonal arbors. BCs are the sole excitatory connection between the retina's photoreceptors and all retinal ganglion cells (RGCs), the output cells of the retina. Ability of these BCs to establish novel connections is therefore essential to cell therapy approaches to regenerate and reconnect the retina after damage to either the inner or outer retina. Here, we find that BCs retain a surprising degree of plasticity in the mature retina and readily make novel connections within a constrained territory out to at least six-months of age, well after when the mouse retina is considered mature at approximately one-month of age(Gibson et al., 2013). Furthermore, we find that the tiled dendritic and axonal territories of BCs are enforced by homotypic recognition mediated by DSCAM. Physiology experiments confirm that expanding arbors make novel synaptic connections and suggest that activating dendrite outgrowth by targeting *Dscam* or its downstream signaling network may be an effective strategy to stimulate synaptogenesis. In support of this, targeting *Dscam* deletion in the mature retina is sufficient to activate BC dendrite outgrowth and increase the number of presynaptic connections made with cones.

MATERIALS AND METHODS

Mouse Strains and Handling. Mice were handled in accordance with protocols approved by the Animal Use and Care Committees at the University of Idaho and the University of Louisville. In this study, two different transgenic mouse lines manipulating *Dscam* were used: (1) $Dscam^{tm1Pfu}$ (referred to as $Dscam^{FF}$)(Fuerst et al., 2012) and (2) $Dscam^{tm1.1Pfu}$ (referred to as $Dscam^{-/-}$)(Fuerst et al., 2012); one Cre-reporter mouse was used: Gt(ROSA)26Sortm9(CAG-tdTomato)Hze (referred to as *Ai9*, The Jackson Laboratory, stock

no:007909)(Madisen et al., 2010); three Cre transgenic mouse lines were used: (1) Tg(Htr2a-cre)KM207Gsat (referred to as *HTR:Cre*, MMRRC, stock no:036750)(Lu et al., 2013), (2) *Pou4f2:Cre* (courtesy of Dr. Vann Bennett; Duke University)(Simmons et al., 2016a), (3) Gt(ROSA)26Sortm1(cre/ERT2)Tyi (referred to as *CreER*, The Jackson Laboratory, stock no:008463)(Ventura et al., 2007); and one GFP transgenic mouse was used: 5-HTR2a-EGFP (referred to as *HTR:GFP*, MMRRC, stock no:DQ118)(Lu et al., 2009). Mice were maintained on a mixed genetic background containing C57BL/6, C3H, 129, and FVB. Mutant alleles of *Pde6b* were crossed out of colony. Mice were fed ad-libitum and kept on 12h light/dark cycles. A minimum of three retinas from three mice were used in each measurement, unless otherwise stated.

Genotyping. The genotyping of mice followed a procedure as previously described(Simmons et al., 2016a), while the primers used can be found in the following publications: $Dscam^{FF}$ (Fuerst et al., 2012); $Dscam^{-/-}$ (Fuerst et al., 2012); *Ai9* (Madisen et al., 2010); *HTR:Cre* (Lu et al., 2013); *Pou4f2:Cre* (Simmons et al., 2016a); *HTR:GFP* (Lu et al., 2009). All mice taken for study were given a unique alphabetical code that was dissociated from the genotypes to those performing experiments until the data was completely collected and recorded. Tail biopsies were taken from each mouse in the instance that the genotype of a coded retina would need to be verified.

Microscopy. Micrographs were captured using either a Nikon Spinning Disk confocal microscope (Melville, NY, USA) or an Olympus Scanning Laser confocal microscope (Center Valley, PA, USA). Any processing of the images was performed in FIJI (National Institutes of Health, Bethesda, MD, USA) and/or Adobe Photoshop (Adobe Systems, Inc., San Jose, CA, USA). Any changes to brightness or contrast were performed uniformly across the image.

Immunohistochemistry. Immunohistochemistry (IHC) was performed as previously described(Li et al., 2015). In all images containing *HTR:GFP*, the GFP was amplified using IHC; however, the RFP from the *Ai9* reporter was never amplified.

Antibodies and Stains. *Primary antibodies:* rabbit anti-calbindin (CB-38a, 1:500; Swant, Switzerland); mouse anti-calsenilin (05-756, 1:1000; Millipore, Darmstadt, Germany); mouse anti-DSCAM (MAB36661,1:50; R&D Systems, Minneapolis, MN, USA); mouse anti-dystroglycan (MANDAG2(7D11); 1:500; developed by Morris, G.E., Developmental Studies Hybridoma Iowa City, IA, USA); mouse anti-GFP (75-132, 1:250; NeuroMab, Davis, CA,

USA); mouse anti-PKARIIβ (610625, 1:1000; BD Biosciences, San Jose, CA, USA); rabbit anti-TH (AB152; 1:500; Millipore). *Secondary antibodies:* all secondary antibodies were used at 1:500 (Jackson ImmunoResearch, West Grove, PA, USA). *Stains:* 4′,6-diamidino-2-phenylindole (DAPI) (4083, 1:50,000 from 1 mg/mL stock; Cell Signaling Technology); peanut lectin (PNA) (L21409, L32460; 1:500; Molecular Probes, Eugene, OR, USA).

Statistical Analysis. All statistical analyses were performed in Microsoft Excel. A summary of the statistical tests performed and p-values for each measurement can be found in Table 4.S1. In short, to test for statistical differences between two groups with numerical data, a Student's *t*-test was performed; between two groups of categorical data, a hypothesis test comparing two independent proportions was performed; and between groups of three or more with numerical data, a one-way ANOVA with a Tukey-Kramer post-hoc test was performed. A p-value < 0.05 was considered statistically different and is denoted by an asterisk in the graphs. Error bars in all graphs are ±SEM.

HTR:Cre Targeting Efficiency and Effects. The efficiency of *HTR:Cre* targeting was confirmed by analyzing the percent of RFP+ BC4s in mice carrying *HTR:Cre* and *Ai9* in cryosections of retina counterstained with anti-calsenilin, a marker specific to BC4s(Haverkamp et al., 2008). We determined that ~80% of BC4s are targeted by *HTR:Cre,* consistent with what was previously reported (Figure 4.S1 D-E)(Lu et al., 2013). For reporter activity, a minimum of 10 images from at least two retinas gathered from at least two mice analyzed at each time-point. To confirm that *HTR:Cre* targets the floxed allele of *Dscam*, $Dscam^{FF\ HTR:Cre}$ mice were cryo-sectioned and stained with anti-DSCAM and anti-calsenilin antibodies. Accumulation of DSCAM protein in the cytosol is observed after the transmembrane domain is removed by cre-mediated recombination(de Andrade et al., 2014b). Targeting of the floxed allele of *Dscam* was observed as early as P13, the earliest analyzed time-point (Figure 4.S1 D, inset). The effects of *HTR:Cre* targeting of $Dscam^{FF}$ were analyzed (Figure 4.S1). *HTR:Cre* targeting of $Dscam^{FF}$ sufficient to induce previously described defects in organization in BC4s, with no differences in cell number (Figure 4.S1 A-C and H-M)(de Andrade et al., 2014b). No differences in the cell number or organization of cones, BC3bs or dopaminergic amacrine cells (DACs) were detected when comparing $Dscam^{FF\ HTR:Cre}$ to $Dscam^{+/+}$ (Figure 4.S1 F-G and N-AE).

Cell Counts. *Whole populations:* Eight images (four central, four peripheral), equally sampled from the dorsal, ventral, nasal, and temporal regions, were captured from whole-

mount retinas stained with cell type specific markers at 1µm increments along the z-axis. 60x magnification (44,944µm^2 field size) was used to capture BC4s, BC3bs and cones. 20x magnification (160,000µm^2 field size) was used to capture DACs. Image stacks were then imported into FIJI and the cell bodies were manually marked using the multi-point tool. The total number of cells per retina was then calculated by extrapolating the total cells counted in those eight images to the total area of the retina. Retina area was quantified by montage imaging the entire whole-mount retina and using the polygon tool in FIJI. *Thickness of retinal layers:* this was performed as previously described(Simmons et al., 2016b).

Cell Spacing. Comma separated values (CSV) files, which document the x,y coordinates of each point created, were created in FIJI after manual marking the cells for cell counts. CSV files were imported into WinDRP and two metrics of spacing were calculated and recorded: the nearest neighbor regularity index (NNRI) and the packing factor(Rodieck, 1991).

Quantifying BC4 characteristics. Genetically labeled BC4s (*HTR:Cre x Ai9*) were imaged from the dendrites to the distal end of the cell bodies at 60x magnification at 0.3µm along the z-axis (Figure 4.S4). Anti-calsenilin antibody was used to confirm that each cell was a BC4 and counterstained with PNA to visualize cones. Z-stack images were then imported into FIJI and the following metrics were assessed. *Dendrite tips:* each of the dendrite tips was mapped using the multipoint tool and further characterized into categories, total dendrite tips, dendrite tips per cone, dendrite tips not at cone. *Cones contacted:* this is the total number of cones a BC4 contacts. A cone was considered contacted if the dendrite arbor was co-localized within PNA staining. *Non-cone contacts:* to determine if dendrite tips not at cone were contacting rods, whole-mount retinas where the BC4s were labeled genetically (*HTR:Cre x Ai9*) where counterstained with PNA and dystroglycan, a marker that is found at the base of rod and cone terminal ribbon synapses (de Andrade et al., 2014b). *Dendrite area:* convex polygons were drawn around the dendritic field in the x,y plane using the polygon tool and the area was measured. This measurement was also performed on Ai9(-) cells in the *Dscam$^{FF\ HTR:cre}$* retinas with calsenilin staining. *Dendrite overlap:* dendrite areas of whole fields were outlined and the overlap between neighboring cells was quantified at percent overlap of each BC4 dendrite field. To ensure that our results were accurate, fields with BC4s that were Ai9(+) and Ai9(-) were reconstructed because of their differential labeling. *Dendrite length:* Z-stacks were imported into the FIJI plugin, Simple Neurite Tracer(Longair et al., 2011), where the neurons were manually traced to generate a skeleton of the dendrite arbors. The total length of these skeletons

was measured and recorded. For *Pouf42:Cre* experiments, *HTR:GFP* was used to label BC4s(Lu et al., 2009) and the following metrics were measured: dendrite area, cones contacted, and dendrite overlap. For BC4 axons, BC4s were labeled with a combination of genetics (*HTR:Cre x Ai9* and *HTR:GFP*) and the following metrics were measured: axon area and total overlap with neighboring BC4 axons. A minimum of 30 cells were used for each condition in each of the measurements at each age. For 6m data, four retinas from two mice were analyzed.

Quantifying BC3b characteristics. *HTR:Cre* is expressed by ~1% BC3bs, consistent with a previous report (data not shown)(Lu et al., 2013). To visualize BC3bs, they were labeled genetically (*HTR:Cre x Ai9*) and counter-stained with PKARIIβ(Mataruga et al., 2007). BC3bs were analyzed at one month of age in both the $Dscam^{+/+}$ and $Dscam^{FF\ HTR:Cre}$ retinas. The measurements were performed following the same protocols outlined for the BC4s. A minimum of 27 cells were used for each condition in each of the measurements.

Quantifying BC4 dendrite organization at the cone synapse. To quantify the total amount of BC4 dendrites at a cone synapse, BC4s in 3m whole-mount retinas were genetically labeled (*HTR:Cre x Ai9*) and counter stained with anti-calsenilin and PNA. In FIJI, cones contacted by a single genetically labeled BC4 were randomly selected from an image, cropped and then a z-projection was generated that captured all of the PNA and Ai9. Binary masks were created for each channel using the threshold tool and the amount of Ai9 area overlapping with the PNA area was measured. After the measurements were complete, the data was split into cones with only 1BC4 contact, ≥BC4 contacts and combined data by adding on the calsenilin staining to reveal the entire BC4 population. To quantify the amount of BC4 dendrite crossing at the cone synapse, BC4 dendrites at the cone were traced in FIJI and each BC4/Cone connection was classified as either crossing or not crossing. Dendrites that could not be resolved were considered not crossing even if clumping was evident. The following sample sizes were used: 101($Dscam^{+/+}$) and 108($Dscam^{FF\ HTR:Cre}$) BC4/cone contacts for Ai9/PNA overlapping, 63($Dscam^{+/+}$) and 42($Dscam^{FF\ HTR:Cre}$) BC4 dendrite crossing at the cone synapse.

DSCAM localization. All DSCAM localization was performed in cryo-sections of $Dscam^{+/+}$ retinas by staining them with antibodies against *HTR:GFP*, calsenilin and DSCAM. Confocal images were then taken using a scanning laser confocal microscope at 60x x2 magnification, sampling at 0.5μm increments about the z-axis. Image stacks were then

taken into FIJI where there were analyzed by the following metrics. *DSCAM localization on BC4 dendrites:* dendrite tips and cell bodies of BC4s and DSCAM co-localized to BC4 dendrites were identified and marked using the multipoint tool. This distance from DSCAM puncta to the nearest dendrite tip was measured by tracing from the puncta, along the dendrite, to the terminal. Also, the length of each dendrite was measured in the same way, but from the dendrite tip back to the cell body. *DSCAM co-localization with BC4 axons:* using images stacks, volumes surrounding isolated BC4 axons were identified and all of the DSCAM puncta within that area were marked with the BC4 axon channel hidden. Then the channel was made visible and the puncta co-localized with the axon were recorded. As a control, the BC4 axon channel was flipped about the horizontal axis and the measurement was performed again. A minimum of seven cells were used for each measurement.

Tamoxifen dosing. Tamoxifen (T5648; Sigma Aldrich) was dissolved at 20 mg/ml in sesame seed oil by incubation at 37 °C until dissolved (about 4 hours). 100 µl of tamoxifen solution was administered by intraperitoneal injection daily for five days starting at postnatal day 30. Mice were maintained for an additional three months before being taken for study.

RESULTS

BC4s are competent to make novel connections in the adult retina

The retina contains two broad categories of BCs that serve as the sole excitatory connection between photoreceptors and downstream neurons(Euler et al., 2014). ON BCs are responsive to light increment, whereas OFFs are responsive to light decrement(Masland, 1986, Miller and Dacheux, 1976, Schiller et al., 1986, Slaughter and Miller, 1981). The synaptic organization of ON and OFF BCs are significantly different in mammalian species, with ON BCs making invaginating contacts at the base of photoreceptor ribbon synapses, while OFF BCs make flat contacts at the base of invagination (Hopkins and Boycott, 1992, Boycott and Hopkins, 1991, Wassle et al., 1978, Carter-Dawson and LaVail, 1979, Wassle et al., 2009, Tsukamoto and Omi, 2014). Physiological response is also different with ON BCs detecting glutamate release through metabotropic glutamate receptors, while OFF BCs utilize a mixture of AMPA and kainite type ionotropic glutamate receptors (Puller et al., 2013, Borghuis et al., 2014, Lindstrom et al., 2014, Ichinose and Hellmer, 2016). The dynamics of ON BC dendrite outgrowth and

connectivity have previously been characterized(Lee et al., 2011, Dunn and Wong, 2012, Dunn et al., 2013, Morgan et al., 2006), but similar studies have not been performed for OFF BCs. ON BCs make an adult complement of synaptic connections early during development with varying degrees of refinement(Dunn and Wong, 2012). Utilizing transgenic markers and antibody reagents to label OFF BCs we find OFF BCs continue to elaborate their dendrite arbors and make novel connections in the wild type adult retina.

In the adult retina Type 4 OFF BC, BC4, dendrite arbors tile with one another (Figure 4.1 A) while making flat contacts at the base of rods and cones(Haverkamp et al., 2008, Tsukamoto and Omi, 2014). A number of reagents exist to visualize BC4s including a cell-type specific marker—calsenilin(Haverkamp et al., 2008) and transgenic mouse lines driving the expression of cre-recombinase and green fluorescent protein (GFP) specifically in BC4s (Lu et al., 2009, Lu et al., 2013). Here, these reagents were utilized to label and characterize the development of BC4s starting at postnatal day 15 (P15) out to six months of age. Surprisingly, BC4s continue to elaborate their dendrite arbors out to six months of age (Figure 4.1 B-C), something that was also true for BC4 innervation of cones (Figure 4.1 D-H). To quantify these changes, we first measured the gross morphology of BC4 dendritic arbors and detected significantly increasing trends in both the area occupied by and the total length of BC4 dendrites starting at P15 and leveling off between 3-6m (Figure 4.1 I-J). When analyzing BC4 connectivity, no differences in the amount of cones contacted were detected (Figure 4.1 K). However, significant increasing trends were detected in the numbers of BC4 dendrite tips sampling each cone, dendrite tips not at cones, and in the total amount of dendrite tips per BC4 (Figure 4.1 L-N). Taken together, these data suggest BC4s remain competent to make connections in the adult retina; however, this ability is confined within the tiled dendritic fields.

DSCAM limits BC4 plasticity by enforcing tiling of dendritic arbors.

The observed extended plasticity within the tiled BC dendrite fields led to the speculation that OFF BCs could remain competent to make synaptic connections outside of their tiled dendritic territory, but are prevented from doing so by homotypic inhibition from neighboring BC4s. A promising candidate to mediate such inhibition is the Down syndrome cell adhesion molecule (*Dscam*), which is expressed in all non-selective OFF BCs in the mouse retina, that is, those making contacts with both blue and green cone types (de

Andrade et al., 2014b, Euler et al., 2014). To manipulate *Dscam* expression we utilized *HTR:Cre*, which efficiently targets *Dscam* deletion in BC4s with minimal disruption to retinal organization (Figure 4.S1). Of note, *HTR:Cre* targets Dscam deletion in most BC4s but some non-targeted cells remain, allowing measurement of both wild type ($Dscam^{NonTar}$) and targeted ($Dscam^{Tar}$) BC4s in the same retina (Figure 4.S1 D), thereby providing an internal control for non-specific phenotypes caused by off target Cre activity in retinal ganglion and amacrine cells.

To address the influence of *Dscam* on BC4 dendrite morphogenesis, BC4s within $Dscam^{+/+}$ and $Dscam^{FF\ HTR:Cre}$ retinas were analyzed between P15 and 6m (Figure 4.2 A-B). At every time-point, significant increases were detected when comparing the dendrite areas of $Dscam^{Tar}$ and $Dscam^{NonTar}$ BC4s to $Dscam^{+/+}$ BC4s, while significant decreases were detected when comparing $Dscam^{NonTar}$ BC4s to $Dscam^{Tar}$ BC4s at P21 and 6m (Figure 4.2 C). Here it is important to note that DSCAM primarily acts as a homotypic cell adhesion molecule and wild type cells adopt a mutant phenotype next to mutant cells of the same type (Fuerst et al., 2012). Significant increases in dendrite length were also detected in $Dscam^{Tar}$ BC4s to that of $Dscam^{+/+}$ BC4s (Figure 4.2 D). As a test for dendrite tiling, the amount of overlap was measured between neighboring BC4s in both the $Dscam^{+/+}$ and $Dscam^{FF\ HTR:Cre}$ retinas (Figure 4.2 E). We found negligible dendrite overlap when analyzing $Dscam^{+/+}$ or $Dscam^{NonTar}$ BC4 pairs; however, when analyzing $Dscam^{Tar}$-$Dscam^{NonTar}$ pairs, BC4s dendrite arbors overlapped extensively with one another. No statistical differences in retina area were detected at any time-point (Figure 4.2 F). *Dscam* was also found to act in a dosage dependent manner, consistent with previous results (Fuerst et al., 2008, Keeley et al., 2011, Li et al., 2015) (Figure 4.S2). Taken together, these data support a model in which BC4s utilize *Dscam* mediated homotypic recognition to inhibit dendrite outgrowth.

BC4s are competent to make functional connections outside of their tiled dendrite territories when DSCAM inhibition is removed.

With the loss of dendrite tiling, we wanted to test if this resulted in an increase in the number of pre-synaptic connections made by BC4s. To address this, the connectivity of $Dscam^{+/+}$, $Dscam^{Tar}$, $Dscam^{NonTar}$ BC4s were analyzed and compared between P15 and 6m (Figure 4.3 A-C). At every time-point, significant increases in number of cones contacted were detected in $Dscam^{Tar}$ and $Dscam^{NonTar}$ BC4s when compared to $Dscam^{+/+}$ BC4s (Figure

4.3 D). Additionally, significant increases were detected in the number of cones contacted by *Dscam*^{Tar} BC4s when compared to *Dscam*^{NonTar} BC4s at three and six months of age. Significant increases in the total dendrite tips, dendrite tips per cone, and dendrite tips not at cone in *Dscam*^{Tar} BC4s were also detected when compared to *Dscam*$^{+/+}$ BC4s (Figure 4.3 E-G). To determine whether dendrite tips not ending in cones were ending at rods, retinas were stained with a marker specific to synaptic clefts, dystroglycan, in conjunction with PNA (Figure 4.3 H). No significant differences were detected in the number of rods contacted by *Dscam*$^{+/+}$ and *Dscam*^{Tar} BC4s; however, significant increases in the dendrite tips ending at neither photoreceptors was detected in *Dscam*^{Tar} BC4s, compared to *Dscam*$^{+/+}$ BC4s (Figure 4.3 I). Again, *Dscam* was also found to act in a dosage dependent manner, consistent with previous results (Fuerst et al., 2008, Keeley et al., 2011, Li et al., 2015) (Figure 4.S3).

During analysis of BC4 dendrites, we noticed that *Dscam*^{Tar} BC4 innervation of cones was highly disorganized and the dendrites of a single BC4 appeared to clump together, compared to *Dscam*$^{+/+}$ BC4s (Figure 4.4 A). To quantify these changes, the density of dendrites from a single genetically labeled BC4 sampling a single cone was quantified (Figure 4.4 B). These data were then split into whether cones were innervated by 1 or ≥2 BC4s as determined by labeling the entire BC4 population with calsenilin. *Dscam*^{Tar} BC4 dendrites covered significantly more of the cone, compared to *Dscam*$^{+/+}$ BC4s, while the total number of multiply innervated cones is increased in the *Dscam*$^{FF\ HTR:Cre}$ retina (Figure 4.4 C). To further measure the organization of BC4 dendrites innervating cones, individual BC4 cone innervations were reconstructed and the proportion of innervations with crossing dendrites were logged (Figure 4.4 D-E). A significant increase in the proportion with crossing dendrites was detected in *Dscam*^{Tar} BC4s, compared to *Dscam*$^{+/+}$ BC4s. We then mapped out the location of DSCAM protein along BC4 dendrites and found it to be localized along the distal dendrite and not just at the dendrite terminals (Figure 4.4 F-G).

DSCAM limits BC4 plasticity by enforcing tiling of axonal arbors.

Despite their name BCs have easily recognized axons and dendrites. DSCAM function differs in the axons and dendrites of cells such as retinal ganglion cells, in which it prevents dendrite clumping (Fuerst et al., 2008) but promotes axon growth (Fernandes et al., 2016). To test if DSCAM has the same function in BC axons and dendrites we

confirmed that DSCAM protein was localized to *Dscam*$^{+/+}$ BC4 axons (Figure 4.5 A-C). Next, we analyzed and compared axon tiling within *Dscam*$^{+/+}$ and *Dscam*$^{FF\ HTR:Cre}$ retinas (Figure 4.5 D-E). To do this, *Dscam*^{NonTar} BC4 axons that were isolated and surrounded only by *Dscam*^{Tar} BC4s were analyzed and compared to *Dscam*$^{+/+}$ BC4 axons. In this environment, *Dscam*^{NonTar} BC4s became statistically larger and overlapped more with neighboring BC4 axons, compared to *Dscam*$^{+/+}$ BC4 axons (Figure 4.5 F-G).

DSCAM limits plasticity in other non-selective OFF BCs.

Dscam is expressed in all non-selective OFF bipolar cells (de Andrade et al., 2014b). We next measured if DSCAM is required to inhibit dendrite outgrowth in another *Dscam* expressing OFF BC, BC3b. Analysis of BC3bs was possible because *HTR:Cre* targets ~1% of BC3bs (Lu et al., 2013), allowing for the differential labeling and targeting of *Dscam*^{FF} in sparsely targeted BC3bs (Figure 4.6 A-B). BC4s were easily distinguished from BC3bs because the retinas were counter-stained with anti-PKARIIβ, a marker specific to BC3bs (Mataruga et al., 2007). Significant increases in the number of cones contacted and the dendrite areas were detected in *Dscam*^{Tar} BC3bs, compared to *Dscam*$^{+/+}$ or *Dscam*^{NonTar} BC3bs (Figure 4.6 C-D). When measuring the amount of dendrite overlap, significant increases were detected in *Dscam*^{Tar}-*Dscam*^{NonTar} BC3b pairs, compared to *Dscam*$^{+/+}$ or *Dscam*^{NonTar} BC3bs pairs (Figure 4.6 E).

BC4 plasticity within the mature retina is inhibited by DSCAM.

To test whether the restriction of BC4 plasticity by DSCAM is needed in the mature retina, late deletion of *Dscam* was accomplished using *Pou4f2:Cre*, which targets the conditional allele of *Dscam* a little after one-month of age (Simmons et al., 2016a). BC4s in retinas targeted by *Pou4f2:Cre*, *Dscam*$^{FF\ Pou4f2:Cre}$, were analyzed and compared to littermate controls, before and after *Pou4f2:Cre* mediated recombination. When measured before recombination, at one-month of age (Figure 4.7 A-B), no significant differences in dendrite area, dendrite overlap, or cones contacted were detected between *Dscam*^{FF} and *Dscam*$^{FF\ Pou4f2:Cre}$ BC4s (Figure 4.7 E-G), a time point at which a phenotype is clearly observed in the *Dscam*$^{FF\ Htr:Cre}$ retina. When comparing these BC4s targeted with *Pou4f2:Cre* at three and six-months of age (Figure 4.7 C-D), significant increases in all of

these measurements were detected (Figure 4.7 E-G). No significant differences in retina area were detected at any of the time-points (Figure 4.7 H).

To test whether chances in BC4 morphology and connectivity were not secondary to early changes in RGCs by *Pou4f2:Cre*, the inducible *CreER* system (Ventura et al., 2007) was used to target the conditional *Dscam* allele. $Dscam^{FF}$ and $Dscam^{FF\ CreER}$ mice were injected with tamoxifen at one-month of age and the retinas were harvested and analyzed at three-months of age. When comparing BC4s targeted with *CreER* (Figure 4.7 I-J), significant increases in dendrite area, dendrite overlap, and cones contacted were detected (Figure 4.7 K-M). No significant differences in retina area were detected (Figure 4.7 N). Taken together, these data demonstrate that DSCAM is required to inhibit BC plasticity in the mature retina by enforcing tiling.

DISSCUSSION

In this study, we identify and describe the extents and limits of neuron plasticity in retinal bipolar cells, the sole excitatory connection between photoreceptors and downstream retinal circuitry. First we find that BC4s, the focus of the study, retain the ability to extend and refine components of their dendritic arbor within a defined tiled territory over an extended period in the adult mouse retina. Next, we identify *Dscam* as a gene that enforces BC axonal and dendritic tiling, thereby inhibiting further BC plasticity. We also find that this activity is mediated through homotypic DSCAM:DSCAM interactions. We confirmed that novel contacts are physiologically active. Finally, we find that BC dendrite and axon outgrowth can be triggered by targeting *Dscam* deletion in the mature retina. This work therefore identifies cell adhesion molecule (CAM)-mediated inhibition of axon and dendrite outgrowth as a novel target to trigger neurite outgrowth and synaptogenesis.

There are a number of known factors that limit plasticity in mature CNS neurons. In the spinal cord, the extracellular matrix provides inhibitory cues preventing the sprouting and outgrowth of neurons following damage (Fawcett, 2015). In the retina, restriction of axon outgrowth in mature RGCs is caused in part by the down regulation of factors promoting cytoskeletal dynamics (Steketee et al., 2014). In the brain, the bioavailability of growth factors critical for promoting plasticity during development and for learning and memory is reduced with age (Azeredo et al., 2017, Isaev et al., 2017, Keefe et al., 2017,

Kojima and Mizui, 2017, Wrigley et al., 2017). Here, we find that plasticity in mature retinal bipolar cells is inhibited by *Dscam* and that removing *Dscam* triggers the growth of dendrites and axons and the birth of new connections.

Mechanisms describing how BC dendrites and axons develop have been largely based on studies in ON BCs (Lee et al., 2011, Dunn and Wong, 2012, Dunn et al., 2013, Morgan et al., 2006). Here we demonstrate that OFF BC dendritic arbor and synapse development is significantly different from ON BCs. We find that OFF BCs continue to make connections within their dendritic territories until at least six months of age, whereas ON BCs make the same number of connections in the adult retina as they do around the time of eye-opening (Dunn et al., 2013, Gibson et al., 2013). This could be related to the different synapse types formed by ON and OFF BCs in the mammalian retina, with ON cells making invaginating contacts and OFF cells making flat contacts. We find *Dscam* to be important for the regulation of OFF BC plasticity by acting through the homotypic recognition and inhibition of axon and dendrite outgrowth.

The tiled organization of dendritic and axonal within BC types suggest that similar mechanisms exist for all of the BC types to prevent overlap between neighboring neurons. In this study, we identify *Dscam* as the regulator of tiling in non-selective OFF BCs (BC2s, BC3as, BC3bs, BC4s), the OFF populations that make nonselective contacts with both blue and green cones, while previous work points to the closely related *Dscaml1* as the regulator of tiling in rod BCs (Fuerst et al., 2009). Other cell adhesion molecules that regulate neuron self-organization in the retina include the MEGF proteins and g-protocadherin complex (Kay et al., 2012, Lefebvre et al., 2012, Kostadinov and Sanes, 2015). While the limited expression pattern of MEGF proteins suggest that they do not provide self-identify to these populations these works establish cell adhesion molecules as likely candidates for this activity. The identity of molecules providing this recognition in the other ON BCs and BC1s remains an open question as does the extent to which *Dscam* restricts plasticity in other parts of the CNS. *Dscam* is widely expressed throughout the CNS (de Andrade et al., 2014b, de Andrade et al., 2014a, Li et al., 2015, Fernandes et al., 2016, Bruce et al., 2017) and only a subset of functions described in the retina, such as regulation of developmental cell death, laminar targeting and avoidance, have been identified in the rest of the brain. The extent to which *Dscam* limits plasticity in the non-retina portion of the CNS will be important to understand how those cell types regulate their dendritic and axonal arbors.

REFERENCES

AZEREDO, L. A., DE NARDI, T., LEVANDOWSKI, M. L., TRACTENBERG, S. G., KOMMERS-MOLINA, J., WIECK, A., IRIGARAY, T. Q., SILVA, I. G. F. & GRASSI-OLIVEIRA, R. 2017. The brain-derived neurotrophic factor (BDNF) gene Val66Met polymorphism affects memory performance in older adults. *Rev Bras Psiquiatr***,** 0.

BORGHUIS, B. G., LOOGER, L. L., TOMITA, S. & DEMB, J. B. 2014. Kainate receptors mediate signaling in both transient and sustained OFF bipolar cell pathways in mouse retina. *J Neurosci,* 34**,** 6128-39.

BOYCOTT, B. B. & HOPKINS, J. M. 1991. Cone bipolar cells and cone synapses in the primate retina. *Vis Neurosci,* 7**,** 49-60.

BRUCE, F. M., BROWN, S., SMITH, J. N., FUERST, P. G. & ERSKINE, L. 2017. DSCAM promotes axon fasciculation and growth in the developing optic pathway. *Proc Natl Acad Sci U S A,* 114**,** 1702-1707.

CARTER-DAWSON, L. D. & LAVAIL, M. M. 1979. Rods and cones in the mouse retina. I. Structural analysis using light and electron microscopy. *J Comp Neurol,* 188**,** 245-62.

DE ANDRADE, G. B., KUNZELMAN, L., MERRILL, M. M. & FUERST, P. G. 2014a. Developmentally dynamic colocalization patterns of DSCAM with adhesion and synaptic proteins in the mouse retina. *Mol Vis,* 20**,** 1422-33.

DE ANDRADE, G. B., LONG, S. S., FLEMING, H., LI, W. & FUERST, P. G. 2014b. DSCAM localization and function at the mouse cone synapse. *J Comp Neurol,* 522**,** 2609-33.

DE LUCA, C. & PAPA, M. 2016. Looking Inside the Matrix: Perineuronal Nets in Plasticity, Maladaptive Plasticity and Neurological Disorders. *Neurochem Res,* 41**,** 1507-15.

DUNN, F. A., DELLA SANTINA, L., PARKER, E. D. & WONG, R. O. 2013. Sensory experience shapes the development of the visual system's first synapse. *Neuron,* 80**,** 1159-66.

DUNN, F. A. & WONG, R. O. 2012. Diverse strategies engaged in establishing stereotypic wiring patterns among neurons sharing a common input at the visual system's first synapse. *J Neurosci,* 32**,** 10306-17.

EULER, T., HAVERKAMP, S., SCHUBERT, T. & BADEN, T. 2014. Retinal bipolar cells: elementary building blocks of vision. *Nat Rev Neurosci,* 15**,** 507-19.

FAWCETT, J. W. 2015. The extracellular matrix in plasticity and regeneration after CNS injury and neurodegenerative disease. *Prog Brain Res,* 218**,** 213-26.

FERNANDES, K. A., BLOOMSBURG, S. J., MILLER, C. J., BILLINGSLEA, S. A., MERRILL, M. M., BURGESS, R. W., LIBBY, R. T. & FUERST, P. G. 2016. Novel axon projection after stress and degeneration in the Dscam mutant retina. *Mol Cell Neurosci,* 71**,** 1-12.

FERNANDEZ-HERNANDEZ, I. & RHINER, C. 2015. New neurons for injured brains? The emergence of new genetic model organisms to study brain regeneration. *Neurosci Biobehav Rev,* 56**,** 62-72.

FUERST, P. G., BRUCE, F., ROUNDS, R. P., ERSKINE, L. & BURGESS, R. W. 2012. Cell autonomy of DSCAM function in retinal development. *Dev Biol,* 361**,** 326-37.

FUERST, P. G., BRUCE, F., TIAN, M., WEI, W., ELSTROTT, J., FELLER, M. B., ERSKINE, L., SINGER, J. H. & BURGESS, R. W. 2009. DSCAM and DSCAML1 function in self-avoidance in multiple cell types in the developing mouse retina. *Neuron,* 64**,** 484-97.

FUERST, P. G., KOIZUMI, A., MASLAND, R. H. & BURGESS, R. W. 2008. Neurite arborization and mosaic spacing in the mouse retina require DSCAM. *Nature,* 451**,** 470-4.

GIBSON, R., FLETCHER, E. L., VINGRYS, A. J., ZHU, Y., VESSEY, K. A. & KALLONIATIS, M. 2013. Functional and neurochemical development in the normal and degenerating mouse retina. *J Comp Neurol,* 521**,** 1251-67.

HAVERKAMP, S., SPECHT, D., MAJUMDAR, S., ZAIDI, N. F., BRANDSTATTER, J. H., WASCO, W., WASSLE, H. & TOM DIECK, S. 2008. Type 4 OFF cone bipolar cells of the mouse retina express calsenilin and contact cones as well as rods. *J Comp Neurol,* 507**,** 1087-101.

HOPKINS, J. M. & BOYCOTT, B. B. 1992. Synaptic contacts of a two-cone flat bipolar cell in a primate retina. *Vis Neurosci,* 8**,** 379-84.

ICHINOSE, T. & HELLMER, C. B. 2016. Differential signalling and glutamate receptor compositions in the OFF bipolar cell types in the mouse retina. *J Physiol,* 594**,** 883-94.

ISAEV, N. K., STELMASHOOK, E. V. & GENRIKHS, E. E. 2017. Role of Nerve Growth Factor in Plasticity of Forebrain Cholinergic Neurons. *Biochemistry (Mosc),* 82**,** 291-300.

KAY, J. N., CHU, M. W. & SANES, J. R. 2012. MEGF10 and MEGF11 mediate homotypic interactions required for mosaic spacing of retinal neurons. *Nature,* 483**,** 465-9.

KEEFE, K. M., SHEIKH, I. S. & SMITH, G. M. 2017. Targeting Neurotrophins to Specific Populations of Neurons: NGF, BDNF, and NT-3 and Their Relevance for Treatment of Spinal Cord Injury. *Int J Mol Sci,* 18.

KEELEY, P. W., SLIFF, B., LEE, S. C., FUERST, P. G., BURGESS, R. W., EGLEN, S. J. & REESE, B. E. 2011. Neuronal clustering and fasciculation phenotype in dscam- and bax-deficient mouse retinas. *J Comp Neurol*.

KOJIMA, M. & MIZUI, T. 2017. BDNF Propeptide: A Novel Modulator of Synaptic Plasticity. *Vitam Horm,* 104**,** 19-28.

KOSTADINOV, D. & SANES, J. R. 2015. Protocadherin-dependent dendritic self-avoidance regulates neural connectivity and circuit function. *Elife,* 4.

LEE, S. C., COWGILL, E. J., AL-NABULSI, A., QUINN, E. J., EVANS, S. M. & REESE, B. E. 2011. Homotypic regulation of neuronal morphology and connectivity in the mouse retina. *J Neurosci,* 31**,** 14126-33.

LEFEBVRE, J. L., KOSTADINOV, D., CHEN, W. V., MANIATIS, T. & SANES, J. R. 2012. Protocadherins mediate dendritic self-avoidance in the mammalian nervous system. *Nature,* 488**,** 517-21.

LEVIN, S. G. & GODUKHIN, O. V. 2017. Modulating Effect of Cytokines on Mechanisms of Synaptic Plasticity in the Brain. *Biochemistry (Mosc),* 82**,** 264-274.

LI, S., SUKEENA, J. M., SIMMONS, A. B., HANSEN, E. J., NUHN, R. E., SAMUELS, I. S. & FUERST, P. G. 2015. DSCAM Promotes Refinement in the Mouse Retina through Cell Death and Restriction of Exploring Dendrites. *J Neurosci,* 35**,** 5640-54.

LINDSTROM, S. H., RYAN, D. G., SHI, J. & DEVRIES, S. H. 2014. Kainate receptor subunit diversity underlying response diversity in retinal off bipolar cells. *J Physiol,* 592**,** 1457-77.

LONGAIR, M. H., BAKER, D. A. & ARMSTRONG, J. D. 2011. Simple Neurite Tracer: open source software for reconstruction, visualization and analysis of neuronal processes. *Bioinformatics,* 27**,** 2453-4.

LU, Q., IVANOVA, E., GANJAWALA, T. H. & PAN, Z. H. 2013. Cre-mediated recombination efficiency and transgene expression patterns of three retinal bipolar cell-expressing Cre transgenic mouse lines. *Mol Vis,* 19**,** 1310-20.

LU, Q., IVANOVA, E. & PAN, Z. H. 2009. Characterization of green fluorescent protein-expressing retinal cone bipolar cells in a 5-hydroxytryptamine receptor 2a transgenic mouse line. *Neuroscience,* 163**,** 662-8.

MADISEN, L., ZWINGMAN, T. A., SUNKIN, S. M., OH, S. W., ZARIWALA, H. A., GU, H., NG, L. L., PALMITER, R. D., HAWRYLYCZ, M. J., JONES, A. R., LEIN, E. S. & ZENG, H. 2010. A robust and high-throughput Cre reporting and characterization system for the whole mouse brain. *Nat Neurosci,* 13**,** 133-40.

MASLAND, R. H. 1986. The functional architecture of the retina. *Sci Am,* 255**,** 102-11.

MATARUGA, A., KREMMER, E. & MULLER, F. 2007. Type 3a and type 3b OFF cone bipolar cells provide for the alternative rod pathway in the mouse retina. *J Comp Neurol,* 502**,** 1123-37.

MILLER, R. F. & DACHEUX, R. F. 1976. Synaptic organization and ionic basis of on and off channels in mudpuppy retina. I. Intracellular analysis of chloride-sensitive electrogenic properties of receptors, horizontal cells, bipolar cells, and amacrine cells. *J Gen Physiol,* 67**,** 639-59.

MORGAN, J. L., DHINGRA, A., VARDI, N. & WONG, R. O. 2006. Axons and dendrites originate from neuroepithelial-like processes of retinal bipolar cells. *Nat Neurosci,* 9**,** 85-92.

PULLER, C., IVANOVA, E., EULER, T., HAVERKAMP, S. & SCHUBERT, T. 2013. OFF bipolar cells express distinct types of dendritic glutamate receptors in the mouse retina. *Neuroscience,* 243**,** 136-48.

RODIECK, R. W. 1991. The density recovery profile: a method for the analysis of points in the plane applicable to retinal studies. *Vis Neurosci,* 6**,** 95-111.

RODRIGUEZ, J. J. & VERKHRATSKY, A. 2011. Neurogenesis in Alzheimer's disease. *J Anat,* 219**,** 78-89.

SCHILLER, P. H., SANDELL, J. H. & MAUNSELL, J. H. 1986. Functions of the ON and OFF channels of the visual system. *Nature,* 322**,** 824-5.

SCHMIDT, A. & MINNERUP, J. 2016. Promoting recovery from ischemic stroke. *Expert Rev Neurother,* 16**,** 173-86.

SIMMONS, A. B., BLOOMSBURG, S. J., BILLINGSLEA, S. A., MERRILL, M. M., LI, S., THOMAS, M. W. & FUERST, P. G. 2016a. Pou4f2 knock-in Cre mouse: A multifaceted genetic tool for vision researchers. *Mol Vis,* 22**,** 705-17.

SIMMONS, A. B., MERRILL, M. M., REED, J. C., DEANS, M. R., EDWARDS, M. M. & FUERST, P. G. 2016b. Defective Angiogenesis and Intraretinal Bleeding in Mouse Models With Disrupted Inner Retinal Lamination. *Invest Ophthalmol Vis Sci,* 57**,** 1563-77.

SLAUGHTER, M. M. & MILLER, R. F. 1981. 2-amino-4-phosphonobutyric acid: a new pharmacological tool for retina research. *Science,* 211**,** 182-5.

STEKETEE, M. B., OBOUDIYAT, C., DANEMAN, R., TRAKHTENBERG, E., LAMOUREUX, P., WEINSTEIN, J. E., HEIDEMANN, S., BARRES, B. A. & GOLDBERG, J. L. 2014. Regulation of intrinsic axon growth ability at retinal ganglion cell growth cones. *Invest Ophthalmol Vis Sci,* 55**,** 4369-77.

SUN, F., PARK, K. K., BELIN, S., WANG, D., LU, T., CHEN, G., ZHANG, K., YEUNG, C., FENG, G., YANKNER, B. A. & HE, Z. 2011. Sustained axon regeneration induced by co-deletion of PTEN and SOCS3. *Nature,* 480**,** 372-5.

TAY, T. L., SAVAGE, J. C., HUI, C. W., BISHT, K. & TREMBLAY, M. E. 2017. Microglia across the lifespan: from origin to function in brain development, plasticity and cognition. *J Physiol,* 595**,** 1929-1945.

THAKURELA, S., SAHU, S. K., GARDING, A. & TIWARI, V. K. 2015. Dynamics and function of distal regulatory elements during neurogenesis and neuroplasticity. *Genome Res,* 25**,** 1309-24.

TSUKAMOTO, Y. & OMI, N. 2014. Some OFF bipolar cell types make contact with both rods and cones in macaque and mouse retinas. *Front Neuroanat,* 8**,** 105.

VENTURA, A., KIRSCH, D. G., MCLAUGHLIN, M. E., TUVESON, D. A., GRIMM, J., LINTAULT, L., NEWMAN, J., RECZEK, E. E., WEISSLEDER, R. & JACKS, T. 2007. Restoration of p53 function leads to tumour regression in vivo. *Nature,* 445**,** 661-5.

WASSLE, H., BOYCOTT, B. B. & PEICHL, L. 1978. Receptor contacts of horizontal cells in the retina of the domestic cat. *Proc R Soc Lond B Biol Sci,* 203**,** 247-67.

WASSLE, H., PULLER, C., MULLER, F. & HAVERKAMP, S. 2009. Cone contacts, mosaics, and territories of bipolar cells in the mouse retina. *J Neurosci,* 29**,** 106-17.

WRIGLEY, S., ARAFA, D. & TROPEA, D. 2017. Insulin-Like Growth Factor 1: At the Crossroads of Brain Development and Aging. *Front Cell Neurosci,* 11**,** 14.

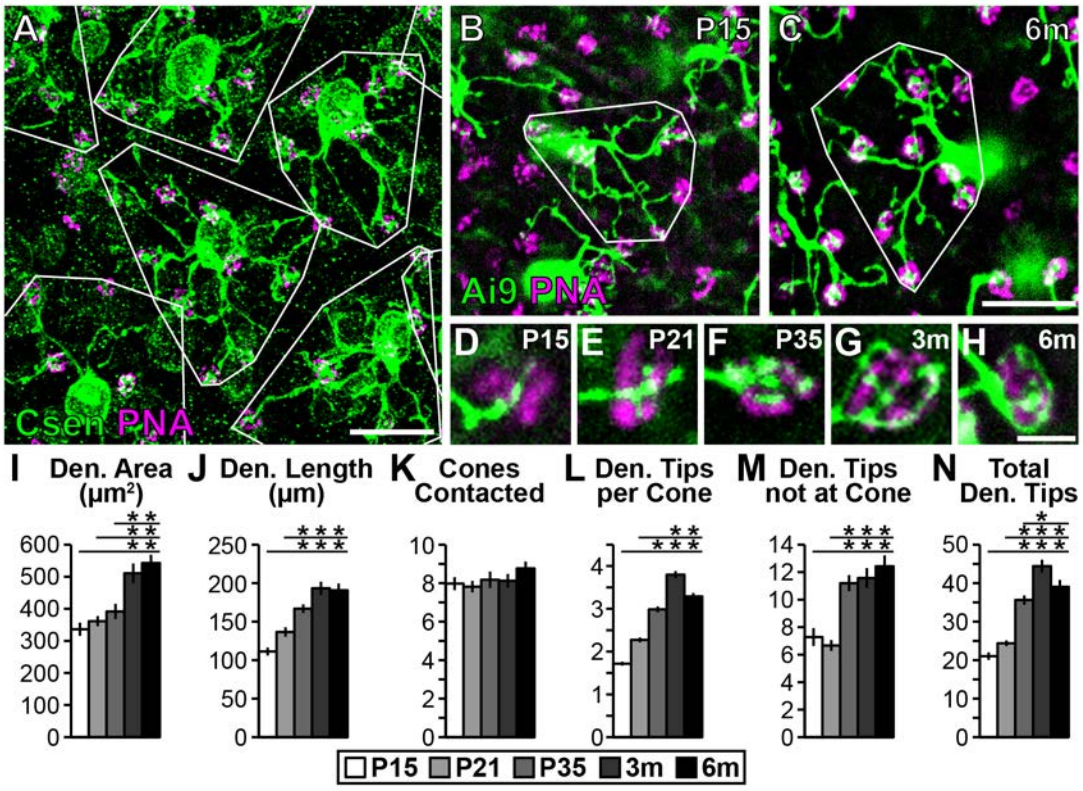

Figure 4.1. BC4s elaborate their dendritic arbors into adulthood. (A) Three-month whole-mount retina stained with anti-calsenilin antibody and PNA to visualize BC4s and cone photoreceptors, respectively. Dendrite areas outlined in white to visualize tiling. (B-C) BC4s labeled genetically (*HTR:Cre x Ai9*) at P15 (B) and 6m (C). Dendrite arbors occupy more area and elaborate their arbors throughout development and into adulthood. (D-H) High magnification images of BC4s connections with cones from P15 to 6m. BC4s elaborate their innervation of cones over-time until they become almost paddle shaped. (I-N) Quantification of BC4 characteristics at P15, P21, P35, 3m, and 6m. Significant increasing trends in all measurements except in cones contacted was detected. Data presented is also found in Figures 4.2, 4.3, 4.S2 and 4.S3. Scale bars in A and C = 25µm, H = 5µm. Abbreviations: Csen, calsenilin; PNA, Peanut Agglutinin; P, post-natal day; m, month; Den., dendrite.

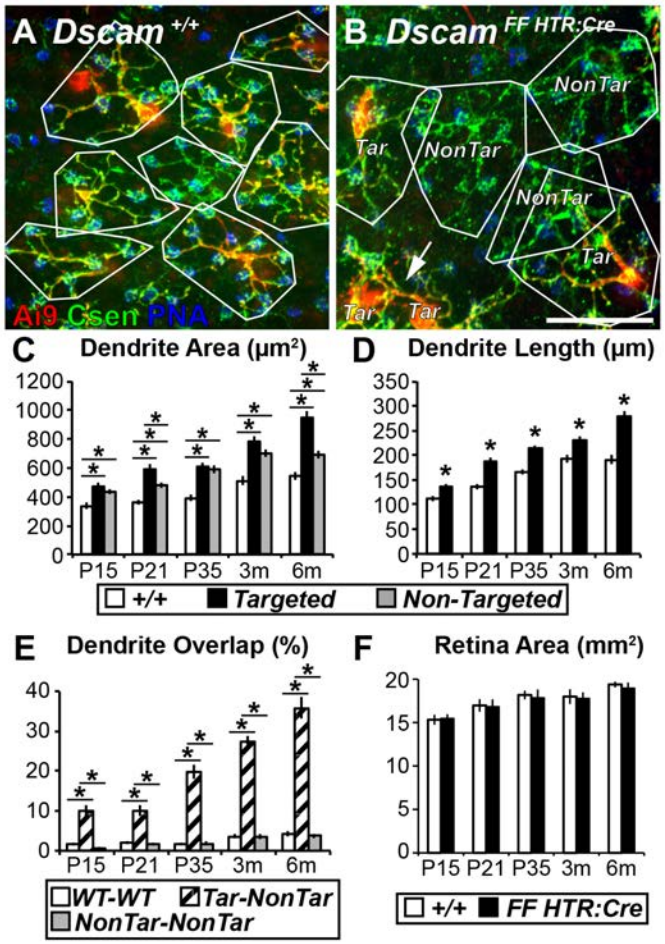

Figure 4.2. *Dscam* is necessary and sufficient to establish and maintain BC4 dendritic tiling. (A-B) Three-month whole-mount retinas where BC4s are labeled genetically (*HTR:Cre x Ai9*), cones are stained with PNA, and anti-calsenilin antibody to label all BC4s. Dendrite areas outlined in white. (A) $Dscam^{+/+}$ retina, BC4 dendrite arbors tile. (B) $Dscam^{FF\ HTR:Cre}$ retina, BC4s invade each others territory when $Dscam^{Tar}$ BC4s neighbor each other (arrow) and when a $Dscam^{Tar}$ BC4 neighbors a $Dscam^{NonTar}$ BC4. However, when $Dscam^{NonTar}$ BC4s neighbor each other, tiling remains intact. (C) Quantification of BC4 dendrite area. Significant increases in dendrite area were detected in $Dscam^{Tar}$ and $Dscam^{NonTar}$ BC4s compared to $Dscam^{+/+}$ BC4s. (D) Quantification of dendrite length. $Dscam^{Tar}$ BC4s have significantly more dendrites than $Dscam^{+/+}$ BC4s. (E) Quantification of dendrite overlap. Significant increases in dendrite overlap were detected in $Dscam^{Tar}$- $Dscam^{NonTar}$ BC4 pairs compared to $Dscam^{+/+}$ and $Dscam^{NonTar}$ pairs. (F) Quantification of total retina area. No significant differences were detected when comparing $Dscam^{+/+}$ and $Dscam^{FF\ HTR:Cre}$ retinas at any time-point. $Dscam^{+/+}$ data is also presented in Figures 4.1 and 4.S2. Image in panel A is also used in Figure 4.S2. Scale bar = 25µm.

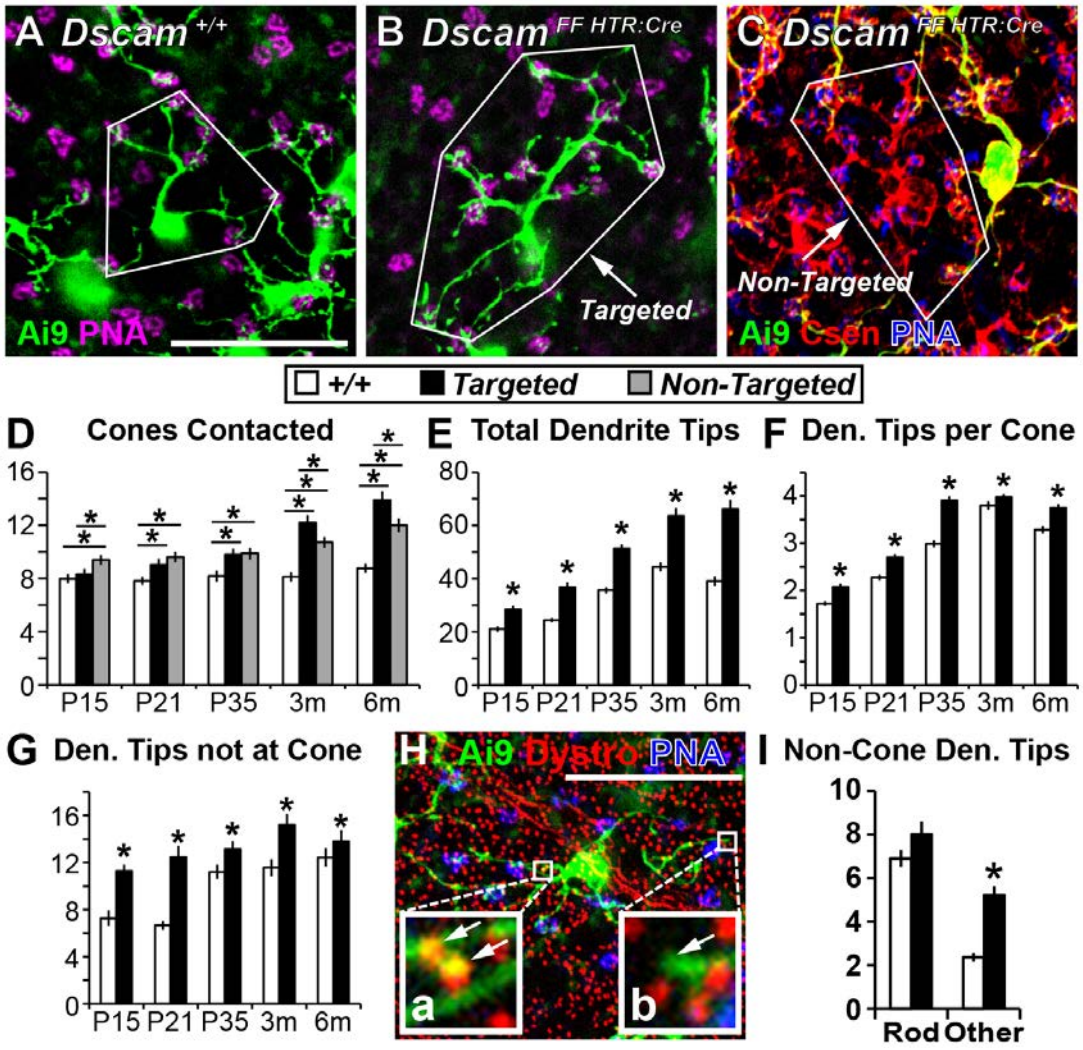

Figure 4.3. BC4s lacking *Dscam* inhibition project more dendrites and connect to more photoreceptors. (A-C) Three-month whole-mount retinas where BC4s are labeled genetically (*HTR:Cre x Ai9*) and cones are stained with PNA. (A) $Dscam^{+/+}$ BC4. (B) $Dscam^{Tar}$ BC4 in $Dscam^{FF\ HTR:Cre}$ retina. (C) $Dscam^{NonTar}$ BC4 in $Dscam^{FF\ HTR:Cre}$ retina. $Dscam^{NonTar}$ BC4s are calsenilin positive, Ai9 negative because they have not been targeted by *HTR:Cre*, and are therefore still expressing *Dscam*. (D) Quantification of cones contacted by BC4s. $Dscam^{Tar}$ and $Dscam^{NonTar}$ BC4s contact significantly more cones compared to $Dscam^{+/+}$ BC4s and they continued to contact more cones over-time. (E-G) Quantification of BC4 dendrite tips. $Dscam^{Tar}$ BC4s have statistically more dendrite tips (E), tips per cone (F), and tips not at cones (G), compared to $Dscam^{+/+}$ BC4s. (H) At P35, retinas were stained with markers to both rods (dystroglycan) and cones (PNA). (I) $Dscam^{+/+}$ and $Dscam^{Tar}$ BC4s contacted similar numbers of rods, while $Dscam^{Tar}$ BC4s had

statistically more dendrite tips ending in neither photoreceptors. *Dscam*$^{+/+}$ data in panels D-G is also presented in Figures 4.1 and 4.S3. Image in panel A is also used in Figure 4.S3. Scale bars = 25μm. Abbreviations: Dystro, dystroglycan.

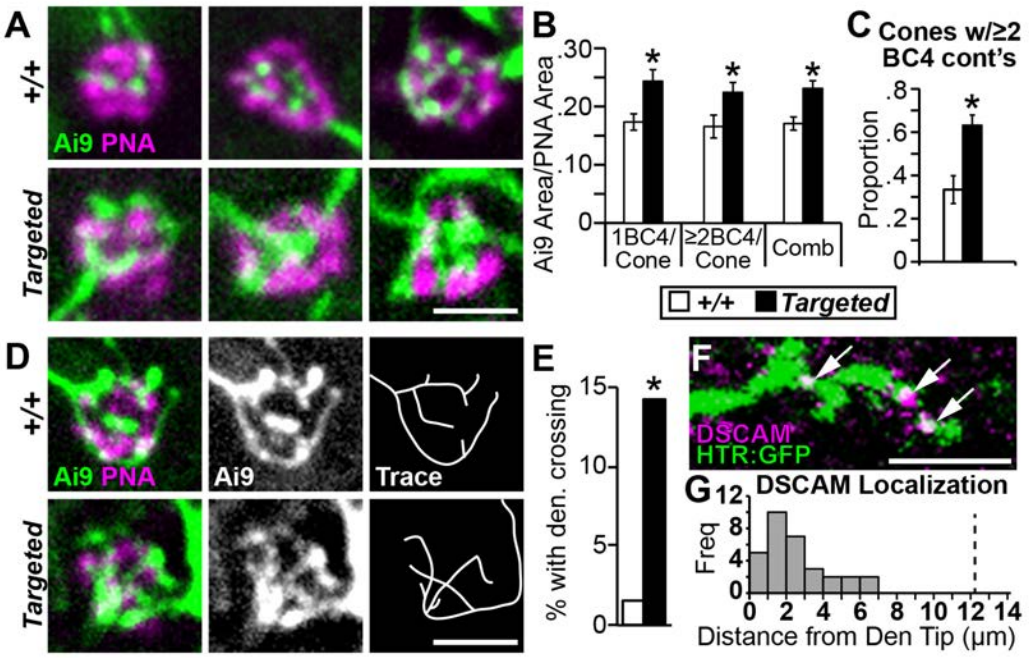

Figure 4.4. *Dscam* is necessary and sufficient for iso-neuronal avoidance at the cone synapse in BC4s. (A) High magnification images of single BC4s making contact with cones at three months of age in whole-mount retinas. *Dscam*$^{+/+}$ BC4s make connections with cones that are highly organized and vary in their amount of contacts at a single cone. *Dscam*^{Tar} BC4s make connections with cones that are disorganized and their dendrites clump together. (B) Quantification of total amount of BC4 dendrites localized within PNA area. Significant increases in coverage were observed in *Dscam*^{Tar} BC4s compared to *Dscam*$^{+/+}$ BC4s, regardless if the cones were contacted by 1BC4 or ≥2BC4s. No significant differences were detected in PNA area (data not shown). (C) Quantification of cones contacted by two or more BC4s. A significant increase was observed in *Dscam*$^{FF\ HTR:Cre}$ compared to *Dscam*$^{+/+}$. (D) High magnification images of single BC4s making contact with cones at three-months of age. *Dscam*$^{+/+}$ BC4s dendrites do not cross. *Dscam*^{Tar} BC4s dendrites frequently cross. (E) Quantification of observed dendrite crossing at the cone. Statistically more dendrites cross in *Dscam*^{Tar} BC4s compared to *Dscam*$^{+/+}$ BC4s. (F) High magnification image of DSCAM co-localization with *Dscam*$^{+/+}$ BC4 dendrites in cryo-sections. Arrows point to co-localization. (G) Quantification of the distance DSCAM puncta is localized from the nearest BC4 dendritic tip. DSCAM was observed as far away as 7µm from the dendrite tip. The vertical dotted line at 12.2µm represents the average dendrite length from dendrite terminal to cell body. Scale bars = 3µm. Abbreviations: comb, combined; cont's, contacts; freq, frequency.

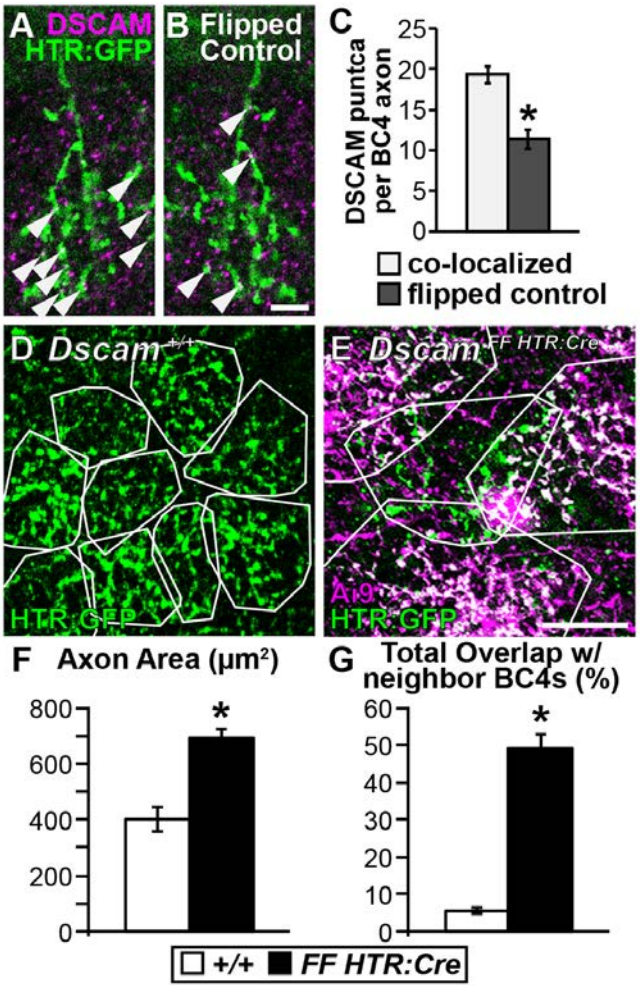

Figure 4.5. *Dscam* is necessary and sufficient to establish and maintain BC4 axon tiling. (A-C) Co-localization of DSCAM protein with BC4 axons. Of note, this analysis was performed in serial z-stack images, shown here is a single confocal plane from an analyzed stack. (A-B) Cryo-sections of retina stained with anti-DSCAM and *HTR:GFP* to determine co-localization. (A) Image showing DSCAM/BC4 axon co-localization. (B) Axon channel flipped about the horizontal axis as a control for incidental co-localization. Arrowheads point to co-localized DSCAM puncta on BC4 axons. (C) Quantification of DSCAM puncta co-localization per BC4 axon. A significant increase in DSCAM puncta was detected when comparing the original images to the flipped controls. (D-E) Three-month flat-mount retina, BC4s are labeled genetically (*HTR:Cre x Ai9* and *HTR:GFP or HTR:GFP* only). (D) $Dscam^{+/+}$, BC4 axons outlined in white to visualize tiling. (E) $Dscam^{FF\ HTR:Cre}$, axons outline in white. Only the green axon is a single axon. The others outlined are multiple BC4 axons bundled together. Green axon is a $Dscam^{NonTar}$ BC4. Axons invade each others territory

when one or both lack DSCAM. (F-G) Quantifications of axon area (F) and total overlap with neighboring BC4 axons (G). *Dscam*^{NonTar} BC4 axons, become significantly larger and overlap significantly more with neighboring *Dscam*^{Tar} BC4 axons when compared to *Dscam*$^{+/+}$ BC4 axons. Scale bar in B = 5μm; E = 20μm.

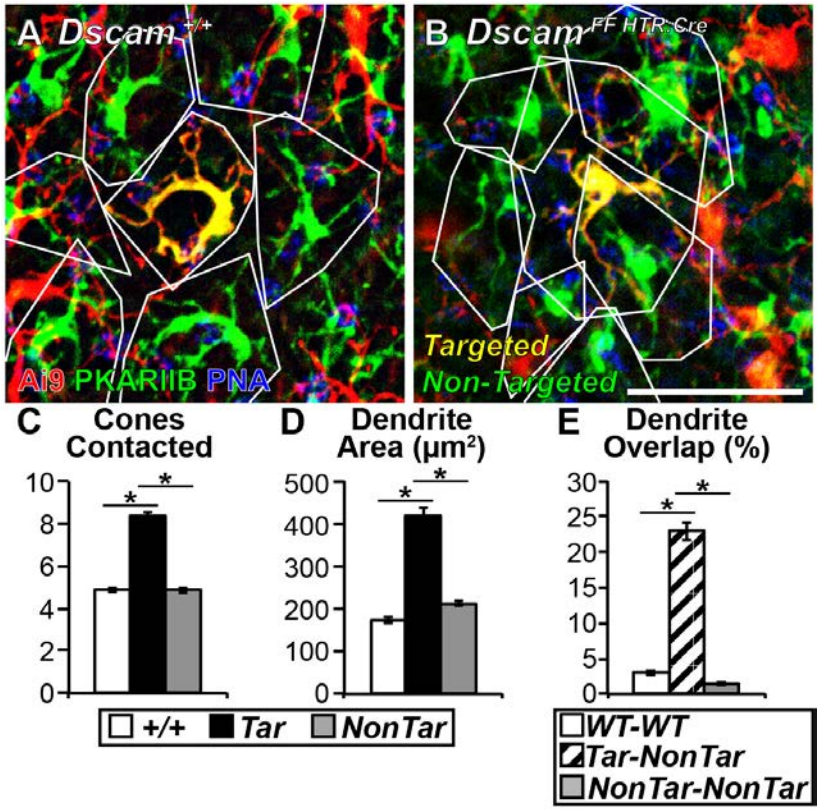

Figure 4.6. *Dscam* is necessary and sufficient to establish and maintain BC3b dendritic tiling. (A-B) One-month flat-mount retinas stained genetically *(HTR:Cre x Ai9)* and counterstained with PKARIIB and PNA. Because *HTR:Cre* targets ~1% of BC3bs (Lu et al., 2013) (data not shown), sparse BC3bs can be labeled genetically while concurrently deleting *Dscam* when the mouse is homozygous for the floxed *Dscam* allele. BC4s can be eliminated from the analysis because they are not PKARIIB-positive. (A) $Dscam^{+/+}$, BC3bs outlined in white to visualize tiling. (B) $Dscam^{FF\ HTR:Cre}$, $Dscam^{Tar}$ BC3bs become significantly larger and loose tiling with neighboring $Dscam^{NonTar}$ BC3bs. (C-E) Quantification of cones contacted (C), dendrite area (D), and dendrite overlap (E). Significant increases in cones contacted and dendrite area were detected when comparing $Dscam^{Tar}$ BC3bs to $Dscam^{+/+}$ or $Dscam^{NonTar}$ BC3bs. Significant increases in dendrite overlap were detected when comparing $Dscam^{Tar}$-$Dscam^{NonTar}$ BC3b pairs to $Dscam^{+/+}$ or $Dscam^{NonTar}$ pairs. Scale bar in B = 20µm. Abbreviations: PKARIIB, Protein Kinase A RII beta.

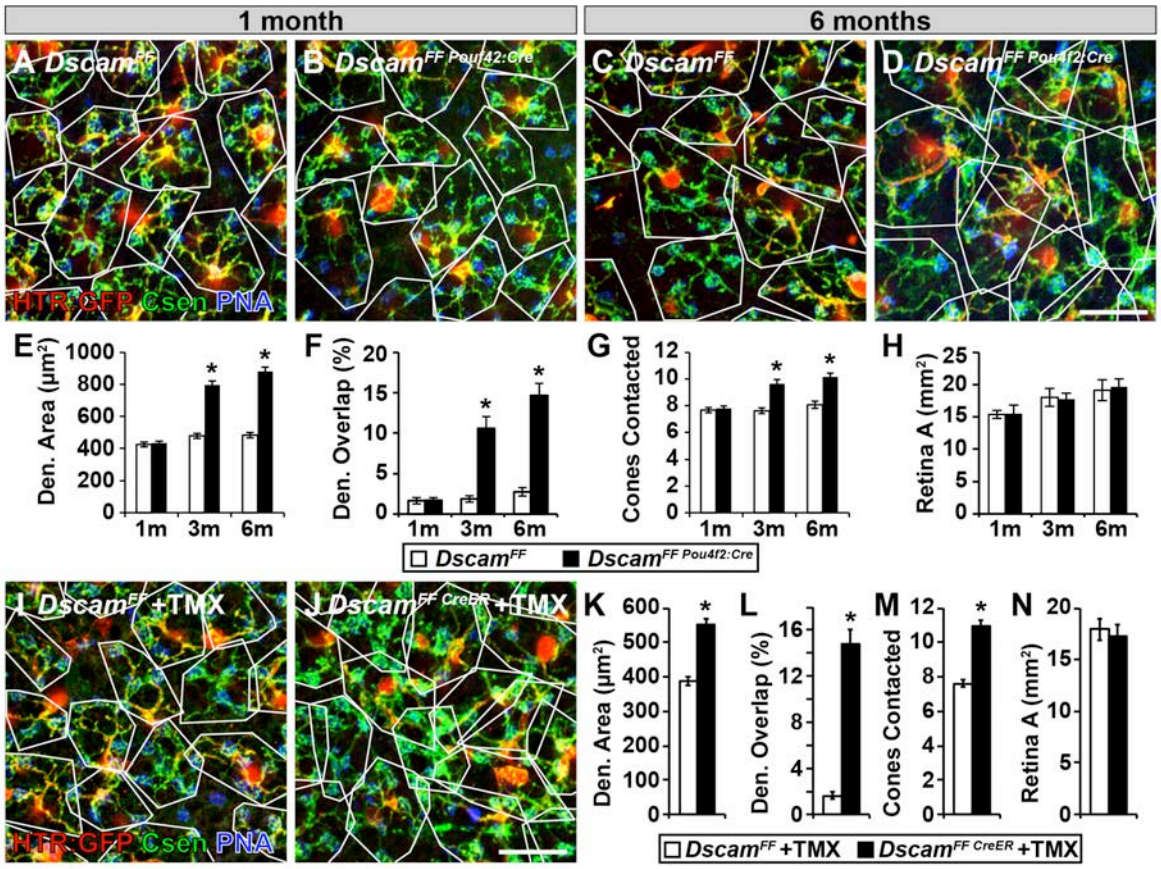

Figure 4.7. *Dscam* is necessary and sufficient to inhibit BC4 dendritic plasticity in the adult retina. Late deletion of the *Dscam* floxed allele was accomplished with *Pou4f2:Cre* (A-H), which effectively recombines *Dscam* by P45 (Simmons et al., 2016a), and with the inducible *CreER* (I-N). *Dscam*^{FF} BC4s were compared to *Dscam*$^{FF\ Pou4f2:Cre}$ BC4s before *Pou4f2:Cre* mediated recombination of *Dscam* occurs, 1m (A-B), and then compared at two more time-points after recombination occurs, 3m and 6m (C-D). (A-D) Whole-mount retinas with BC4s labeled with *HTR:GFP* and stained with PNA and calsenilin. Dendrite areas mapped in white. (E-H) Quantifications of dendrite area (E), dendrite overlap (F), and cones contacted (G). *Dscam*^{FF} BC4s and *Dscam*$^{FF\ Pou4f2:Cre}$ BC4s are not statistically different for any of these measures at 1m of age. However, *Dscam*$^{FF\ Pou4f2:Cre}$ BC4s become statistically greater for all of these measurements at 3m and 6m. (H) Quantification of total retina area. No statistical differences were observed between *Dscam*^{FF} and *Dscam*$^{FF\ Pou4f2}$ retinas. (I-J) *Dscam*^{FF} and *Dscam*$^{FF\ CreER}$ mice were injected with tamoxifen at 1m and retinas were collected at 3m. (K-N) Quantifications of dendrite area (K), dendrite overlap (L), cones contacted (M). *Dscam*$^{FF\ CreER}$ BC4s are statically larger for all of these measurements. (N) Quantification of total retina area. No statistical differences observed between *Dscam*^{FF} and *Dscam*$^{FF\ CreER}$ retinas. Scale bars = 20µm.

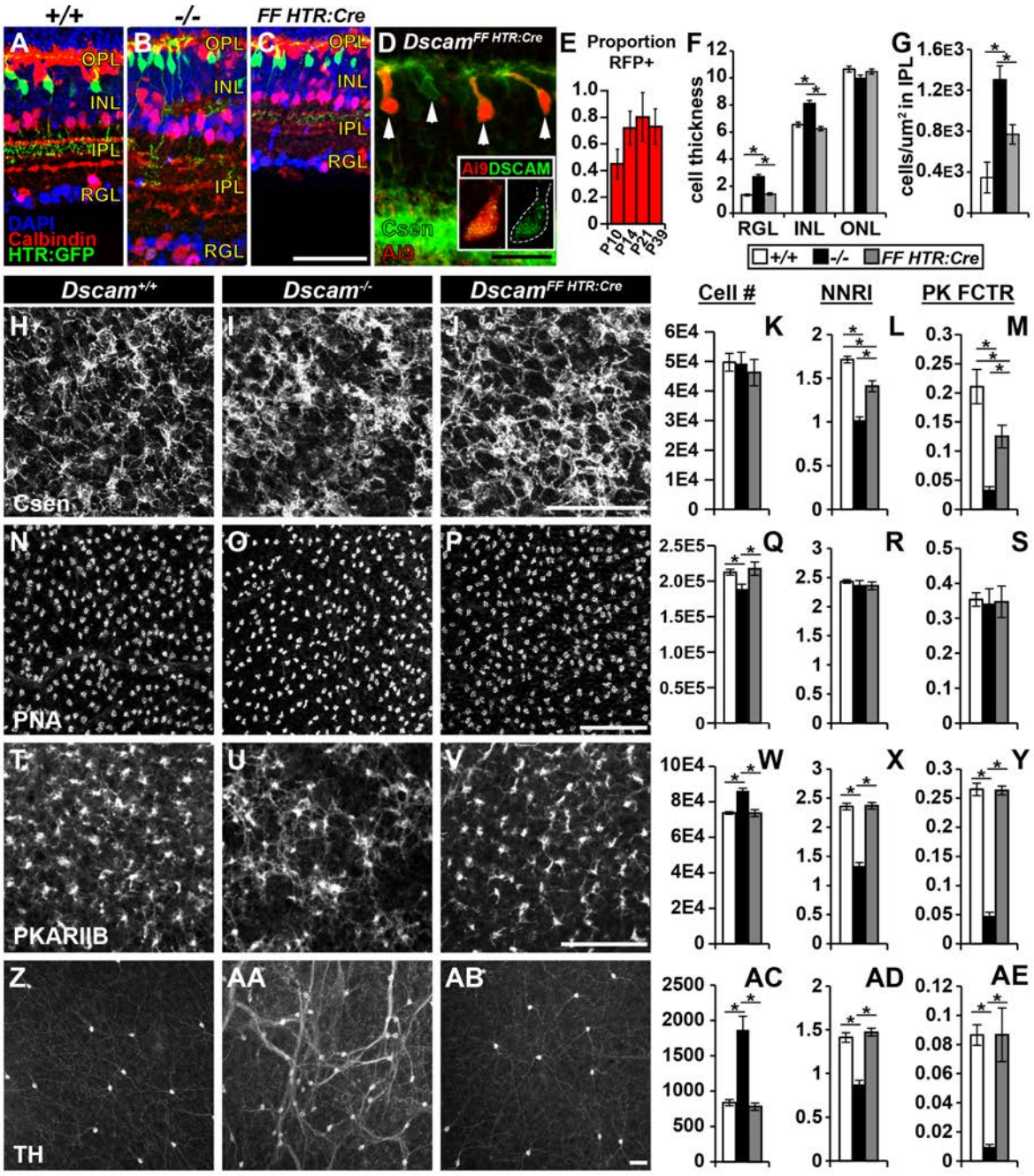

Figure 4.S1. Conditional targeting of *Dscam* with *HTR:Cre*. (A-C) Cryo-sections of retina stained with DAPI, calbindin and *HTR:GFP*. (A) *Dscam*$^{+/+}$ retina, organization of the retina in to alternating nuclear and synaptic layers. Lamination of the IPL is organized into sublamina, illustrated by calbindin staining and lamination of BC4 axons. (B) *Dscam*$^{-/-}$ retina, highly disorganized retinal layers due to defects in neural organization and cell death. (C) *Dscam*$^{FF\ HTR:Cre}$ retina, integrity of the retinal layers and lamination of the IPL is maintained.

(D-E) *HTR:Cre* targeting efficiency of the *Ai9* reporter and *Dscam* floxed alleles. By P14, *HTR:Cre* targets ~75% of BC4s, evidenced by *Ai9* expression and accumulation of DSCAM protein in the cytosol after the transmembrane domain is removed by cre-mediated recombination. (F) Quantification of retinal thickness in each nuclear layer. (G) Quantification of displaced cells in the IPL. Significant increases in cellularity is observed in the $Dscam^{-/-}$ retina compared to $Dscam^{+/+}$ or $Dscam^{FF\ HTR:Cre}$ retinas. (H-AE) Cell number, NNRI and Packing factors were quantified and compared in whole-mount retinas at 1m of age in $Dscam^{+/+}$, $Dscam^{-/-}$, and $Dscam^{FF\ HTR:Cre}$ retinas for multiple cell types known to require DSCAM for proper cell death and/or dendrite arborization. Cones do not require DSCAM, but were included in the analysis because they are the main presynaptic input for BC4s. (H-M) BC4s, no significant changes in cell number were detected. Significant reductions in both the NNRI and packing factor were detected when comparing $Dscam^{+/+}$ to $Dscam^{-/-}$ and $Dscam^{FF\ HTR:Cre}$, and when comparing $Dscam^{-/-}$ to $Dscam^{FF\ HTR:Cre}$. (N-S) Cones, a significant reduction in cones was detected when comparing $Dscam^{-/-}$ to $Dscam^{+/+}$ or $Dscam^{FF\ HTR:Cre}$ retinas. No significant changes to NNRI or packing factor were detected. (T-Y) BC3bs, significant increases in cell number was detected when comparing $Dscam^{-/-}$ to $Dscam^{+/+}$ or $Dscam^{FF\ HTR:Cre}$ retinas. Significant reductions in NNRI and packing factor were detected when comparing $Dscam^{-/-}$ to $Dscam^{+/+}$ or $Dscam^{FF\ HTR:Cre}$ retinas. (Z-AE) DACs, significant increases in cell number was detected when comparing $Dscam^{-/-}$ to $Dscam^{+/+}$ or $Dscam^{FF\ HTR:Cre}$ retinas. Significant reductions in NNRI and packing factor were detected when comparing $Dscam^{-/-}$ to $Dscam^{+/+}$ or $Dscam^{FF\ HTR:Cre}$ retinas. Scale bars = 50μm. Abbreviations: ONL, outer nuclear layer; OPL, outer plexiform layer; INL, inner nuclear layer; IPL, inner plexiform layer; RGL, retinal ganglion cell layer; RFP, red fluorescent protein; NNRI, nearest neighbor regularity index; PK FCTR, packing factor.

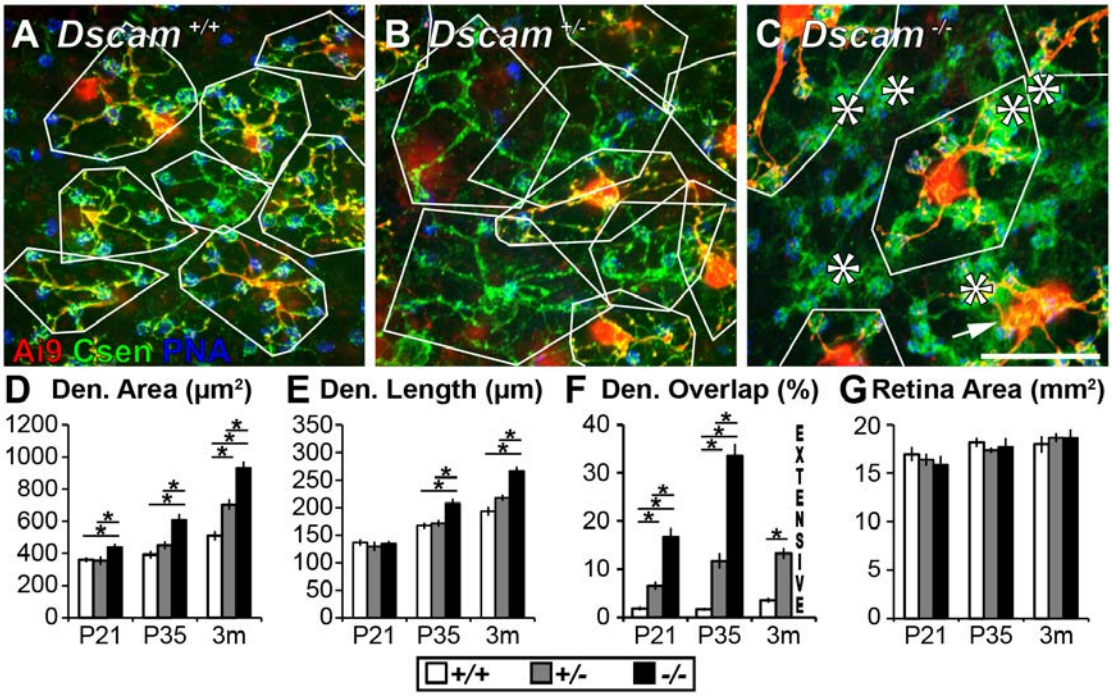

Figure 4.S2. *Dscam* dosage affects BC4 dendritic tiling. To test how *Dscam* dosage influenced BC4 dendritic tiling and gross morphology, these characteristics were measured at P21, P35 and 3m in *Dscam*$^{+/+}$, *Dscam*$^{+/-}$, and *Dscam*$^{-/-}$ retinas. (A-C) Three-month whole-mount preparations of retina where BC4s are labeled genetically (*HTR:Cre x Ai9*), cones are stained with PNA, and anti-calsenilin antibody to label all BC4s. BC4 dendrite areas are outlined in white. In panel (C), only Ai9(+) BC4s are outlined because dendrite overlap is so extensive that calsenilin(+), Ai9(-) cells cannot be resolved. Asterisks are placed where calsenilin(+), Ai9(-) cell bodies are located. Arrow points to two Ai9(+) cells that are highly tangled with one another. (D-G) Quantifications of dendrite area (D), dendrite length (E), dendrite overlap (F), and retina area (G). By 3m of age, we detected significant increases in dendrite area as *Dscam* dosage decreases. We also detected dosage dependent effects on dendrite overlap at all time-points assessed. At 3m of age, the overlap of BC4 dendrites in the *Dscam*$^{-/-}$ retina was too extensive to quantify with the assay. *Dscam*$^{+/+}$ data and image in panel A are also presented in Figure 4.3. Scale bar = 25µm.

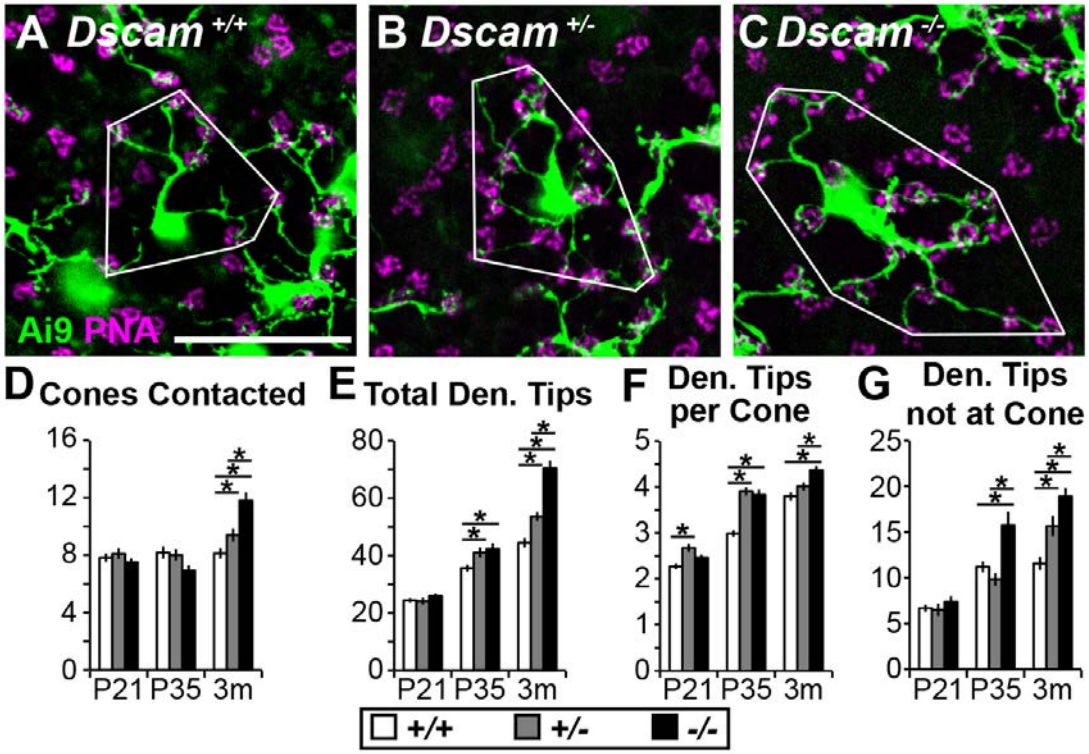

Figure 4.S3. *Dscam* dosage affects BC4 connectivity. To test how *Dscam* dosage influenced connectivity of BC4s, connectivity was compared at P21, P35 and 3m in *Dscam*$^{+/+}$, *Dscam*$^{+/-}$, and *Dscam*$^{-/-}$ retinas. (A-C) Three-month whole-mount retinas where BC4s are labeled genetically (*HTR:Cre x Ai9*) and cones are stained with PNA. (D-G) Quantification of BC4 connectivity, total dendrite tips (D), dendrite tips per cone (E), dendrite tips not at cone (F), and cones contacted (G). By 3m of age, we detected significant increases in total dendrite tips, dendrite tips not at cone and cones contacted as *Dscam* dosage went down. Delays in the development of *Dscam*$^{-/-}$ mice may be contributing abnormally low values are early time-points. *Dscam*$^{+/+}$ data and image in panel A are also presented in Figure 4.2. Scale bar = 25µm.

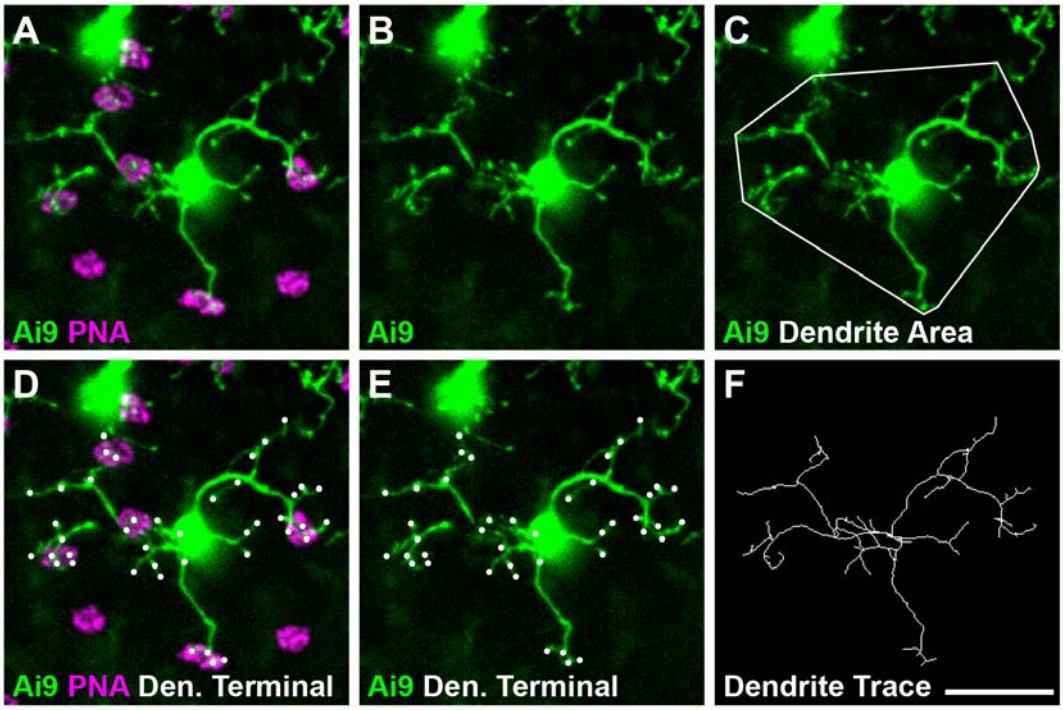

Figure 4.S4. Z-stack images showing how individual BC4 characteristics were measured. All measurements were performed using a series of images that were actively scrolled through. The image series for this cell can be seen in Video S1. (A) Genetically labeled BC4 (*HTR:Cre x Ai9*) in green and cones labeled by PNA in magenta. Cones contacted was quantified by the number of cones the cell came in contact with, this cell contacts 5 cones. (B) Genetically labeled BC4 (*HTR:Cre x Ai9*) in green split out for better visualization. (C) Dendrite area was measured by constructing a convex polygon around the dendrite arbor and measuring the area within that polygon. (D) All dendrite terminals marked with white dots. These terminals were then classified based upon their location into three different categories: total dendrite tips, dendrite tips per cone, and dendrite tips not at cones. (F) Dendrite skeletons were made by manually tracing dendrites of BC4s in the FIJI plug-in, Simple Neurite Tracer (Longair et al., 2011) and the total length of dendrites was measured. Scale bar = 10μm.

Table 4.S1. Table summary of statistics			
Fig	**Measurement**	**Statistical Test**	**p-values [group(p-value)]**
4.1	Den Area	1-way ANOVA	5.0E-10
	Den Length	1-way ANOVA	1.4E-16
	Cones Contacted	1-way ANOVA	0.48
	Den Tips per Cone	1-way ANOVA	1.2E-98
	Den Tips not at Cone	1-way ANOVA	4.5E-12
	Total Den Tips	1-way ANOVA	5.4E-31
4.2	Dendrite Area	1-way ANOVA	P15(4.9E-5), P21(1.0E-10), P35(2.4E-7), 3m(5.1E-8), 6m(2.1E-12)
	Dendrite Length	Student's *t*-test	P15(4.6E-4), P21(7.5E-7), P35(5.3E-7), 3m(9.2E-4), 6m(1.7E-9)
	Dendrite Overlap	1-way ANOVA	P15(5.7E-11), P21(6.8E-13), P35(1.0E-29), 3m(1.8E-48), 6m(1.0E-37)
	Retina Area	Student's *t*-test	P15(0.85), P21(0.90), P35(0.77), 3m(0.85), 6m(0.64)
4.3	Cones Contacted	1-way ANOVA	P15(0.02), P21(2.6E-3), P35(0.01), 3m(1.5E-8), 6m(8.9E-9)
	Total Den Tips	Student's *t*-test	P15(2.9E-5), P21(1.1E-7), P35(5.3E-12), 3m(4.4E-7), 6m(2.3E-8)
	Den Tips per Cone	Student's *t*-test	P15(2.0E-5), P21(2.2E-5), P35(1.1E-13), 3m(1.4E-3), 6m(0.02)
	Den Tips not at Cone	Student's *t*-test	P15(1.3E-5), P21(1.5E-6), P35(0.03), 3m(2.9E-3), 6m(0.03)
	Non-Cone Den Tips	Student's *t*-test	Rod(0.11), other(3.9E-8)
4.4	Ai9 Area/PNA Area	Student's *t*-test	1BC4/cone(4.9E-3), ≥2BC4(0.03), comb(5.4E-4)
	Cones w/≥2BC4 cont	Student's *t*-test	0.01
	% with den crossing	HT (2 indv prop)	0.01
4.5	DSCAM co-localization	Student's *t*-test	1.5E-4
	Axon Area	Student's *t*-test	3.3E-6
	Total Overlap w/nbr BC4s	Student's *t*-test	5.0E-13
4.6	Cones Contacted	1-way ANOVA	7.6E-31
	Dendrite Area	1-way ANOVA	1.1E-28
	Dendrite Overlap	1-way ANOVA	1.7E-65
4.7	Den Area (*Pou4f2*)	Student's *t*-test	1m(0.66), 3m(5.3E-17), 6m(1.5E-19)
	Den Overlap (*Pou4f2*)	Student's *t*-test	1m(0.93), 3m(1.6E-7), 6m(5.2E-11)
	Cones Contacted (*Pou4f2*)	Student's *t*-test	1m(0.62), 3m(1.1E-6), 6m(7.7E-7)
	Retina Area (*Pou4f2*)	Student's *t*-test	1m(0.87), 3m(0.77), 6m(0.68)
	Den Area (*CreER*)	Student's *t*-test	3.06E-9
	Den Overlap (*CreER*)	Student's *t*-test	4.65E-19
	Cones Contacted (*CreER*)	Student's *t*-test	2.90E-11
	Retina Area (*CreER*)	Student's *t*-test	0.69
4.S1	Cellularity	1-way ANOVA	RGL(1.3E-14), INL(7.5E-11), ONL(0.07), cells/μm^2 in IPL(6.5E-5)
	Cell Number	1-way ANOVA	BC4s(0.79), cones(0.03), BC3bs(1.1E-4), DACs(3.5E-5)
	NNRI	1-way ANOVA	BC4s(1.0E-6), cones(0.66), BC3bs(9.2E-8), DACs(2.1E-6)
	Packing Factor	1-way ANOVA	BC4s(2.2E-4), cones(0.98), BC3bs(2.8E-9), DACs(5.3E-4)
4.S2	Dendrite Area	1-way ANOVA	P21(0.01), P35(4.4E-6), 3m(1.1E-12)
	Dendrite Length	1-way ANOVA	P21(0.75), P35(5.6E-5), 3m(4.5E-9)
	Dendrite Overlap	1-way ANOVA	P21(2.0E-16), P35(1.4E-32), 3m(3.6E-12)
	Retina Area	1-way ANOVA	P21(0.63), P35(0.68), 3m(0.75)
4.S3	Cones Contacted	1-way ANOVA	P21(0.42), P35(0.06), 3m(9.1E-7)
	Total Den Tips	1-way ANOVA	P21(0.37), P35(0.01), 3m(1.2E-14)
	Den Tips per Cone	1-way ANOVA	P21(5.3E-4), P35(3.4E-14), 3m(2.8E-5)
	Den Tips not at Cone	1-way ANOVA	P21(0.50), P35(1.9E-4), 3m(9.0E-7)

Table 4.S1. Table summary of statistics. Reported here are the statistical tests and p-values for each measurement performed in the study. If the measurement contained multiple pairings (age, rods v. other, retinal layer, cell type, etc.) the grouping is stated followed by the p-value in parentheses, i.e. P15(p-value). An α=0.05 was used for each statistical analysis. For all one-way ANOVAs, Tukey-Kramer post-hoc tests were used to detect difference among groups. Asterisks in the graphs denote statistical differences.

Chapter 5: *Pou4f2* knock-in Cre mouse: A multifaceted genetic tool for vision researchers

Aaron B. Simmons, Sam A. Billingslea, Morgan M. Merrill, Shuai Li, Marshall Thomas and Peter G. Fuerst

Current Status: Published in *Molecular Vision*

Citation: Simmons, A.B., Bloomsburg S.J., Billingslea S.A., Merrill, M.M., Li, S., Thomas M.W., and Fuerst, P.G. Pou4f2 knock-in Cre mouse: A multifaceted genetic tool for vision researchers. Molecular Vision. 2016 Jun 23;22:705-17. PMID: 27390513.

ABSTRACT

PURPOSE: A transgenic mouse that expresses Cre recombinase under control of the *Pou4f2*-promoter (also referred to as *Brn-3b and Brn-3.2*) was characterized. *Pou4f2* expression has been reported in a subset of retinal ganglion cells (RGCs) in the retina, in the midbrain and in the germ line. In this study we characterize the expression pattern of this Cre-recombinase line and report its utility in targeted deletion, temporal deletion, RGC depletion and germ line targeting, which can be regulated by the sex of the Cre-carrying mouse.

METHODS: *Pou4f2*^{Cre} was mapped by utilizing a combination of polymerase chain reaction (PCR) and sequencing of PCR products to better understand the construct and to locate where it was inserted within the *Pou4f2* locus. Cre expression patterns were examined by crossing *Pou4f2*$^{Cre/+}$ mice to Cre reporter mice. Immunohistochemistry was used to further define the pattern of Cre expression and Cre-mediated recombination within the retina, brain and other tissues.

RESULTS: An IRES-Cre cassette was inserted into the *Pou4f2* gene disrupting normal gene function, as verified by depletion of RGCs in mice homozygous for the insert. *Pou4f2*^{Cre} expression was observed in the retina, brain, peripheral neurons and the male germ cells. Germline recombination was observed when the sire carried both the Cre and the target for recombination. In all other breeding schemes, recombination was observed within subsets of cells within the retina, brain, intestines, heart and gonads. In the retina, Cre efficiently targets recombination in neurons within the retinal ganglion cell layer, inner nuclear layer and a small percentage of photoreceptors, activity that has not been previously reported. Unlike most other Cre lines active in the inner retina, recombination in

Müller and other glia was not observed in mice carrying *Pou4f2*^{Cre}. Within visual centers of the brain, Cre targets recombination in about 15% of cells within the superchiasmatic nucleus, lateral geniculate nucleus and superior colliculus.

CONCLUSIONS: *Pou4f2*^{Cre} provides multiple uses for the vision researcher's genetic toolkit. First, *Pou4f2*^{Cre} is a knock-in allele that can be used to eliminate *Pou4f2*, resulting in depletion of RGCs. Second, expression of Cre in the male germ cells makes this strain an efficient germline activator of recombination, for example to target loxP-flanked sequences in the whole mouse. Third, *Pou4f2*^{Cre} efficiently targets RGCs, amacrine cells, bipolar cells, horizontal cells and a small number of photoreceptors within the retina, as well as visual centers in the brain. Unlike other Cre recombinase lines that target retinal neurons, no recombination is observed in Müller or other retinal glia. These properties make this Cre recombinase line a useful tool for vision researchers.

INTRODUCTION

Targeted manipulation of the genome has greatly improved our understanding of mechanisms responsible for development; however, many such genetic manipulations result in severe abnormalities and high mortality rates. Understanding cell autonomy of defects often also necessitates a more targeted approach than eliminating or over expressing a gene. Cre-lox technology, in which Cre recombinase excises or inverts the sequence flanked by loxP sites, depending on the orientation of the sites, allows for targeted activation or inactivation of DNA sequences [1]. Using this technology has enabled researchers to target specific populations of cells or specific time points. Characterizing and disseminating various Cre transgenic lines allows researchers to refine experiments and ask more informative questions.

In this study we characterize a mouse strain in which Cre recombinase has been inserted into the *Pou4f2* locus (also referred to as *Brn-3b* or *Brn-3.2*), replacing the *Pou4f2* gene. Previous work has shown that the POU domain transcription factor *Pou4f2* is expressed in a large subset of retinal ganglion cells (RGCs) and is essential for RGC differentiation [2-5], survival [6] and axon path-finding [7-9]. The study herein characterizes a *Pou4f2* knock-in Cre recombinase mouse line, *Pou4f2*^{Cre}, which expresses Cre recombinase in a subset of retinal neurons. In addition to targeting genes in the mouse

retina, the *Pou4f2*^{Cre} line can be used to generate mice in which the number of RGCs is depleted, when the transgene is homozygous [2, 3]. When carried by male mice, along with a target allele, the *Pou4f2*^{Cre} efficiently targets recombination in the germline. Therefore, a single mouse strain can be used to target recombination in retinal neurons, to deplete RGCs and to target germline recombination.

MATERIALS AND METHODS

Mouse care and housing*:* All protocols were performed in accordance with the University of Idaho Institutional Animal Care and Use Committee. Mice were fed *ad libitum* under 12-hour light/dark cycle.

Mouse Strains*:* The following mouse strains were used in this study: *Pou4f2*^{Cre} (courtesy of Dr. Vann Bennett; Duke University) [10], Ai9 reporter (The Jackson Laboratory, Bar Harbor, ME; stock number 007909) [11], Brainbow reporter (The Jackson Laboratories stock number 021227) [12] and *Dscam* conditional mutant mice [10]. Mouse strains were maintained on a mixed C57Bl6/J, C3H/HeJ and 129 background. All mice carried the wild type allele of *Pde6b*.

Genotyping: Tissue biopsies (toe tips or tail tips) were taken from mice and then prepared for polymerase chain reaction (PCR) by first boiling the samples in 50 µl 25 µM sodium hydroxide and 0.2 µm EDTA for 15 minutes. 50 µl of Tris Cl (pH 5.0) was then added to the samples, neutralizing them. Each PCR reaction consisted of: 7.5 µl of OneTaq Hot Start Master Mix (2X, New England Biolabs, Ipswich, MA) [13], 0.1 µl primers, 1 µl of DNA sample, and 6.4 µl of nuclease free water; bringing the final volume to 15 µl. The following primers were used when genotyping: *Pou4f2* Forward (#1, Figure 5.1A): GCT GAG GTC TGA AGC CAG AG, *Pou4f2* Reverse (#2, Figure 5.1A): CAG TCA GCT CCT CGC TTT CT. Cre Forward (#3, Figure 5.1B): GCA TTA CCG GTC GAT GCA ACG AGT G, Cre Reverse (#4, Figure 5.1B): GAG TGA ACG AAC CTG GTC GAA ATC A. Neomycin Forward (#6, Figure 5.1B): AGG ATC TCC TGT CAT CTC ACC TTG CTC CTG, Neomycin Reverse (#5, Figure 5.1B): AAG AAC TCG TCA AGA AGG CGA TAG AAG GCG.

Tissue preparation: Mice were anesthetized using tribromoethanol. Anesthetized mice were perfused with phosphate-buffered saline (PBS), pH 7.4. Eyes were then carefully removed using forceps and dissected in PBS to remove the cornea, iris and lens. Eyes

were fixed in 4% paraformaldehyde (PFA) solution for 30 minutes at room temperature and the retina was dissected from the eyecup. Fixed retinas were sunk in 30% sucrose overnight before freezing. Sucrose sunk tissues were placed in Tissue-Tek optimal cutting temperature (OCT) media (Sakura Finetek, Torrance, CA) and frozen by placing the block above liquid nitrogen to rapidly freeze the sample. Retinas were then sectioned at 10 µm and placed onto charged slides. Whole fixed retinas were washed thoroughly in PBS and then stained. All other tissues were fixed in 4% PFA overnight at 4° C and washed thoroughly with PBS. Tissues for cryo-sectioning were handled in the same manner as the retinas. Brains that were used for vibratome sections were placed in a 6% agarose block and sectioned at 150 µm thickness and stained with 4,6-diamidino-2-phenylindole (DAPI) reagent at a dilution of 1:50,000 of a 1 mg/ml stock.

Immunohistochemistry: *Sections:* Tissues were blocked in a blocking solution (5% normal donkey serum, 0.1% Triton X-100 and PBS) for 30 minutes at room temperature. Blocking solution was used to dilute primary antibodies. Sections were incubated in primary antibodies overnight at 4° C. Sections were then washed in PBS at room temperature 3 times prior to secondary staining. Secondary antibodies were also diluted in blocking solution and incubated overnight at 4° C. Sections were again washed 3 times in PBS at room temperature. DAPI was added to the second wash at a concentration of 1:50,000 from a 1 mg /ml stock. Coverslips were applied using 80% glycerol as a mounting medium. *Whole retinas:* Whole retinas were stained in a similar manner except: blocking solution used was composed of (5% normal donkey serum, 0.4% Triton X-100 and PBS), blocking was performed at 4° C overnight, both primary and secondary incubations lasted 2-4 days at 4° C, and the final wash was performed in 0.4% Triton blocking solution overnight at 4° C.

Antibodies: The following antibodies were used within this study: mouse anti-POU4F1/BRN3A (Millipore, Darmstadt, Germany; MAB1585; 1:100); goat anti-POU4F2/BRN3B (Santa Cruz Biotechnology, Santa Cruz, CA; sc-6026; 1:100); rabbit anti-Melanopsin (generous gift from Ignacio Provencio; 1:10,000); rabbit anti-tyrosine hydroxylase (Millipore; AB152; 1:500); mouse anti-AP2α (Developmental Studies Hybridoma Bank, Trevor J. Williams; 3B5; 1:50); rabbit anti-Calbindin (Swant, Marly, Switzerland; CB-38a; 1:1000); goat anti-Choline Acetyltansferase (Millipore; AB144P; 1:250); rabbit anti-bNOS (Sigma, St. Louis, MO; N7280; 1:5000); mouse anti-PKCα (Santa Cruz Biotechnology, sc-17769; 1:500); rabbit anti-Cone Arrestin (Millipore; AB15282;

1:10,000); mouse anti-Glutamine Synthetase (Millipore; MAB302; 1:1000); mouse anti-calsenilin (Millipore; 05-756; 1:1000); mouse anti-PAX6 (developed by Kawakami, Developmental Studies Hybridoma; 1:500); rabbit anti-Cre (Millipore; 69050-3; 1:500). All secondary antibodies were used at 1:1000 (Jackson ImmunoResearch, West Grove, PA).

Fluorescent microscopy: Sections and whole retinas were imaged using an Olympus or Nikon spinning disk confocal microscope or an Olympus Fluoview confocal microscope. Adobe Photoshop was used to crop and rotate images. If brightness or contrast was altered, it was done uniformly across the entire image.

RESULTS

Pou4f2^{Cre} can be used to deplete RGCs.

The *Pou4f2*^{Cre} transgenic line that was used in this study was previously generated, but never characterized [10]. Since the method used to generate the mice was not known, numerous primers were designed specific to the native *Pou4f2* sequence and Cre recombinase to determine the site of Cre insertion within the *Pou4f2* locus (Figure 5.1 A, B and not shown). Additionally, primers designed specific to neomycin were created to determine if this cassette still remained within the transgene (Figure 5.1 B). Through the use of polymerase chain reaction (PCR) and sequencing of PCR products, we successfully mapped the location of *Pou4f2*^{Cre} (Figure 5.1 C and not shown). The inserted transgene consists of an internal ribosome entry site (IRES) Cre fused to exon 1 of the native *Pou4f2* sequence and an inverted neomycin cassette (Figure 5.1B). Homozygous carriers of the transgene can be differentiated from heterozygotes by the lack of *Pou4f2* gene, assayed by PCR (Figure 5.1 D). Elimination of POU4F2 (BRN3B) immunoreactivity in the retina and a reduction in RGCs, assayed with an antibody to the homologous protein POU4F1 (BRN3A), was observed in mice homozygous for Cre recombinase, consistent with previous investigations of *Pou4f2* function [2, 3] (Figure 5.1 E-G).

Location of *Pou4f2*^{Cre} recombination is dependent upon breeding scheme.

To test the efficiency and location of *Pou4f2*^{Cre} recombination activity, *Pou4f2*^{Cre} mice were crossed to a mouse strain carrying a sensitive and ubiquitously expressed Cre

reporter, Ai9 [11]. The Ai9 reporter (Figure 5.2A) is driven by the CAG promoter, which is followed by a loxP-flanked transcription termination cassette and red fluorescent protein (RFP). Upon Cre-mediated recombination, the transcription termination cassette is removed, allowing for the transcription of RFP. This results in the production of RFP in tissues that have expressed Cre recombinase.

Cre activity was determined by visualization of RFP in cryo-sections and tissue biopsies of mouse tissues (Figure 5.2 C-E). The pattern of recombination was dependent upon which parent carried the Cre and the target of Cre. When the sire carried *Pou4f2*^{Cre} and Ai9, germline recombination occurred (Figure 5.2 Bi and D). Germline recombination of the reporter was observed in offspring regardless of whether they inherited *Pou4f2*^{Cre}, verified by PCR (not shown), suggesting that recombination was targeted in the germline. RFP was observed within testis of sexually mature mice carrying both the *Pou4f2*^{Cre} and the Ai9 reporter (Figure 5.2 E), consistent with these results and previous reports that *Pou4f2* is expressed within germ cells [14, 15]. When the sire carried *Pou4f2*^{Cre} and the dam carried the reporter, recombination was limited to subsets of cells within the retina, brain, intestines, heart and gonads (Figure 5.2 Bii and E). When the dam carried *Pou4f2*^{Cre}*,* recombination was limited to subsets of cells within the retina, brain, intestines, heart and gonads, regardless of which parent carried the reporter allele (Figure 5.2 Biii-iv and E). No visualization of the Ai9 reporter was detected in mice lacking *Pou4f2*^{Cre} (Figure 5.2 C).

Pou4f2^{Cre} mediated recombination within the retina.

To test the specificity of *Pou4f2*^{Cre} expression within the retina, *Pou4f2*$^{Cre/+}$ Ai9 retina sections from crosses generating specific recombination (Figure 5.2 Bii-iv and E) were immunostained with a panel of cell type specific markers (Figure 5.3, Figure 5.4 and Table 5.1). Reporter activity was limited to neurons, but was also detected in neuron populations not know to express *Pou4f2*. Recombination was observed in RGCs (Figure 5.3 A and B), amacrine cells (ACs) (Figure 5.3 C-E and Figure 5.4 A-B), bipolar cells (BCs) (Figure 5.4 C), horizontal cells (HCs) (Figure 5.3 D) and a very small number of photoreceptors (Figure 5.4 D). No Cre activity was detected within microglia, astrocytes or blood vessels (not shown). Müller glia were also not normally targeted by Cre (Figure 5.4 E and E''). However, 1 out of the 34 mice observed in this study contained columns of cells produced RFP, suggesting that a small number of retinal progenitor cells had expressed Cre (not shown).

For the majority of markers used in this study only a portion of the cells produced RFP, with the exception of POU4F2, where all counted cells produced RFP (Table 5.1). *Pou4f2*$^{Cre/+}$ mice were also crossed with mice carrying the Brainbow reporter (Figure 5.4 F). The Brainbow reporter is a transgene driven by the *Thy1* promoter that encodes a series of fluorescent proteins, each flanked by loxP sites [16]. This genetic construct allows for differential expression and visualization of fluorescent proteins. Cre expression within the retina was again limited to neurons within the retina, but only those that express *Thy1*; RGCs, ACs, HCs (Figure 5.4 F).

Pou4f2$^{Cre/+}$ Ai9 retina sections were taken from crosses generating specific recombination in order to map out the developmental time-course at which *Pou4f2*^{Cre} targeted recombination in different cell populations (Figure 5.2 Bii-iv and E). The proportion of cells producing RFP and positive for specific markers were quantified at P0, P10, P20 and P40 (Figure 5.5). The proportion of cells positive for RFP and PAX6, ChAT and calsenilin increased incrementally from P0 to P40, while POU4F2 positive cells were all targeted starting from P0, the earliest time point sampled (Figure 5.5 A-I). Immunohistochemistry was then used to detect the location of Cre protein (Figure 5.5 J-M). Cre protein was observed within the neurites and nuclei of cells in which recombination occurred (Figure 5.5 J), while staining was absent in retina sections taken from mice lacking Cre (Figure 5.5 K). Cre protein was observed within the nuclei and neurites of subsets of ganglion cells and horizontal cells, confirmed by co-staining with POU4F2 and PAX6 (not shown), but was absent from the nuclei of amacrine and bipolar cells at P10 (Figure 5.5 L, L'). Cre protein was observed within the nuclei of cells in the RGL and INL by P40, consistent with reporter activation (Figure 5.5 M and M'). Late activity of *Pou4f2*^{Cre} was also effective in targeting constructs other than the highly sensitive Ai9 and Brainbow reporters. A conditional allele of Down syndrome cell adhesion molecule *(Dscam)* was used to demonstrate this activity, which is evidenced by the accumulation of DSCAM protein with the cells bodies of targeted cells [17]. *Dscam* targeting was observed in ganglion cells and amacrine cells early during development, and later (~P45) in bipolar cells (Figure 5.5 N).

Pou4f2^{Cre} activity within the brain.

Pou4f2$^{Cre/+}$ Ai9 brains from crosses generating specific recombination were imaged to test the specificity of *Pou4f2*^{Cre} expression within the brain (Figure 5.2 Bii-iv and E). RFP

was observed in many regions of the brain (Figure 5.6). The expression of RFP was observed in retinal ganglion cell axons projecting throughout the brain, but was also found within neural cell bodies and their neurites in other regions of the brain, including visual centers, consistent with previous studies [9, 18]. The percentage of cells targeted by *Pou4f2*^{Cre} within three visual centers was determined; the suprachiasmatic nucleus (SCN), lateral geniculate nucleus (LGN) and the superior colliculus (SC) (Figure 5.7). This was accomplished by staining vibratome sections of brain with DAPI and counting the total number of cells positive for RFP. Our results indicate that 18% of cells within the SCN had expressed Cre, 11% for the LGN and 17% for the SC (Figure 5.8 D-G).

DISCUSSION

This study characterized a *Pou4f2*^{Cre} transgenic mouse line, in which Cre recombinase is driven by the *Pou4f2* promoter. Our results show that this transgenic mouse can be used (1) to deplete RGC populations when homozygous for the *Pou4f2*^{Cre}, (2) that the pattern of Cre recombination is dependent upon which parent carries *Pou4f2*^{Cre} and the target of recombination, making it useful to target germline recombination and (3) that Cre specific activity within the retina is limited to the neurons (RGCs, ACs, BCs, HCs, and a small number of photoreceptors) and (4) that the timing of *Pou4f2*^{Cre} recombination is subclass specific. These properties make this line a useful multipurpose genetic reagent for vision researchers.

The *Pou4f2*^{Cre} knock-in transgenic mouse can be used to generate RGC specific depletion, consistent with previous literature demonstrating that deletion of *Pou4f2* results in depletion of about 70% of RGCs [2, 3]. Previous studies have also shown that the remaining RGCs within *Pou4f2* knockout mice maintain normal RGC diversity and a grossly normal morphology [19]. Using the *Pou4f2*^{Cre} transgenic mouse line to drastically reduce RGC populations allows questions to be asked about how retinas develop without normal populations of RGCs and the effects major depletion of RGCs has on the developing retina.

The *Pou4f2*^{Cre} line can also be used to target recombination in the germline, depending on which parent carries the *Pou4f2*^{Cre} and the target for recombination. Germline recombination occurs when the sire carried *Pou4f2*^{Cre} and the target for recombination, yet was always specific when the dam carried *Pou4f2*^{Cre}. This was an interesting observation

consistent with the expression of *Pou4f2* in the male and female germline and suggests that the *Pou4f2*^{Cre} transgenic mouse line could be used to understand the genetic underpinnings of varying germline development between sexes [14, 15]. In crosses we have established using floxed alleles of target genes the recombination rate is complete, resulting in 100% transmission of recombined alleles, which increases the efficiency of producing mice that carry mutations that would otherwise prevent or reduce breeding efficiency.

The activity of *Pou4f2*^{Cre} recombination was observed in multiple populations of cells in the retina. Here we mapped patterns of recombination using two different reporter lines, Ai9 and Brainbow. The *Pou4f2*^{Cre} line targets RGCs during early stages of retinal development and would be useful to study processes such as RGC axon guidance. At later time points, recombination is observed within neurons in the retinal ganglion cell layer and inner nuclear layer and in a small number of photoreceptors. The Brainbow reporter was only observed in RGCs, ACs and HCs, consistent with activity of the *Thy1* promoter. The expression of Cre from the *Pou4f2* locus differs from immunohistological studies in which RGCs are the primary cell type of the retina expressing *Pou4f2*^{Cre} and related proteins [9]. The IRES-sequence added to the construct is highly GC-rich and such sequences are likely to alter local DNA methylation patterns. We speculate that this is why the expression pattern of Cre also differs from a recently reported *Pou4f2* Dre/Cre line [18]. In this line Dre mediated recombination replaces the *Pou4f2* gene with Cre. The Cre driven from the *Pou4f2* locus in this transgenic mouse is observed in the entire animal, which is different compared to the expression pattern of *Pou4f2* as detected by *in situ* [18]. These results suggest that expression driven from the *Pou4f2* locus is highly sensitive to small changes, such as those made in engineering the recombinant lines and could account for the expression of Cre in non-RGC cell populations in the retina reported in this study. Alternatively, this could reflect low expression of *Pou4f2* in these cell types (i.e., ACs).

We also report that the timing of *Pou4f2*^{Cre} mediated recombination within the retina is also highly dependent upon the cell type in which the target of recombination is located. By taking advantage of the timing of this recombination pattern investigators will have a reproducible method to target amacrine and bipolar cells after the completion of developmental processes such as developmental cell death and dendrite outgrowth to complement use of Cre:ER lines. Sparse recombination was also observed in neurons of the enteric nervous system, photoreceptors and some other regions of the brain, allowing for genetic manipulations to be targeted in a small number of cells.

In conclusion, this study characterizes a transgenic *Pou4f2* knock-in Cre recombinase transgenic mouse line. This line can be used to deplete RGC number, to target germline recombination and to target recombination in retinal neurons while sparing Müller glia and most photoreceptors.

ACKNOWLEDGEMENTS

This research was supported by the National Eye Institute Grant EY020857. Imaging support was provided by NIH Grant Nos. P20 RR016454, P30 GM103324-01 and P20 GM103408.

AUTHOR CONTRIBUTIONS

All authors contributed to laboratory work and data collection. Writing was done by ABS and PGF.

REFERENCES

1. Sauer B, Henderson N. Site-specific DNA recombination in mammalian cells by the Cre recombinase of bacteriophage P1. Proceedings of the National Academy of Sciences of the United States of America. 1988;85(14):5166-70.
2. Erkman L, McEvilly RJ, Luo L, Ryan AK, Hooshmand F, O'Connell SM, Keithley EM, Rapaport DH, Ryan AF, Rosenfeld MG. Role of transcription factors Brn-3.1 and Brn-3.2 in auditory and visual system development. Nature. 1996;381(6583):603-6.
3. Gan L, Xiang M, Zhou L, Wagner DS, Klein WH, Nathans J. POU domain factor Brn-3b is required for the development of a large set of retinal ganglion cells. Proceedings of the National Academy of Sciences of the United States of America. 1996;93(9):3920-5.
4. Xiang M. Requirement for Brn-3b in early differentiation of postmitotic retinal ganglion cell precursors. Developmental biology. 1998;197(2):155-69.
5. Liu W, Khare SL, Liang X, Peters MA, Liu X, Cepko CL, Xiang M. All Brn3 genes can promote retinal ganglion cell differentiation in the chick. Development. 2000;127(15):3237-47.

6. Gan L, Wang SW, Huang Z, Klein WH. POU domain factor Brn-3b is essential for retinal ganglion cell differentiation and survival but not for initial cell fate specification. Developmental biology. 1999;210(2):469-80.
7. Wang SW, Gan L, Martin SE, Klein WH. Abnormal polarization and axon outgrowth in retinal ganglion cells lacking the POU-domain transcription factor Brn-3b. Molecular and cellular neurosciences. 2000;16(2):141-56.
8. Erkman L, Yates PA, McLaughlin T, McEvilly RJ, Whisenhunt T, O'Connell SM, Krones AI, Kirby MA, Rapaport DH, Bermingham JR, O'Leary DD, Rosenfeld MG. A POU domain transcription factor-dependent program regulates axon pathfinding in the vertebrate visual system. Neuron. 2000;28(3):779-92.
9. Badea TC, Cahill H, Ecker J, Hattar S, Nathans J. Distinct roles of transcription factors brn3a and brn3b in controlling the development, morphology, and function of retinal ganglion cells. Neuron. 2009;61(6):852-64.
10. Fuerst PG, Bruce F, Rounds RP, Erskine L, Burgess RW. Cell autonomy of DSCAM function in retinal development. Developmental biology. 2012;361(2):326-37.
11. Madisen L, Zwingman TA, Sunkin SM, Oh SW, Zariwala HA, Gu H, Ng LL, Palmiter RD, Hawrylycz MJ, Jones AR, Lein ES, Zeng H. A robust and high-throughput Cre reporting and characterization system for the whole mouse brain. Nature neuroscience. 2010;13(1):133-40.
12. Cai D, Cohen KB, Luo T, Lichtman JW, Sanes JR. Improved tools for the Brainbow toolbox. Nature methods. 2013;10(6):540-7.
13. Truett GE, Heeger P, Mynatt RL, Truett AA, Walker JA, Warman ML. Preparation of PCR-quality mouse genomic DNA with hot sodium hydroxide and tris (HotSHOT). BioTechniques. 2000;29(1):52, 4.
14. Lillycrop KA, Budrahan VS, Lakin ND, Terrenghi G, Wood JN, Polak JM, Latchman DS. A novel POU family transcription factor is closely related to Brn-3 but has a distinct expression pattern in neuronal cells. Nucleic acids research. 1992;20(19):5093-6.
15. Budhram-Mahadeo V, Moore A, Morris PJ, Ward T, Weber B, Sassone-Corsi P, Latchman DS. The closely related POU family transcription factors Brn-3a and Brn-3b are expressed in distinct cell types in the testis. The international journal of biochemistry & cell biology. 2001;33(10):1027-39.
16. Livet J, Weissman TA, Kang H, Draft RW, Lu J, Bennis RA, Sanes JR, Lichtman JW. Transgenic strategies for combinatorial expression of fluorescent proteins in the nervous system. Nature. 2007;450(7166):56-62.

17. de Andrade GB, Long SS, Fleming H, Li W, Fuerst PG. DSCAM localization and function at the mouse cone synapse. The Journal of comparative neurology. 2014;522(11):2609-33.
18. Sajgo S, Ghinia MG, Shi M, Liu P, Dong L, Parmhans N, Popescu O, Badea TC. Dre - Cre sequential recombination provides new tools for retinal ganglion cell labeling and manipulation in mice. PloS one. 2014;9(3):e91435.
19. Lin B, Wang SW, Masland RH. Retinal ganglion cell type, size, and spacing can be specified independent of homotypic dendritic contacts. Neuron. 2004;43(4):475-85.

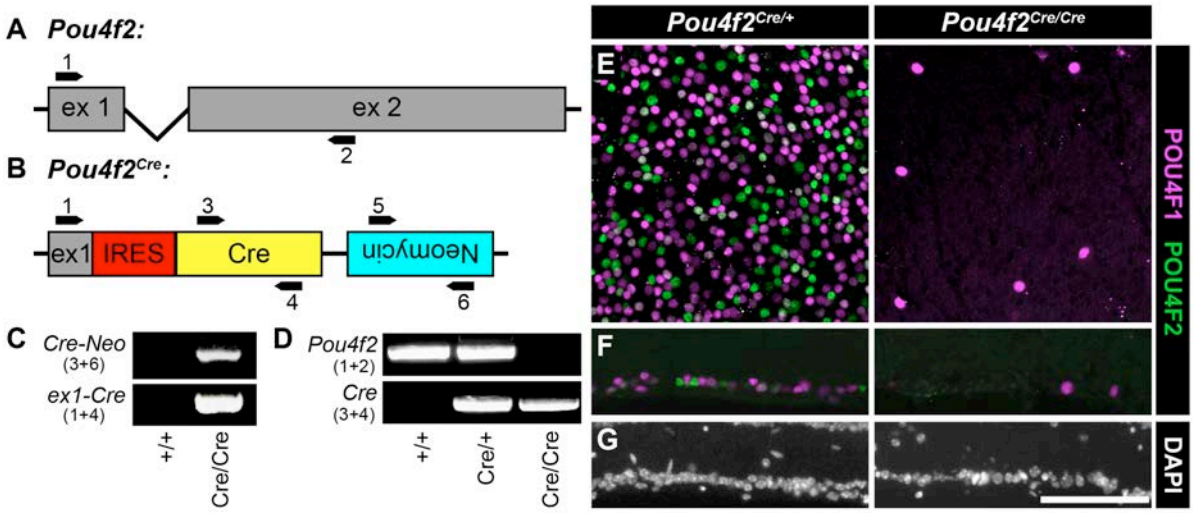

Figure 5.1. *Pou4f2*^{Cre}. A, Diagram of the *Pou4f2* gene showing exons, introns and locations of designed primers. **B,** Diagram showing the *Pou4f2*^{Cre} construct and locations of designed primers. The construct consisting of an internal ribosome entry site (IRES) Cre, fused to exon1, and an inverted neomycin cassette. **C,** Polymerase chain reaction (PCR) product showing DNA sequence unique to *Pou4f2*^{Cre}, compared to wild type. These bands were sequenced to confirm authenticity of the bands. **D**, PCR was used to determine the zygosity of Cre. *Pou4f2*$^{+/+}$ mice are *Pou4f2* positive and Cre negative. *Pou4f2*$^{Cre/+}$ mice are *Pou4f2* and Cre positive. *Pou4f2*$^{Cre/Cre}$ mice are *Pou4f2* negative and Cre positive. **E**, Retina whole mounts immunostained for POU4F1 (BRN3A) and POU4F2 (BRN3B). **F**, Cryo-sections of retina immunostained for POU4F1 and POU4F2. *Pou4f2*$^{Cre/Cre}$ retinas display a large reduction in POU4F1 positive cells and no POU4F2 immunoreactivity. **G**, DAPI staining for panel **F**. No significant difference was found between POU4F1 and POU4F2 positive cells across *Pou4f2*$^{Cre/+}$ and *Pou4f2*$^{+/+}$ retinas (data not shown). Scale bar = 100 µm.

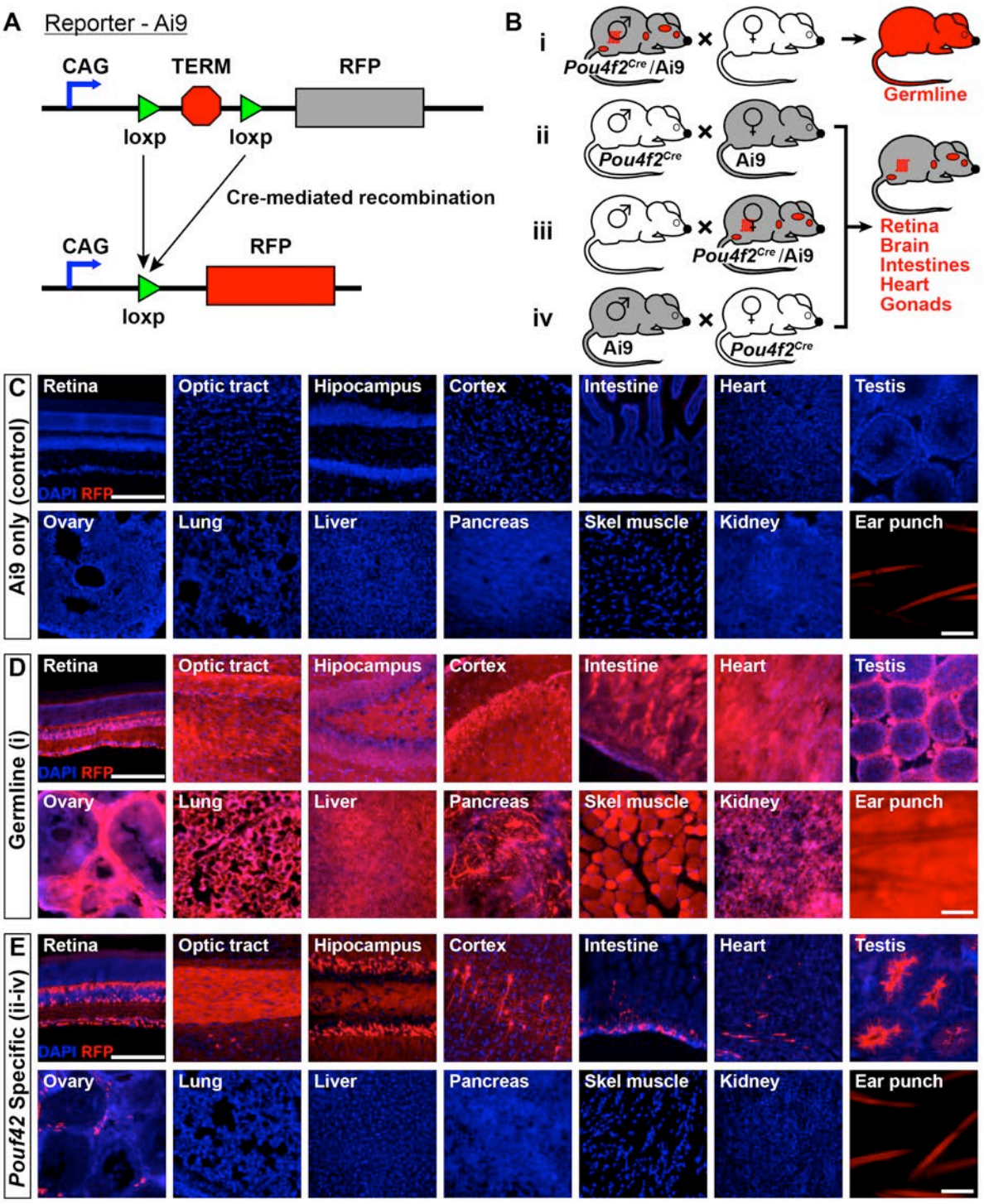

Figure 5.2. *Pou4f2*^{Cre} Recombination Patterns. A, Diagram of the Ai9 Cre reporter construct. This fluorescent reporter is driven by the CAG promoter and is designed to transcribe red fluorescent protein (RFP) after Cre-mediated recombination removes the transcription termination cassette. **B**, Cartoon diagram showing varying Cre-mediated

recombination patterns, which were dependent upon the parent carrying *Pou4f2*^{Cre} and the reporter. **B(i)**, Ubiquitous production of RFP in offspring when *Pou4f2*^{Cre} and Ai9 are carried by the sire. **(ii-iv)** *Pou4f2*^{Cre} specific recombination was observed in offspring when the sire carries *Pou4f2*^{Cre} and the dam carries Ai9 (ii); *Pou4f2*^{Cre} and Ai9 are carried by the dam (iii); or Ai9 is carried by the sire and the dam carries *Pou4f2*^{Cre}(iv). **C**-**E**, Images of cryo-sections and tissue biopsies (ear) that are counterstained with DAPI. **C**, No RFP was detected in mice carrying Ai9 only. **D**, Offspring with germline recombination, RFP was detected throughout all tissues. **E**, Offspring with *Pou4f2*^{Cre} specific recombination. RFP was detected in the retina, brain, intestine, heart and gonads. Scale bars = 100 µm (retina-kidney, scale bar in retina image; ear punch, scale bar in image).

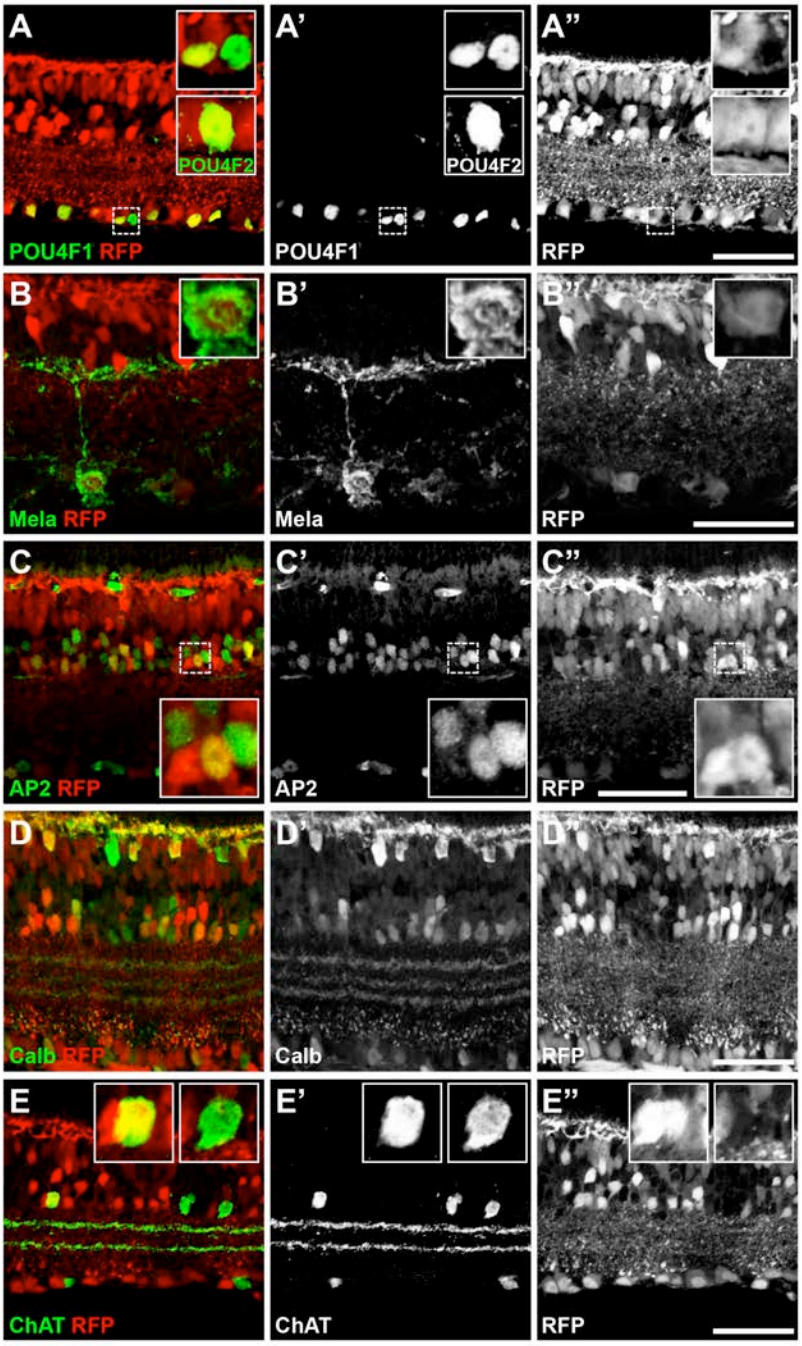

Figure 5.3. *Pou4f2*^{Cre} mediated recombination within the retina. Cre-mediated recombination within the retina was assayed in *Pou4f2*$^{Cre/+}$ Ai9 mice by immunostaining cryo-sections of retina with a panel of markers. Channels are split out for better visualization. Markers are described in further detail in Table 5.1. Abbreviations: mela: melanopsin, Calb: calbindin. Scale bars = 50 μm. Insets = 16 μm boxes.

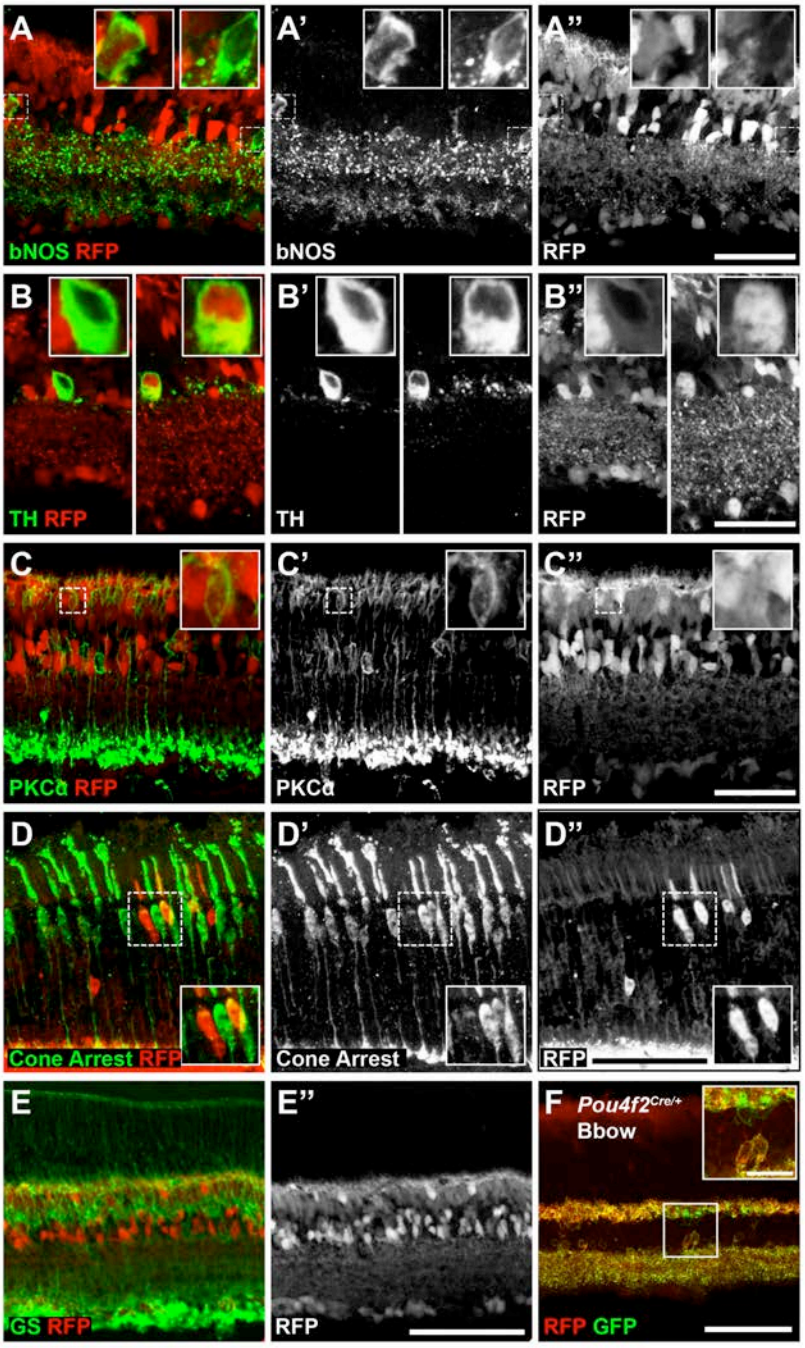

Figure 5.4. *Pou4f2*^{Cre} mediated recombination within the retina continued. Recombination within the retina was assayed in *Pou4f2*$^{Cre/+}$ Ai9 mice by immunostaining cryo-sections of retina with a panel of markers. Channels are split out for better visualization. Markers are described in further detail in Table 5.1. Abbreviations: TH: tyrosine hydroxylase, PKC: protein kinase C, GS: glutamine synthetase. Scale bars = 50 μm. Insets A-C = 16 μm boxes, Insets in D and F = 24 μm boxes.

Table 5.1: Retinal Cell Types Expressing *Pou4f2*^{Cre}		
Marker	**Population**	**Cre+ (%)**
POU4F2 (BRN3B)	RGCs	100
POU4F1 (BRN3A)	RGCs	86
Melanopsin	RGCs	79
AP2α	ACs	44
Calbindin	ACs	60
	HCs	100
ChAT	Cholinergic ACs	97
bNOS	bNOS ACs	38
TH	Dopaminergic ACs	50
PKCα	Rod BCs	0
Cone Arrestin	Cones	2
GS	Müller Glia	0*
IBA-1	Microglia	0
GFAP	Astroctyes	0
GS iso B4	Blood Vessels	0

Table 5.1. Retinal Cell Types Expressing *Pou4f2*^{Cre}. Immunohistochemistry was performed on *Pou4f2*$^{Cre/+}$ Ai9 retinas to determine which cells types within the retina express *Pou4f2*^{Cre}. This table summaries Figure 5.3 and 5.4 and contains markers not shown (IBA-1, GFAP, GS isolection-B4). *1 out of 34 mice contained sparsely labeled Müller glia, where columns of cells expressed tdTomato. Abbreviations: ACs—amacrine cells, BCs—rod bipolar cells, HCs—horizontal cells, RGCs—retinal ganglion cells, TH—tyrosine hydroxylase, PKC—protein kinase C, GS—glutamine synthetase.

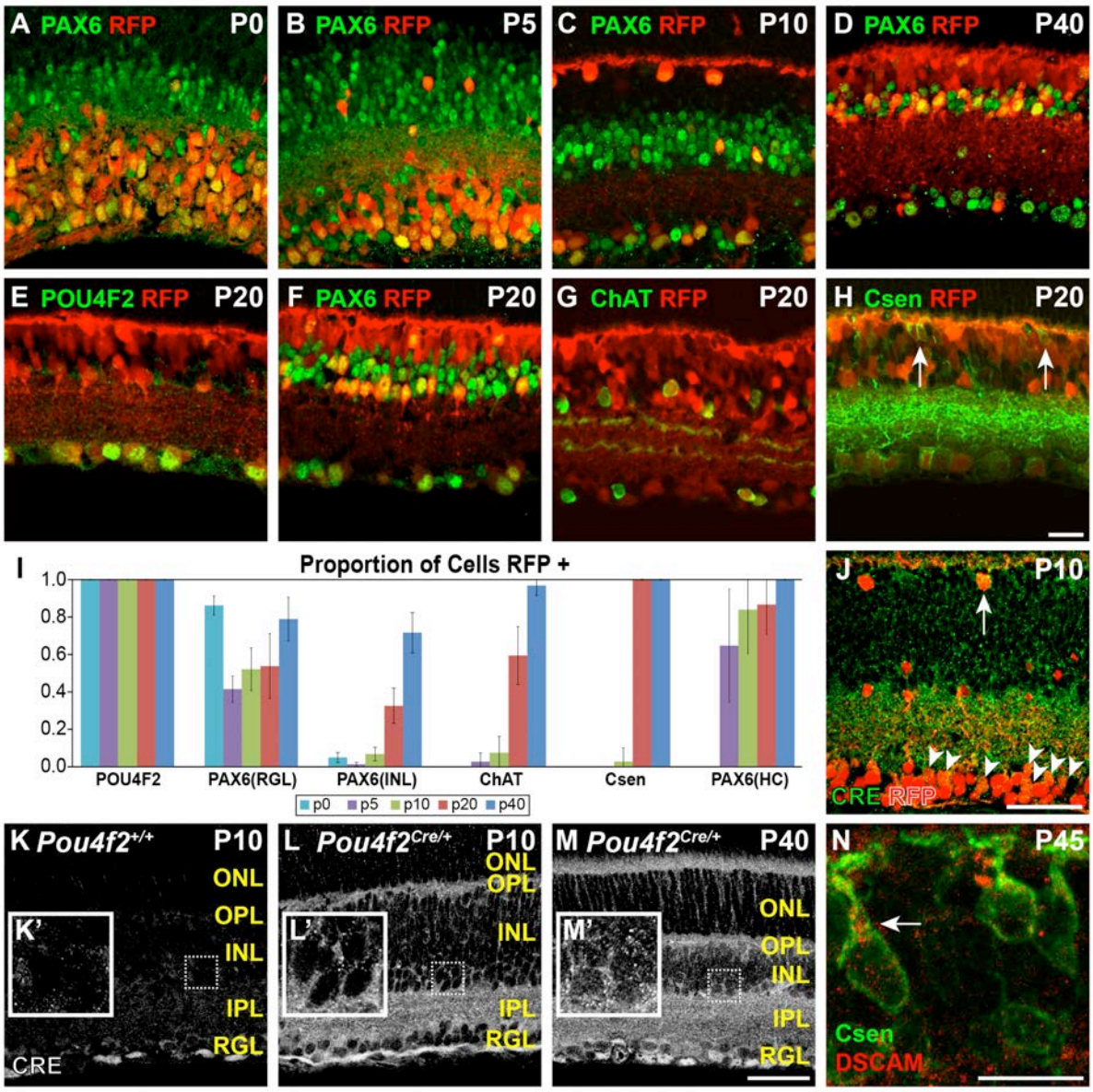

Figure 5.5. Developmental time-course of *Pou4f2*^{Cre} activity within the retina. A developmental time-course of Cre targeting within the retina was performed by immunostaining cryo-sections of retina with neural markers (PAX6, POU4F2, ChAT and Calsenilin). The proportions of reporter positive cells for each of the markers at P0, P5, P10, P20 and P40 were quantified. Progression in the proportion of cells targeted by *Pou4f2*^{Cre} increased in all of the markers over developmental time, except for POU4F2 positive cells, which were 100% targeted starting from P0. **A-D,** developmental time-course of PAX6 except P20. **E-H,** representative images of all the markers at P20. **I,** Graph illustrating the proportion of cells positive for the Ai9 reporter over time. PAX6-positive cells were subdivided into cells found within the RGL, INL and HCs in the outer INL. Calsenilin

(Csen) was used to label Type 4 bipolar cells and bipolar cells were the only quantified cell type reported for this stain. **J**-**M**, Cre protein staining. **J**, Cre was detected within cell bodies and neurites of cells in the RGL (arrowheads) and horizontal cells (arrow). **K,** Cre negative control. Cre protein was not observed. **L,** Cre was detected within the nuclei and neurites of cells within the RGL but was absent from most nuclei within the INL at postnatal day 10 (P10) (L'). **M,** Cre was detected within the nuclei of cells in the RGL and INL, consistent with reporter activation. **M',** Inset showing Cre within cells of the INL. **N,** *Pou4f2*^{Cre} effectively targets a conditional allele of *Dscam* at P45 in bipolar cells, evidenced by accumulation of DSCAM protein in the cell body. Abbreviations: Csen: calsenilin. Scale bar in H = 20 μm. Scale Bars in J-L = 50 μm. Scale bar in M = 20 μm. Insets in J-K = 25 μm box.

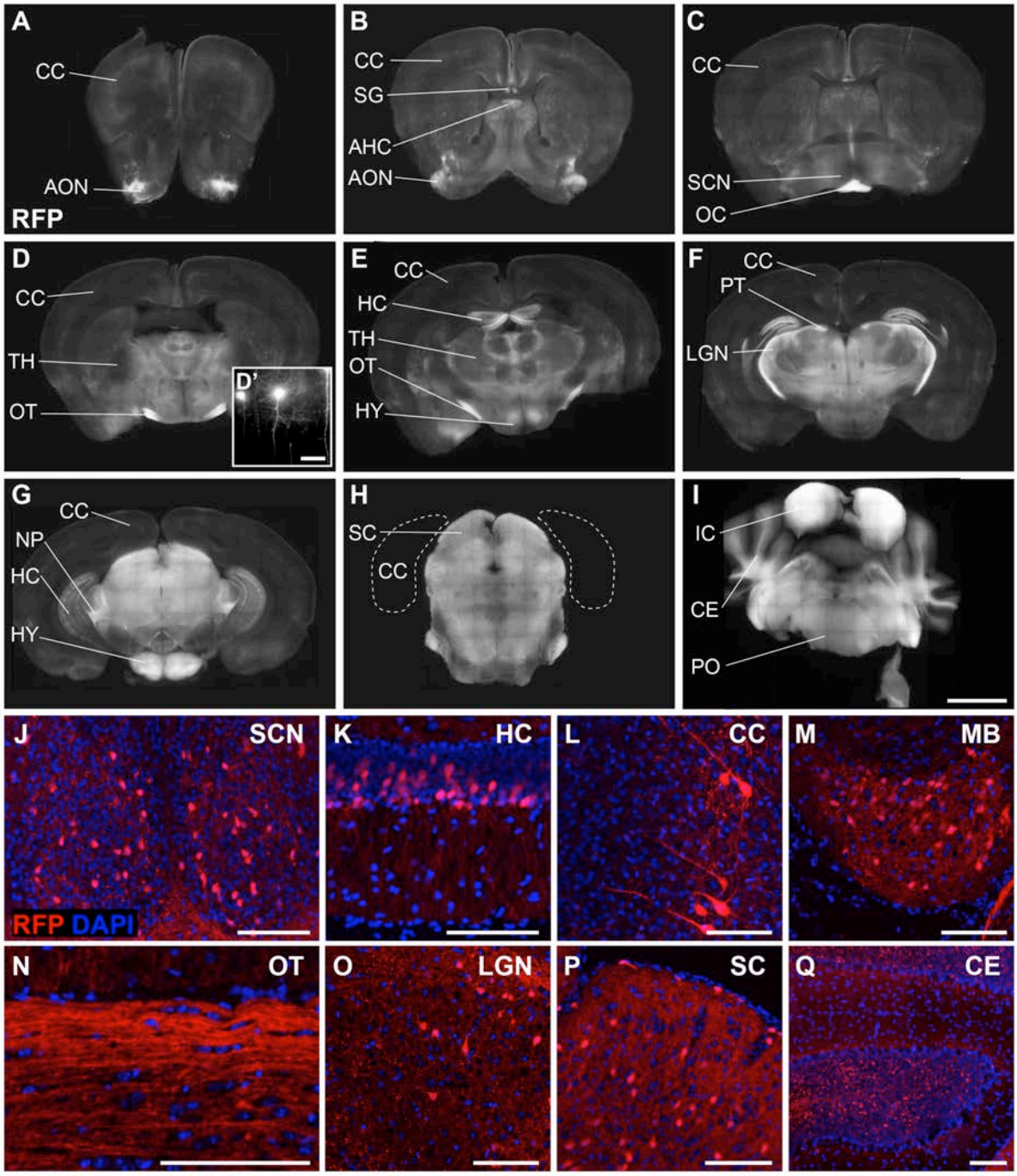

Figure 5.6. *Pou4f2*^{Cre} mediated recombination within the brain. Cre mediated recombination within the brain was assayed in vibratome and cryo-sections of *Pou4f2*$^{Cre/+}$ Ai9 mice. **A-I,** in vibratome sections, reporter activity was detected throughout many regions of the brain. **D',** high magnification image showing pyramidal cells targeted by Cre. **J-Q,** in cryosections, reporter activity was found within retina ganglion cell axons projecting

throughout the brain, but was also found within neural cell bodies and neurites within the brain, within many different regions. Abbreviations: AHC—Anterior Hippocampus, AON—Anterior Olfactory Nucleus, CC—Cerebral Cortex, CE—Cerebellum, HC—Hippocampus, HY—Hypothalamus, IC—Inferior Colliculus, LGN—Lateral Geniculate Nucleus, MB—Mammillary Body, NP—Nucleus Peduncularis, OC—Optic Chiasm, OT—Optic Tract, PO—Pons, PT—Pretectum, SC—Superior Colliculus, SCN— Suprachiasmatic Nucleus, SG—Supracallosal Gyrus, TH—Thalamus. Scale Bar in D' = 50 μm. Scale Bar in I = 2 mm. Scale Bars in J-Q = 100 μm.

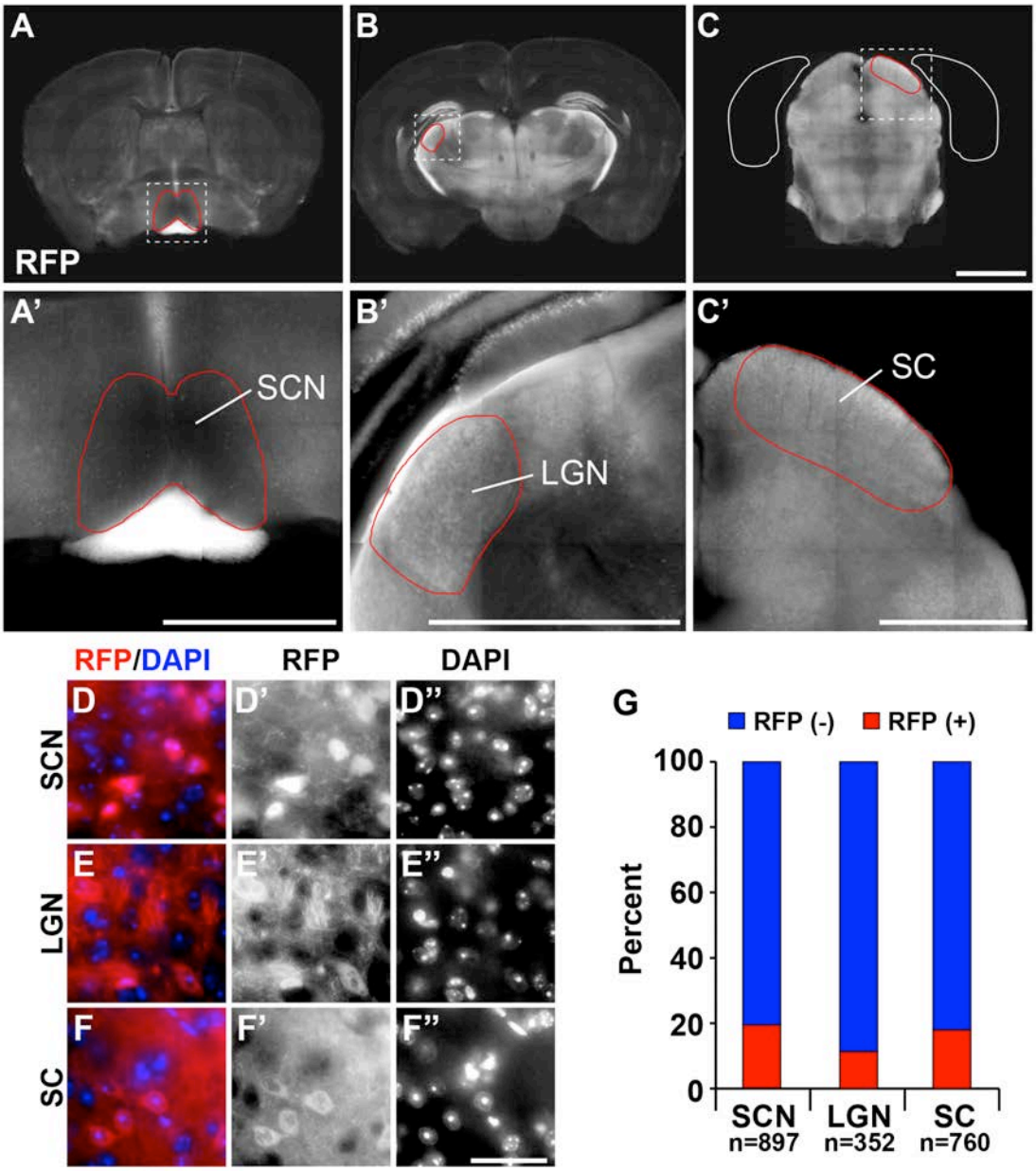

Figure 5.7. *Pou4f2*^{Cre} mediated recombination within visual centers of the brain. The percent of neurons in which recombination was targeted by Cre was quantified within three visual centers of the brain (SCN, LGN and SC) in vibratome sections of *Pou4f2*$^{Cre/+}$ Ai9 brains stained with DAPI. **A-C,** images showing location of visual centers. **D-F,** high magnification images used to quantify number of cells positive for Cre-mediated recombination. **G,** Graph illustrating the percentage of cells targeted by Cre (n=1 animal). Abbreviations: SCN— Suprachiasmatic, LGN— lateral geniculate nucleus, SC— superior colliculus. Scale Bar in C = 2 mm. Scale Bars in A'-C' = 1mm. Scale Bar in F'' = 40 µm.

Chapter 6: Concluding remarks

Throughout my graduate studies I have gained an appreciation for the complexity and interconnectivity within biological systems and the challenges scientists face when attempting to uncover how these systems operate. I have gained a passion for exploring mechanisms responsible for the development of the retina and how an understanding of these mechanisms can be applied towards human disease. I have learned the importance of thoughtfully designed and executed experiments towards the improvement of scientific rigor and impact of the questions to which I seek answers. I have also begun to see the significant knowledge gap about interactions between all cell types within the retina during disease processes that are responsible for driving pathology.

There is a growing need for scientists and clinicians to understand complex cellular interactions between all the cells within retina in order to facilitate the creation of therapeutics that cure retinal degenerative blinding diseases. Remodeling of the retina during these degenerative diseases is well documented and involves the rearrangement of retinal neurons, glia, and the vasculature[1-8]. However, there is little known about the cause and effect relationships that drive rearrangement processes, that is, do vessel changes affect neurons and glia, do neuron changes affect glia and vessels, do glia changes affect vessels and neurons, or is the breakdown of these cellular interactions responsible for the subsequent rearrangement and pathology? There is also little known about how these cellular interactions change as the disease progresses or how these destructive interactions differ from interactions required to maintain retina function and homeostasis in healthy retinas.

There is also a growing need to understand complex signaling events cells employ in response to insults of the retina inflicted by disease or trauma. One of the most prevalent examples relevant to the retina is vascular endothelial growth factor (VEGF) signaling. In response to insufficient oxygen supply, or hypoxia, cells upregulate the expression and release of VEGF through the transcriptional regulation of hypoxic inducible factors[9]. VEGF is a powerful mitogen that will stimulate the growth of vessels into the hypoxic areas[10], but is also an important neuroprotective factor that promotes the survival of neurons[11]. Over-active VEGF signaling is associated with pathologic neovascularization that is experienced during many retinal degenerative blinding disorders. Anti-VEGF agents are used to inhibit VEGF signaling and are effective in reducing pathologic vascular growth, but are also harmful to neurons[12]. A greater understanding of the downstream signaling events specific

to neurons and cells of the vasculature is needed if we want to develop therapeutics that specifically target pathological features of diseases without interfering with protective events.

As I continue my studies of the retina, I will use the experiences and expertise gained here to bridge the fields of neuroscience and angiogenesis to explore complex cellular events driving human pathologies. I will build a research program centered on exploring complex cellular and signaling events occurring during retinal disease. Through my research, I hope to identify mechanisms relevant to the creation of targeted therapeutics that are safer and more effective for retinal diseases.

REFERENCES

1. Hageman GS, Gehrs K, Johnson LV, Anderson D. Age-Related Macular Degeneration (AMD). In: Kolb H, Fernandez E, Nelson R (eds), *Webvision: The Organization of the Retina and Visual System.* Salt Lake City (UT); 1995.
2. Jones BW, Kondo M, Terasaki H, Lin Y, McCall M, Marc RE. Retinal remodeling. *Japanese journal of ophthalmology* 2012;56:289-306.
3. Mehta S. Age-Related Macular Degeneration. *Primary care* 2015;42:377-391.
4. Hartnett ME. Advances in understanding and management of retinopathy of prematurity. *Survey of ophthalmology* 2016.
5. Jones BW, Pfeiffer RL, Ferrell WD, Watt CB, Marmor M, Marc RE. Retinal remodeling in human retinitis pigmentosa. *Experimental eye research* 2016;150:149-165.
6. den Hollander AI, Heckenlively JR, van den Born LI, et al. Leber congenital amaurosis and retinitis pigmentosa with Coats-like exudative vasculopathy are associated with mutations in the crumbs homologue 1 (CRB1) gene. *American journal of human genetics* 2001;69:198-203.
7. Mehalow AK, Kameya S, Smith RS, et al. CRB1 is essential for external limiting membrane integrity and photoreceptor morphogenesis in the mammalian retina. *Human molecular genetics* 2003;12:2179-2189.
8. Lutty GA. Effects of diabetes on the eye. *Investigative ophthalmology & visual science* 2013;54:ORSF81-87.
9. Peet DJ, Kittipassorn T, Wood JP, Chidlow G, Casson RJ. HIF signalling: The eyes have it. *Experimental cell research* 2017.

10. Carmeliet P, Ferreira V, Breier G, et al. Abnormal blood vessel development and lethality in embryos lacking a single VEGF allele. *Nature* 1996;380:435-439.
11. Foxton RH, Finkelstein A, Vijay S, et al. VEGF-A is necessary and sufficient for retinal neuroprotection in models of experimental glaucoma. *The American journal of pathology* 2013;182:1379-1390.
12. Kim LA, D'Amore PA. A brief history of anti-VEGF for the treatment of ocular angiogenesis. *The American journal of pathology* 2012;181:376-379.

Appendix A: Copyright from IOVS

Dear Aaron Simmons,

Permission is hereby granted to reprint the following article in your dissertation for the University of Idaho:

Simmons AB, Merrill MM, Reed JC, Deans MR, Edwards MM, Fuerst PG. Defective angiogenesis and intraretinal bleeding in mouse models with disrupted inner retinal lamination. *Invest Ophthalmol Vis Sci*. 2016;57:1563-1577.

A reprint of this material must include a full article citation.

Best regards,

Debbie Chin
ARVO Journals

Association for Research in Vision and Ophthalmology
1801 Rockville Pike, Suite 400
Rockville, MD 20852 USA
Direct: +1.240.221.2926 | Main: +1.240.221.2900 | Fax: +1.240.221.0370
[www.arvo.org]**www.arvo.org**

Appendix B: Copyright from Molecular Vision

Molecular Vision's policy on republication:

"Articles authored by a student may be reproduced for inclusion in the student's thesis or dissertation, whether in an online repository at the student's institution or through a commercial service used by the student's institution. Such republications must include a citation to the original work in Molecular Vision and must not be changed from the original. They do not require further permissions from Molecular Vision for republication in a thesis or dissertation submitted in partial fulfillment of requirements for an advanced scholarly degree. CC BY-NC-ND 3.0 (see http://creativecommons.org/licenses/by-nc-nd/3.0/ for license terms) applies to derivative works other than the thesis or dissertation."

Additional policy information can be obtained at the journal website:
http://www.molvis.org/molvis/index.html